ABSTRACT

Title of Dissertation: SATELLITE RETRIEVAL OF UPDRAFTS AND CLOUD CONDENSATION NUCLEI CONCENTRATIONS AT CLOUD BASES

Youtong Zheng, Doctor of Philosophy, 2018

Dissertation directed by: Prof. Zhanqing Li
Department of Atmospheric and Oceanic Science/Earth System Science Interdisciplinary Center

Prof. Daniel Rosenfeld
Institute of Earth Science, Hebrew University of Jerusalem, Israel

Aerosol-cloud-climate interactions are the largest uncertainty in climate forcing. Narrowing down the uncertainties of the aerosol impact on Earth's climate ultimately requires concurrent global measurements of aerosol, cloud, and key dynamic quantities. The core variables dictating cloud formation and development as well as aerosol-cloud interactions (ACI) are cloud condensation nuclei (CCN) concentrations and updrafts at cloud base (W_b). Both variables haven long been regarded as non-

retrievable from conventional satellite remote sensing, a major cause of large uncertainty regarding ACI-induced climate radiative forcing. This study attempts to confront these challenges by exploiting any feasibility of satellite-based retrieval of W_b and CCN concentrations based on the most recent generation of operational weather satellite sensors.

Unlike conventional satellite remote sensing that retrieves geophysical quantities from radiance measurements, we estimate variables based on physical understanding of their interactions with conventional meteorological parameters obtained by satellite retrievals together with reanalysis data. Specifically, our methodology uses clouds as a natural analog for CCN chambers. Supersaturation (S) at cloud bases is determined by W_b and satellite-retrieved activated cloud droplet concentrations, which constitute the CCN spectrum, or CCN(S). The W_b is inferred by estimating components of energy that propels the convection. Validations of the retrieved W_b against ground-based updrafts measurements by Dopper lidar/Radar at Oklahoma, at Manaus, at Graciosa Island, and onboard a ship in the northeast Pacific show good agreements with mean absolute percentage errors (MAPE) of 21% and 22% for convective clouds and stratocumulus clouds, respectively. The retrieved W_b were applied for estimating CCN(S) with a MAPE of 30%.

In addition to advancement in satellite retrievals, we find the first robust observational evidence supporting the essential role of cloud-base height in regulating updrafts, an argument that has been used extensively to explain the contrast in lightning activities between land and sea. Additionally, we put forth a new theory interpreting the mechanism of surface coupling of marine stratocumulus clouds. This

theory underscores the important role of cloud-top radiative cooling in driving surface moistures not only in well-mixed marine boundary layers but also in poorly mixed ones where the coupling is achieved via the mechanism of cumulus feeding stratocumulus. This new theory is examined and confirmed by ship-based and satellite measurements.

SATELLITE RETRIEVAL OF UPDRAFTS AND CLOUD CONDENSATION NUCLEI CONCENTRATIONS AT CLOUD BASES

By

Youtong Zheng

Dissertation submitted to the Faculty of the Graduate School of the
University of Maryland, College Park, in partial fulfillment
of the requirements for the degree of
Doctor of Philosophy
2018

Advisory Committee:
Professor Zhanqing Li, Chair
Professor Russell R. Dickerson
Professor Xin-Zhong Liang
Doctor William K.M. Lau
Professor Michael N. Evans (Dean's representative)

Dedication

To my loving mom

Statement of Originality

Chapters 3, 4, 5, and 6 are largely based upon the following five papers I lead:

- Chapter 3:

  Zheng, Y., D. Rosenfeld, and Z. Li, 2015: Satellite inference of thermals and cloud-base updraft speeds based on retrieved surface and cloud-base temperatures. *Journal of the Atmospheric Sciences*, **72,** 2411-2428.

  Zheng, Y., and D. Rosenfeld, 2015: Linear relation between convective cloud base height and updrafts and application to satellite retrievals. *Geophysical Research Letters*, **42,** 6485-6491.

- Chapter 4:

  Zheng, Y., D. Rosenfeld, and Z. Li, 2016: Quantifying cloud base updraft speeds of marine stratocumulus from cloud top radiative cooling. *Geophysical Research Letters*, **43**.

- Chapter 5:

  Zheng, Y., D. Rosenfeld, and Z. Li, 2017: New insights to the mechanism of surface coupling of elevated marine stratocumulus clouds. *submitted to Proceedings of the National Academy of Sciences*.

- Chapter 6:

  Zheng, Y., D. Rosenfeld, and Z. Li, 2017:Satellite retrieval of cloud-base updrafts for marine stratocumulus clouds. *to be submitted to Geophysical Research Letters*.

Chapter 7 is based on a paper (Rosenfeld et al. 2016) in which I am the second author. My contributions are performing satellite retrievals of CCN concentrations

and W_b, analyzing ground-based measurements, and validating the satellite retrievals for cases from two out of three regions in total. The figure 7.6 and 7.7 used in this dissertation were generated by Mira Pohlker and Yannian Zhu, respectively.

Acknowledgements

First of all I would thank my two advisors, Professors Zhanqing Li and Daniel Rosenfeld, for their guidance and encouragement. Professor Li gave me a great deal of freedom to pursue what I am interested in, and offered me a lot of opportunities to attend conferences and visit world-renowned institutes. He trains my writing skills by extensively engaging me in proposal writings, which is very beneficial.

I especially express my deep appreciation to Professor Daniel Rosenfeld. When I first arrived at the Hebrew University of Jerusalem in 2013 to start a one-year research journey with him, I basically had ZERO research experience. He taught me every aspect of doing research: technique, science, and spirit. He is always willing to spend time on advising and motivating me. His enthusiasm for science enlightens me tremendously.

I thank Assaf Zipori, Baruch Fischman, David Giguzin and Tom Goren. The one-year life in Jerusalem is one of the most memorable times in my life. I also thank Maureen Cribb and other group members at the University of Maryland for their help.

I would like to thank my advisory committee members, Drs. Russell Dickerson, William Lau, Xin-Zhong Liang, and Michael Evans, for their services. Appreciation is given to Xing Yu, Bjorn Stevens and Ulrich Pöschl for hosting my visits at Meteorological Institute of Shaanxi Province, Max Planck Institutes (MPI) for Meteorology, and MPI for Chemistry, respectively.

Table of Contents

List of Tables

List of Figures

Chapter 1 Introduction

1.1 Background

Aerosol-cloud interactions (ACI) dominate the uncertainty about the degree of influence that human activities have on the Earth's climate, as stated by nearly all editions of the Inter-Governmental Panel on Climate Change (IPCC) report (Houghton et al. 2001; Solomon 2007; Stocker 2014). Despite an increasing number of studies, either observational or modeling ones, on aerosol−climate interactions over the past 20 years, the uncertainty level associated with the estimated radiative forcing attributed to ACI has not been markedly reduced over the past four IPCC cycles, although our understanding of physical mechanisms has improved dramatically.

Reducing the uncertainty requires global characterization of atmospheric aerosols, clouds and dynamics. There are two basic properties of aerosol particles governing the ACI: (1) the extent to which they scatter and absorb light, and (2) their potential to nucleate cloud droplets under specific conditions of supersaturation that are further dictated by vertical velocity. The global characterization of the first property has improved dramatically in the past 20 years with the advent of pioneering satellite sensors such as Advanced Very High Resolution Radiometer, the Total Ozone Mapping Spectrometer, the Multi-angle Imaging SpectroRadiometer, and the MODerate resolution Imaging Spectroradiometer (Torres et al. 1998; Kaufman et al. 2002; Mishchenko et al. 2003; Kahn et al. 2005; Remer et al. 2008), as well as ground-based aerosol observation networks such as the Aerosol Robotic Network

(Holben et al. 1998). On the contrary, the second property, or cloud condensation nuclei (CCN), has been poorly characterized from space despite its significant role in modulating the hydrological cycle by modifying clouds and precipitation.

The ability of aerosols to act as CCN is primarily determined by a combination of particle size and hygroscopicity (Petters and Kreidenweis 2007). Detailed information about the aerosol size distribution and composition, and their variations with altitude are required. Acquiring any of these quantities is extremely challenging, especially by means of remote sensing from space. Due to the lack of reliable satellite-based CCN measurements, aerosol radiative properties, e.g., aerosol optical depth (AOD) or aerosol index (AI), retrieved from satellite are frequently used as a proxy for CCN (Andreae 2009). However, AOD/AI as a proxy for CCN is a rather crude tool that is fraught with problems for many reasons (Liu and Li 2014) including: (1) aerosol swelling with high relative humidity (Jeong and Li 2010); (2) the uncertainties in solubility and size distribution (Jeong and Li 2005); (3) the lack of a discernible optical signal from small CCN; (4) cloud contamination (Várnai and Marshak 2015); (5) column AOD not representing aerosol concentrations near cloud base; (6) cloud obscuration of aerosols in the boundary layer; and (7) cloud detrainment of aerosols aloft yielding an increase in AOD for deeper and more extensive clouds without a corresponding increase in cloud-base aerosol concentrations. Due to these limitations, using AOD as a proxy for CCN has been critically examined and many problems have been identified (Rosenfeld et al. 2014c; Seinfeld et al. 2016; Stier 2016). Simulations from self-consistent global models of

AOD and CCN reveal that the AOD variability explains less than 25% of the CCN variance over 71% of the area of the globe (Stier 2016).

Besides the above-listed issues concerning AOD, the inherent difficulty in extracting accurate AOD signals in pristine boundary layers due to extremely faint information content makes AOD particularly unsuitable for quantifying aerosol radiative forcing. The disproportionate sensitivity of aerosol forcing to the background state of the pristine atmosphere (Figure 1.1) suggests that the accuracy at which aerosols are measured is most critical in a pristine boundary layer where a very small change in aerosol concentration can cause substantial climate forcing. The retrieval of AOD, however, is uncertain when the boundary layer is clean. This means that even if AOD is a good proxy for CCN under some ideal conditions, the lack of accurate AOD signals in a pristine boundary layer considerably undermines the usefulness of AOD in the quantitative understanding of the response of the climate system to aerosols. To overcome this conundrum, a paradigm change in our approach to estimating CCN is needed. Instead of addressing the limited information content in the optical signal of aerosols, we extract CCN by using clouds as an analog for CCN counter chambers. The detailed theoretical concept for this new approach is described in the next section.

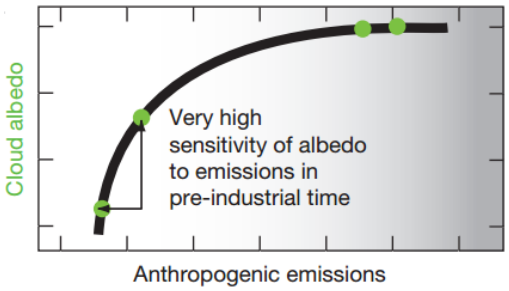

Figure 1.1: A diagram illustrating the nonlinear response of cloud albedo to anthropogenic aerosol emissions, adapted from Carslaw et al. (2013).

1.2 A new retrieval concept and the last missing piece

An innovative approach to satellite measurement of CCN has been proposed by Rosenfeld et al. (2012b) who use clouds as an analog for CCN counter chambers. Traditionally, CCN are measured in a CCN chamber where the water vapor supersaturation (S) is controlled so that the number of activated CCN is counted as a function of S (Figure 1.2a). This is referred to as the CCN spectrum, or CCN(S). The key concept of this satellite-based method is to use convective clouds as a natural analog for the CCN chamber. Natural clouds form in ascending air currents, whereas cloud droplets nucleate on aerosols that serve as CCN. Therefore, the counterparts of S and activated CCN in "cloud" CCN chambers are the maximum supersaturation at cloud base (S_{max}) and the adiabatic cloud droplet number concentration (N_a), respectively. Unlike traditional CCN chambers where S can be manually adjusted, the S_{max} at the cloud bases are controlled by cloud-base updrafts (W_b) and N_a, as shown by the following analytical equation derived based on theoretical considerations (Pinsky et al. 2012):

$$S_{max} = C(T_b, P_b) W_b^{3/4} N_a^{-1/2}, \quad (1.1)$$

where C is a coefficient that depends weakly on cloud-base temperature (T_b) and pressure (P_b). The W_b and N_a control the S_{max} in opposite ways. Strong vertical velocity, via adiabatic cooling effect, facilitates the increase rate of supersaturation in ascending air parcels. This impact could be compensated by adding more CCN into the cloud air parcels, which nucleates a greater number of cloud droplets. More numerous cloud droplets are more effective in consuming the water vapor of the ambient air to buffer the increase in supersaturation. The power of W_b (3/4) is larger than that of N_a (-1/2) in absolute sense, indicating a greater sensitivity of S_{max} to W_b than to N_a. This is because the impact of N_a on supersaturation is coupled with the effect of cloud droplet size (r) to which the supersaturation is more sensitive. The growth of newly nucleated cloud droplets consumes the water vapor of ambient air at a rate of dq_w/dt, where q_w is the liquid water mixing ratio. The q_w is proportional to N_a and to the cubic of r. The larger sensitivity of q_w to r than to N_a diminishes the weight of N_a in controlling the supersaturation.

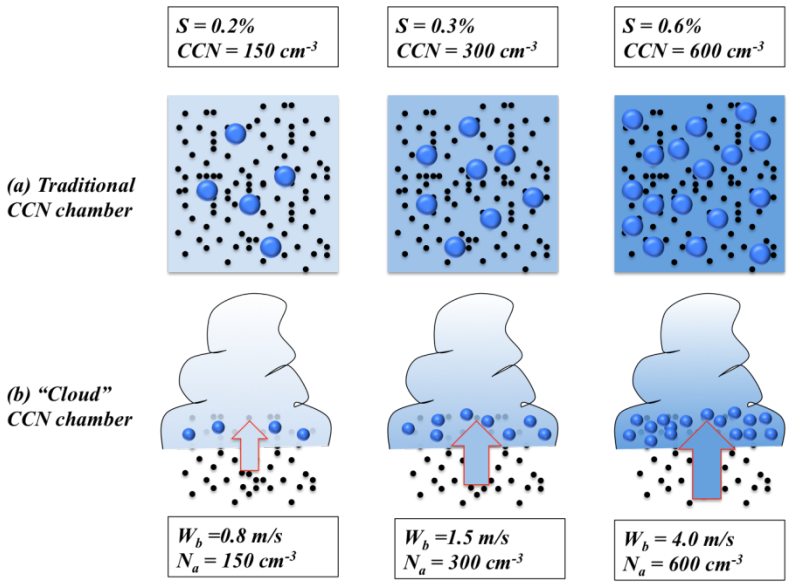

Figure 1.2: A schematic diagram illustrating the concept of a "cloud" CCN chamber (b) in comparison with the traditional CCN chamber (a). The blue-filled circles and black dots represent cloud and aerosol particles, respectively. The background aerosol concentrations and properties are fixed. The color intensity of the blue background indicates the values of supersaturation. The bluer the background, the larger the supersaturation.

The Eq. (1.1) shows that if the W_b and N_a are known, the S_{max} is readily obtained. A combination of S_{max} and N_a constitutes the CCN spectrum, or CCN(S). This retrieval concept is first realized by Rosenfeld et al. (2014a)[1] who use a combination of satellite-measured N_a and Doppler-radar measured W_b to estimate the CCN(S). Validation against ground-based CCN instruments shows an encouragingly good agreement (Figure 1.3). Since the N_a is retrievable from satellite data (the

[1]As a co-author, I contribute to this study by analyzing satellite and ground-based data.

technique detail will be introduced in Chapter 7), the last missing piece of *satellite-only* retrieval of CCN(S) is the satellite retrieval of W_b.

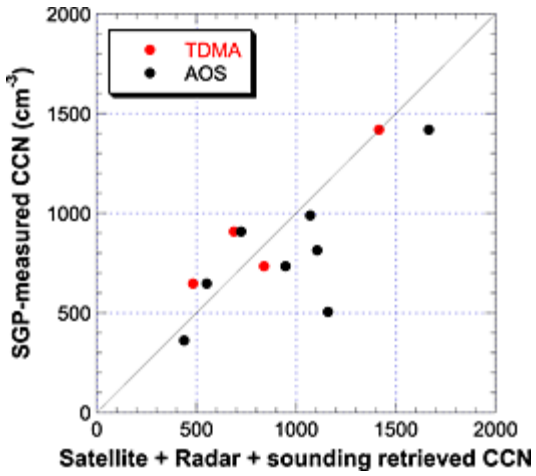

Figure 1.3: Validation of estimated CCN concentrations against ground-based measurements made at the ARM SGP site. The AOS and TDMA stands for the Aerosol Optical System and Tandem Differential Mobility Analyzer, respectively.

The updraft velocity has been the most difficult meteorological quantity to measure by any means. Tracking the vertical movement of cloud tops by monitoring the time evolution of satellite-derived cloud top temperatures allows for the estimation of vertical wind (Luo et al. 2014). Monitoring the flow divergence at cloud top can also help us to infer the vertical motion in clouds based on the continuity equation (Apke et al. 2016). The vertical winds estimated by these techniques represent values at the cloud tops, while it is at the cloud base where the cloud is formed. This is why W_b rather than the cloud-top updraft speed (W_t) is needed. It is

well known that vertical velocity varies considerably in response to the ever-changing buoyancy throughout the cloud column. As such, we cannot extrapolate W_b from W_t.

The limitations of these existing methods motivate me to pursue a paradigm change in retrieval concept, which will be illustrated in Chapter 2.

1.3 The scope of the current study

This dissertation is concerned with developing satellite-based approaches for estimating W_b and CCN(S), and validating the retrievals against "ground truth" measurements. Two different cloud regimes are targeted: convective clouds and stratocumulus (Sc) clouds. These two cloud regimes represent the most dominant low clouds, to which the climate system is particularly sensitive. Their low altitudes make them significantly efficient in reflecting incoming solar radiation, which considerably outweighs their effect on outgoing longwave radiation, thus exerting a strong negative net radiative effect on the Earth's radiation budget (Stephens and Greenwald 1991; Hartmann et al. 1992). This makes them more climatologically important than other cloud types such as cirrus and cumulonimbus clouds. In addition, due to their convective nature, they are typically coupled with local aerosol loadings from the surface, and are particularly susceptible to aerosol indirect effects relative to non-convective clouds such as stratiform clouds associated with large-scale frontal systems (Tao et al. 2012).

The next chapter introduces the methodology. The Chapter 3 is focused on the satellite retrievals of W_b for convective clouds. There are three chapters devoted for marine Sc clouds: Chapter 4 introduces a method for quantifying the W_b from cloud-top radiative cooling rate, which serves as the physical basis for the W_b retrieval;

Chapter 5 describes a new method that infers the coupling state of stratocumulus clouds from space, upon which the W_b retrieval is dependent; Chapter 6 applies the findings of the previous two chapters to satellite retrieval of W_b. The retrieved W_b were applied to estimating the CCN(S) based on Equation (1.1), which is covered in Chapter 7. Chapter 8 presents a summary of the project, discusses limitations, and suggests approaches for future work.

Chapter 2 Methodology

Conventional satellite remote sensing techniques estimate geophysical quantities from satellite radiance measurements, as illustrated in Figure 2.1. For passive methods, radiances observed by satellite sensors represent path-integrated quantities of the atmosphere and surface below. Unlike clear-atmosphere sounding, passive satellite sensors provide little information about vertical structure of clouds. The vast majority of conventionally retrieved cloud quantities represent column-integrated or cloud-top properties. It has been notoriously difficult to retrieve cloud-base quantities even for conventional remote-sensing variables such as temperature, letting alone non-conventional quantities such as updrafts. As such, an indirect approach that infers the W_b based on fundamental understanding of the physical mechanism driving the W_b is exploited in this study. As illustrated in Figure 2.1, by establishing a "simple physics model", we can link conventionally retrieved quantities with the W_b so that the W_b may be inferred.

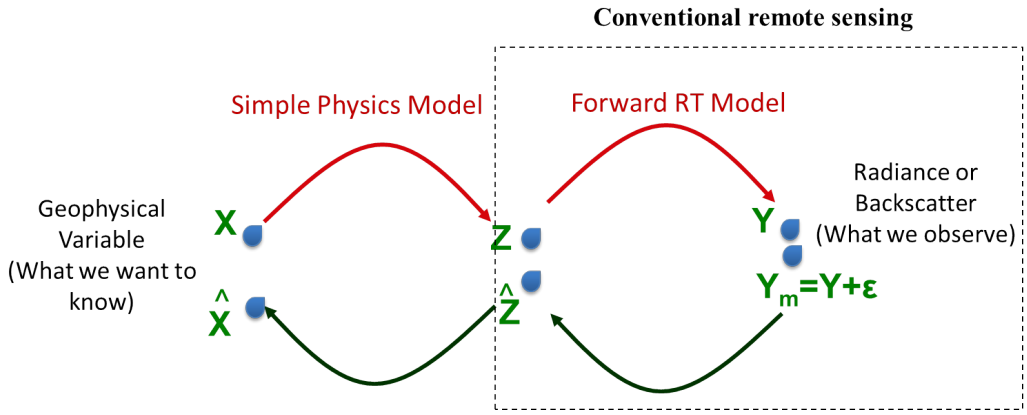

Figure 2.1: A schematic illustrating the concepts of the new algorithms.

2.1 Simple physics model

To understand the driving force of updrafts, we start with the vertical momentum equation:

$$\frac{dw}{dt} = -g - \frac{1}{\rho}\left(\frac{\partial p}{\partial z}\right) + \varepsilon, \qquad (2.1)$$

where w, g, ρ and p represent the vertical velocity, gravitational force, air density and pressure, respectively. The ε is viscous force, which is treated as a constant. Since this study concerns boundary layer clouds, we focus on the turbulent components of the vertical velocity. We expand all the dependent variables in Eq. (2.1) into mean and turbulent parts (e.g., $w = \overline{w} + w'$), which yields:

$$(\bar{\rho} + \rho')\frac{d(\overline{w}+w\prime)}{dt} = -(\bar{\rho} + \rho')g - \frac{\partial(\bar{p}+p\prime)}{\partial z} + (\bar{\rho} + \rho')\varepsilon. \qquad (2.2)$$

Assuming that the mean state is in hydrostatic equilibrium ($\frac{\partial \bar{p}}{\partial z} + g\bar{\rho} = 0$), gives:

$$(\bar{\rho} + \rho')\frac{d(\overline{w}+w\prime)}{dt} = -\rho' g - \frac{\partial p\prime}{\partial z} + (\bar{\rho} + \rho')\varepsilon. \qquad (2.3)$$

Applying Boussinesq approximation yields:

$$\frac{d(\overline{w}+w\prime)}{dt} = -\frac{\rho\prime}{\bar{\rho}}g - \frac{1}{\bar{\rho}}\frac{\partial p\prime}{\partial z} + \varepsilon. \qquad (2.4)$$

In fair-weather boundary layers topped by convective or stratocumulus clouds, the large-scale vertical velocity $\overline{w}$ (<0.1 m/s) is typically one magnitude smaller than the turbulent vertical velocity, w'. So we neglect the large-scale vertical velocity and the Eq. (2.4) becomes:

$$\frac{dw\prime}{dt} = -\frac{\rho\prime}{\bar{\rho}}g - \frac{1}{\bar{\rho}}\frac{\partial p\prime}{\partial z} + \varepsilon. \qquad (2.5)$$

Applying the linearized perturbation ideal gas law (Stull 2012) yields:

$$\frac{dw\prime}{dt} = g\frac{\theta_v\prime}{\overline{\theta_v}} - \frac{1}{\bar{\rho}}\frac{\partial p\prime}{\partial z} + \varepsilon. \qquad (2.6)$$

The terms on the right hand side represent the influences of buoyancy, perturbation pressure gradients, and viscous stress on the motion. In the context of this study, we use the buoyancy term as the main predictor for W_b for the following two reasons. First, both convective clouds and Sc clouds reside in boundary layers that are highly convective. Their maintenance is critically dependent on the generation of convective instability by either surface heating (convective clouds) or cloud-top radiative cooling (Sc clouds). The release of this instability drives buoyancy fluxes that manifest themselves as updrafts. Therefore, in such convective PBLs, the buoyancy term is the dominant driving force of updrafts (Young 1988; Stull 2012; Wood 2012). Second, the perturbation pressure gradients and viscous stress are exceedingly difficult to measure even from the most state-of-the-art instruments. Thus they are poorly quantified. The buoyancy term, on the contrary, is well studied (Deardorff 1970; Young 1988), and it is more feasible to quantify the effects of the buoyancy on driving the updrafts.

Since the buoyancy term in Eq. (2.6) is impossible to be directly computed from satellite data, our strategy is to use conventionally measured parameters to quantify the buoyancy effect. Such quantification is referred to as the "simple physics model". Based on this new concept of W_b estimation, we develop satellite-based methods for inferring the W_b according to the following procedures:

(1) Quantify the W_b using conventionally observed parameters based on theoretical understanding of the mechanisms driving buoyancy in convective boundary layers.

(2) Examine the quantification using high-quality ground-based observations.

(3) Determine any coefficient in the quantification schemes using best-fit regression analysis of the ground-based observational data.

(4) Replace the ground-measured inputs with satellite and reanalysis data to estimate the W_b.

(5) Validate the satellite-estimated W_b against "ground truth" measurements.

In this dissertation, all the W_b retrieval methods (Chapter 3 ~ Chapter 6) were developed based on the above principles and procedures. The succeeding section describes data used in this study. Then I will discuss how to average vertical velocities in a physically based manner so that the retrieved W_b could be most useful for serving our purpose of constraining general circulation models (GCM).

2.2 Data

2.2.1. ARM ground-based data

The "ground truth" observations come from Atmospheric radiation Measurement (ARM) program under the aegis of U.S. Department of Energy (DOE). Observations made at three sites or field campaigns were used (Fig. 2.2), which are the Southern Great Plains (SGP) central facility site, main site of the Green Ocean Amazon (GOAmazon) campaign, and Marine ARM GPCI (Global Energy and Water Cycle Experiment (GEWEX)-Cloud System Study (GCSS)-Pacific Cross-section Intercomparison) Investigation of Clouds (MAGIC) campaign. The details for the three observation sites or field campaigns are described as follows:

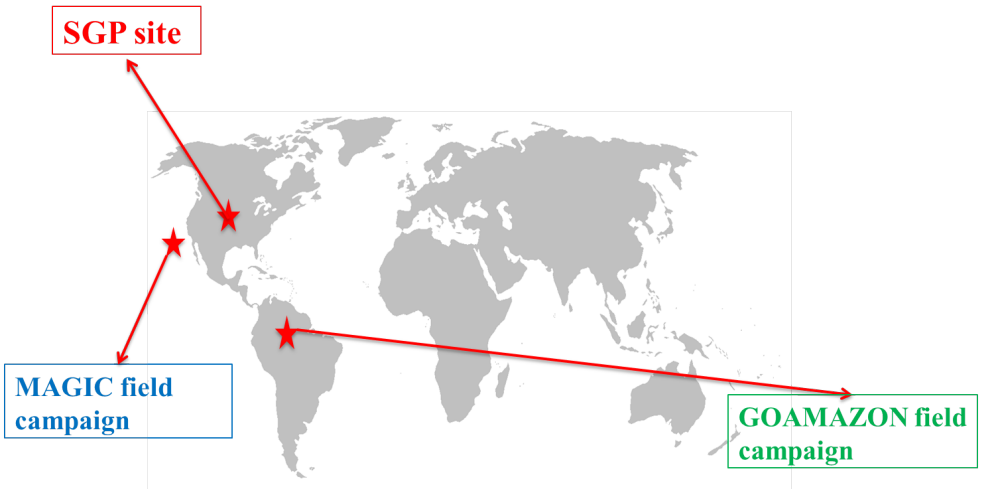

Figure 2.2: Locations of the three observation sites or field campaigns: the SGP site, the MAGIC field campaign, and the GOAMAZON field campaign.

a. SGP site

The SGP central facility site (36.6N, 97.5W) is located to the southeast of Lamont, Oklahoma. The land cover consists of cattle pasture and crop fields. Details of the central facility (CF) site information can be found at http://www.arm.gov/sites/sgp. We used the Doppler lidar (DL) to measure vertical velocity with ~ 1 s temporal and 30 m vertical resolution. The transmitted wavelength is 1.5 μm. Compared with radar, the DL is principally more advantageous in measuring vertical air velocity due to its better precision (better than 0.1 m s^{-1}) and weaker sensitivity to bias by falling rain drops (Zheng et al. 2015).

b. GOAmazon field campaign

The GOAmazon field campaign (http://campaign.arm.gov/goamazon2014/) is conducted over the Central Amazon to the west of the city of Manaus from January

2014 through December 2015. The first ARM Mobile Facility (AMF1) is deployed in the main research site, T3, (3.21S, 60.60W), which is to the north of Manacapuru, Brazil.

c. MAGIC field campaign

The recent MAGIC field campaign (http://www.arm.gov/sites/amf/mag/) lasted from October 2012 through September 2013. The second ARM Mobile Facility (AMF2) was deployed on a container ship, named *Horizon Spirit*, that completed 20 round trips between Los Angeles, California, and Honolulu, Howaii. Due to the dry dock scheduled for the ship, measurements were not made from 12 Jan to 9 May 2013. The AMF2 does not include Doppler lidar, hence we use zenith-viewing Marine W-band (95 GHz) ARM Cloud Radar (WACR) instead to measure vertical velocities. The WACR was deployed on a motion-stabilized platform that compensates for the pitch, roll and yaw of the ship. Ship heave velocity from the Navigational Location and Altitude (NAV) system was used to correct for the vertical velocities of WACR.

Table 2.1 lists the instruments and the measured physical parameters.

Table 2.1: Summary of ARM instruments and measured variables used in this study

Instruments or data products	Measured variables
ARM surface Meteorology System	10-m horizontal wind speed, 2-m air temperature
balloon-borne sounding system (SONDE)[a]	Vertical profiles of the horizontal wind speed and temperature
Planetary boundary layer (PBL) Height Value Added Product[b]	PBL height
Vaisala Ceilometer (VCEIL)	Cloud-base heights
Doppler lidar (DL)[c]	Vertical velocity
Marine W-band (95 GHz) ARM Cloud Radar (WACR)	Vertical velocity in cloud layers
Aerosol Observation System (AOS)	Cloud condensation nuclei concentrations as a function of supersaturation

[a]*The balloon is launched at ~ 1130 local time that is about 2 hours before NPP satellite overpasses.*

[b]*This VAP uses radiosonde as input data to estimate PBL height based on the method developed by Heffter (1980).*

[c]*The DL was not deployed during the MAGIC field campaign.*

2.2.2. Suomi-NPP and reanalysis data

The Suomi National Polar Orbiting Partnership (Suomi-NPP), launched on 28 October 2011, is intended to bridge between the old National Aeronautics and Space Administration (NASA) Earth Observing System (EOS) satellites and the new Joint Polar Satellite System (JPSS) satellites. It carries an imaging instrument, Visible Infrared Imager Radiometer Suite (VIIRS). This instrument provides highly detailed imagery with 5 bands of imagery resolution (375 m) and 17 bands of moderate resolution (750 m). Unlike the 1 km resolution of the infrared (IR) channels of MODerate-resolution Imaging Spectroradiometer (MODIS) and Advanced Very High

Resolution Radiometer (AVHRR), VIIRS has 375 m of spatial resolution in the IR imager bands, which represents a significant improvement over previous instruments.

At the NPP satellite overpass time (~13:30 local time), convective clouds are in the growing stage and are typically well coupled with the boundary layer. This coupling forms convective cloud groups with well-defined cloud bases with heights that change little over scales of several tens of kilometers. Homogeneous convective cloud bases along with high-resolution VIIRS data allow for an accurate estimation of T_b. As illustrated in Figure 2.3, the VIIRS is able to see through the gaps between convective clouds and thus make visible cloud elements at different heights after screening for contamination by surface radiance. The temperature of the warmest cloud pixel corresponds to the T_b. The unique capability of high-resolution NPP/VIIRS in resolving small cloud elements is essential for T_b estimation because it considerably decreases the retrieval errors caused by partial beam (Rosenfeld et al. 2014b). Validation of the VIIRS-retrieved T_b against independently-measured T_b show an excellent agreement with standard error of only 1.1°C (Zhu et al. 2014).

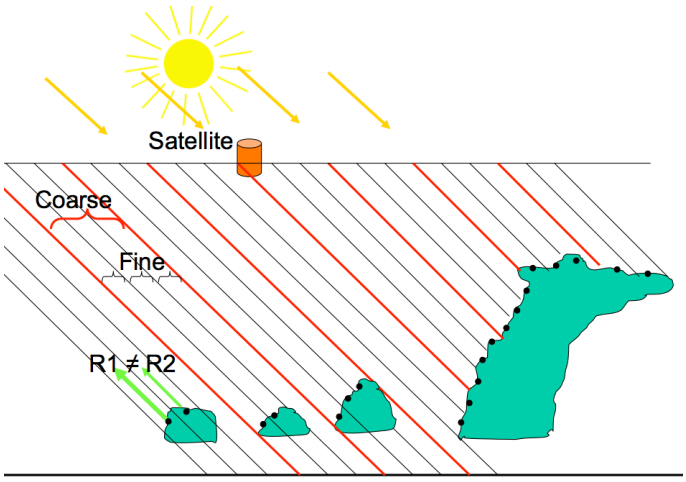

Figure 2.3: A schematic diagram showing how a high spatial resolution is required to resolve the vertical structure of convective clouds. A lower resolution misses all but the largest and deepest clouds. Compared with conventional imagery sensors used before, VIIRS is able to provide much richer information that is yet to be exploited (Hillger et al. 2013).

The datasets from ECMWF ERA-Interim reanalysis (Dee et al. 2011) are used. These include 2-m air temperature, 10-m wind speed, surface geopotential, and vertical profiles of geopotential and wind speeds. The temporal resolution is 6 hours and the spatial resolution is 1.25°×1.25°. Temporal and spatial interpolations are used to spatiotemporally match the NPP/VIIRS data.

2.3 Representation of W_b for computing domain-averaged cloud droplet number

Since our ultimate objective is to constrain GCMs that typically have spatial resolutions of at least several tens of kilometers, W_b that this study concerns is the integrated updrafts over a large domain containing a group of convective clouds or

stratocumulus clouds, not updrafts for a single cloud element. In a convective PBL, updrafts are turbulent and manifest themselves as a distribution of vertical velocities (Figure 2.4). Thus it is necessary to use one single value to represent the integrated effect of all vertical velocities within a large domain on cloud droplet activations. The simplest approach is to average the positive vertical velocities: $\overline{w} = \sum w_i N_i / \sum N_i$, in which the N_i represents the frequency of occurrence of positive vertical velocity w_i ($w_i > 0$). The validity of this simple approach is supported by a number of studies (Meskhidze et al. 2005; Peng et al. 2005; Fountoukis et al. 2007) showing that, within measurement uncertainty, the averaged activated cloud droplet number concentration, $\overline{N_d}$, could be approximated by $N_d(\overline{w})$.

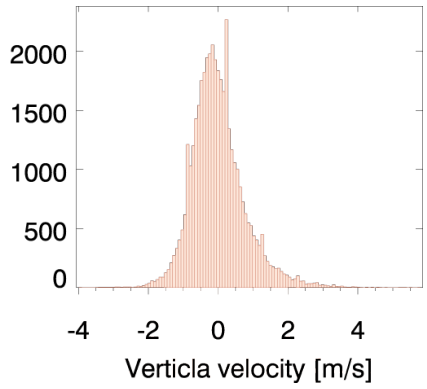

Figure 2.4: Distribution of vertical velocity measured by Doppler lidar over the ARM SGP site. The vertical velocities are measured at cloud bases (1.6 km above ground level) from 19 to 21 UTC on Jun 10, 2012.

This simple average, even though it meets the requirement of $\overline{N_d} \approx N_d(\overline{w})$, is not correct because it neglects stronger updrafts creating larger cloud volumes. This

could be illustrated in Figure 2.5. Twomey (1959) described the roles of updrafts and aerosol number concentration in controlling supersaturation and cloud droplet concentration at cloud bases with an analytical approximation: $N_d(w) = N_{ccn1}^{2/(k+2)} w^{3k/(2k+4)}$, where N_{ccn1} is the cumulative CCN concentration at 1% supersaturation, and k is the slope of CCN supersaturation spectrum in the log-log scale. In k = 0.7 and N_{ccn1} = 600 cm^{-3}, cloud base updrafts of 100 cm s^{-1} and 200 cm s^{-1} are associated with N_d of 377 cm^{-3} and 451 cm^{-3}, respectively. Simply averaging these two N_d values, however, does not give us the correct N_d value for the entire cloud volume because the cloud volume created by the vertical velocity of 200 cm s^{-1} is twice greater than that by the 100 cm s^{-1} vertical velocity.

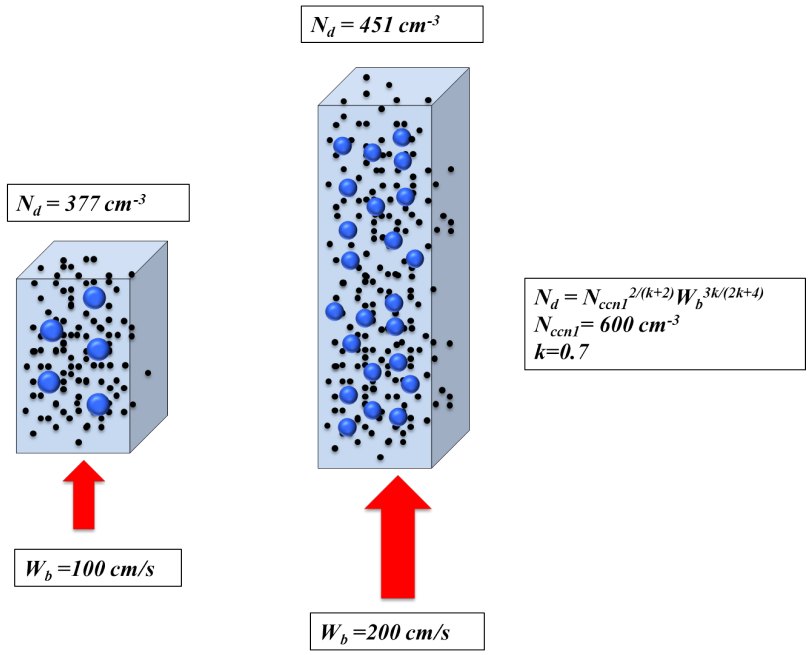

Figure 2.5: Conceptual cartoon illustrating that stronger cloud-base updrafts not only cause greater concentrations of activated cloud droplets but also generate larger cloud volumes per unit time.

Thus, $\overline{N_d}^{\text{vol}}$ (volume-weighted N_d) should be used, which is expressed as:

$$\overline{N_d}^{\text{vol}} = \frac{\sum N_d(w_i)Vol(w_i)}{\sum Vol(w_i)}, \qquad (2.7)$$

in which *Vol* stands for the cloud volume created by w_i in a time unit. For a given distribution of vertical velocity (e.g., Figure 2.4), $Vol(w_i) = \delta s * N_i * w_i$, where δs represents the unit cloud-base area covered by w_i. So equation (2.7) becomes:

$$\overline{N_d}^{\text{vol}} = \frac{\sum N_d(w_i)N_i w_i}{\sum N_i w_i} \quad (2.8)$$

To find a characteristic updrafts w^* that meets:

$$\overline{N_d}^{\text{vol}} = N_d(w^*), \qquad (2.9)$$

we substitute Twomey (1959)'s analytical equation and equation (2.8) to equation (2.9), which yields:

$$w^* = \left[\frac{\sum w_i^{3k/(2k+4)} N_i w_i}{\sum N_i w_i}\right]^{(2k+4)/3k} \qquad (2.10)$$

Figure 2.6 compares the w^* with $\overline{w}$ for two cases. We assume that vertical velocity follows Gaussian distribution, and the two cases represent PBLs with weak (standard deviation, σ, is 0.1 m s^{-1}) and strong (σ =1 m s^{-1}) convections. The result shows that the $\overline{w}$ (red lines) are smaller than w^* (black lines) by ~30% with a slight dependence on *k* and negligible dependence on convection strength. This indicates that the $\overline{w}$ markedly underestimate the effects of updrafts on cloud droplet activations. As a reference, we also plot the $\overline{w}_{Nd}$ (green lines), which is an updrafts speed whose value meets the relation, $\overline{N_d} = N_d(\overline{w}_{Nd})$. It is noteworthy that the difference between the $\overline{w}$ and $\overline{w}_{Nd}$ is markedly smaller than the difference between the w^* and $\overline{w}_{Nd}$, underscoring the significant role of volume-weighting. The importance of volume-weighting led us to examine the volume-weighted updrafts

speed ($\overline{w}^{\mathrm{vol}}$) that is shown by blue lines. Compared with $\overline{w}$, the $\overline{w}^{\mathrm{vol}}$ is much closer to w^* despite a slight overestimation. Figure 2.7 shows that the $\overline{w}^{\mathrm{vol}}/w^*$ ranges between 1.17 for k=0.1 (clean conditions) to 1.05 for k =1.5 (polluted conditions). These values are much closer to unity than $\overline{w}/w^*$ (0.67~0.74) and $\overline{w}_{Nd}/w^*$ (0.51~0.60). Although the $\overline{w}^{\mathrm{vol}}$ is systematically larger than w^*, the slight overestimation is within measurement uncertainty (~0.1 m/s) of Doppler lidar.

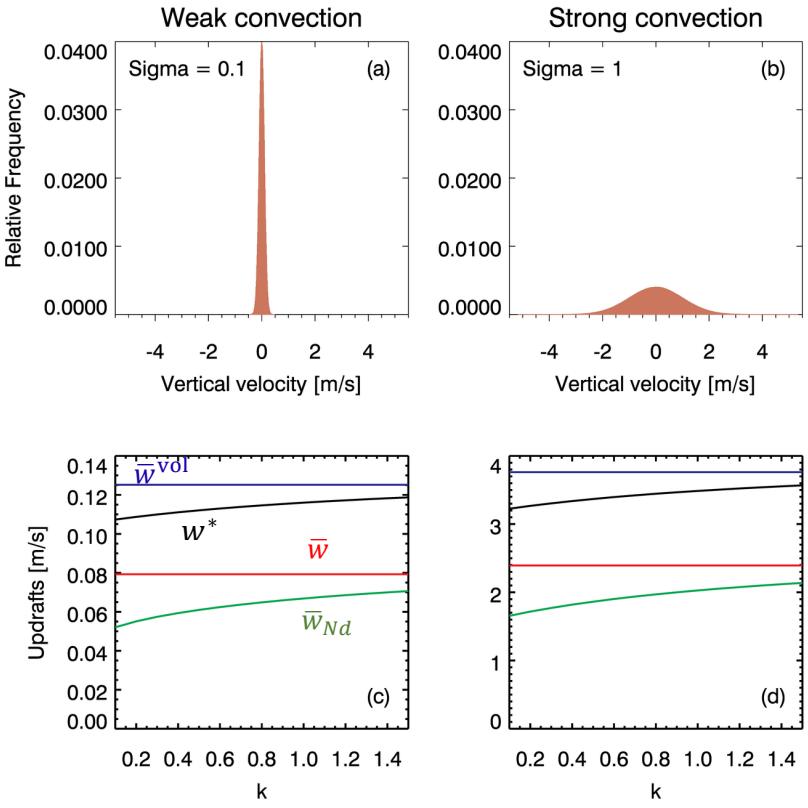

Figure 2.6: Probability density functions (a and b) of vertical velocity (assuming Gaussian distribution), and comparisons between updrafts averaged in different ways (c and d) for weakly and strongly convective PBLs. In (c) and (d), blue, black, red and green lines represent $\overline{w}^{\mathrm{vol}}$, w^*, $\overline{w}$ and $\overline{w}_{Nd}$ as a function of k, respectively.

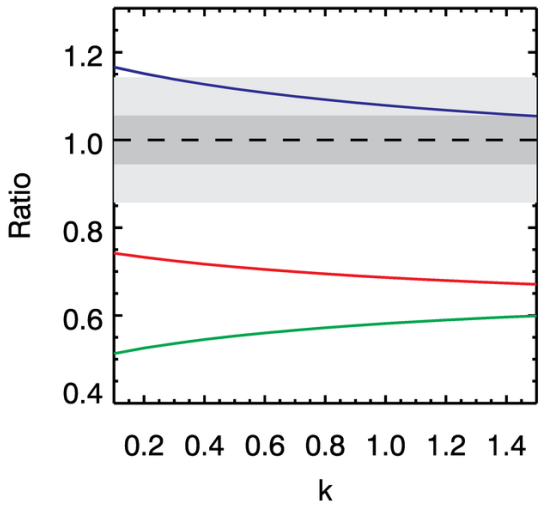

Figure 2.7: Comparisons between $\overline{w}^{\mathrm{vol}}/w^*$ (blue), $\overline{w}\ /w^*$ (red) and $\overline{w}_{Nd}/w^*$ (green) as a function of *k*. The horizontal dashed line marks the unity. The shadings mark the measurement uncertainties of ARM Doppler lidar (~0.1 m/s). The contribution of ~0.1 m/s uncertainty in vertical velocity to percentage error depends on updrafts strength, ranging from 33% for weak updrafts (0.3 m/s) to 3.3% for strong updrafts (3 m/s). The mean value of the $\overline{w}^{\mathrm{vol}}$ for all the cases surveyed in this study is 1.1 m/s with standard deviation of 0.4 m/s. The light and heavy grey shadings correspond to the mean value minus and plus a standard deviation, respectively.

In summary, the volume-weighted updrafts speed ($\overline{w}^{\mathrm{vol}}$) is superior to averaged updrafts speed ($\overline{w}$) in terms of the ability to represent the updrafts effect on cloud droplet activations. Thus W_b is calculated in the same way as the $\overline{w}^{\mathrm{vol}}$, which is:

$$W_b = \overline{w}^{\mathrm{vol}} = \frac{\sum N_i w_i^2}{\sum N_i w_i}, \qquad (2.11)$$

where the $w_i > 0$.

Chapter 3 Satellite inference of updrafts for convective clouds

In this chapter, two complementary methods (Zheng and Rosenfeld 2015; Zheng et al. 2015) were developed for inferring W_b of convective clouds. Recalling section 2.1 in Chapter 2, these methods are established on our fundamental understanding of the dominant force (buoyancy) driving convective updrafts, which helps parameterize them using quantities that are either retrievable from satellite or available from sound-quality reanalysis data.

In the next section, I will describe the methodology for deriving the W_b and the maximum updrafts in the vertical (W_{max}) using ARM Doppler lidar. The two methods for W_b retrieval are described in section 3.2 and 3.3, respectively. For each method, the procedure for algorithm development follows the steps listed in section 2.1. A summary is given in section 3.4.

3.1 Updraft speed calculation with Doppler lidar measurements

The validity of Doppler lidar retrieval of PBL parameters has been demonstrated in multiple studies (Tucker et al. 2009; Ghate et al. 2013). Doppler lidar was used to measure the vertical velocity of aerosol particles from 15 m above the ground to the top of the PBL with ~ 1 s temporal and 30 m vertical resolution. The transmitted wavelength is 1.5 μm. There are several advantages to using coherent Doppler lidar to retrieve vertical velocity. First, Doppler lidar uses aerosol particles as atmospheric scattering targets. Aerosol particles are excellent tracers of air motions. In contrast to radar, lidar is capable of measuring wind velocities under clear-sky conditions with very good precision (better than 0.1 m s^{-1}). Second, taking advantage

of the Doppler frequency shift, Doppler lidar provides a large Nyquist interval of 19 m s^{-1} for vertical velocity, which is three times larger than that for radar at the SGP site. Third, lidar-retrieved velocity is much less sensitive to bias by falling rain drops than is radar-retrieved vertical air velocity.

Figure 3.1 presents three representative convective PBLs (24 March 2013, 25 Jun 2013 and 2 February 2013). The vertical red lines in the left panels mark the NPP satellite overpass time in order to temporally match the ground-based measurements. As denoted by the boxes in the height-time displays of lidar vertical velocity data (left panels), one-hour Doppler lidar pixels of vertical velocity within 200-m layers were used to calculate the updraft velocity using Eq. (2.11). In cloudy conditions, we selected a two-hour (rather than one-hour) time window that centers on satellite overpass time for cloud base updraft calculation in order to include more cloudy pixels. Admittedly, the selection of 1- or 2-hour time window is somewhat arbitrary. Sensitivity tests (not shown) suggest that the computed updrafts are not sensitive to the time window if the selected time window captures several convective cells that pass overhead, which corresponds to 1~2 hours. If the time window is too short, say 10 minutes, it cannot even capture a complete thermal so that the insensitivity will not hold anymore. Another reason to use long time window (1~2 hours) is that a sufficient number of lidar samples can be collected to represent the updrafts on a large scale. A horizontal wind speed of 5~10 m s^{-1} integrates over spatial scale of several tens of km within 1~2 hours, which is comparable to the grid size in a GCM. To visualize the PBL top (the top boxes in the left panels of Fig 3.1) and rule out noise, pixels with signal-to-noise ratio (SNR) - which is calculated as the ratio of the

integrated signal to the noise floor integrated over the passband - less than 0.012 were excluded. We test the sensitivity of the updraft velocity to SNR threshold and found that the retrieved updrafts are highly independent to the threshold for SNR at height levels within the PBL top for 85% cases (not shown). However, this insensitivity diminishes when PBLs are very deep (> 2.5 km). Indeed, the insensitivity is not present in 9 out of 84 clear cases and 8 out of 28 cloudy cases. In the upper part of the deep PBL, lidar returns are sometimes very weak because returning signals are mostly attenuated due to long distance between lidar and aerosol particles. In this situation, lidar updraft signals are usually indistinguishable from noises; too many useful pixels are removed with increasing SNR threshold. In order to solve this problem for deep PBL cases, we developed a new technique that filters out noise with relatively minor signal loss (see *appendix A*).

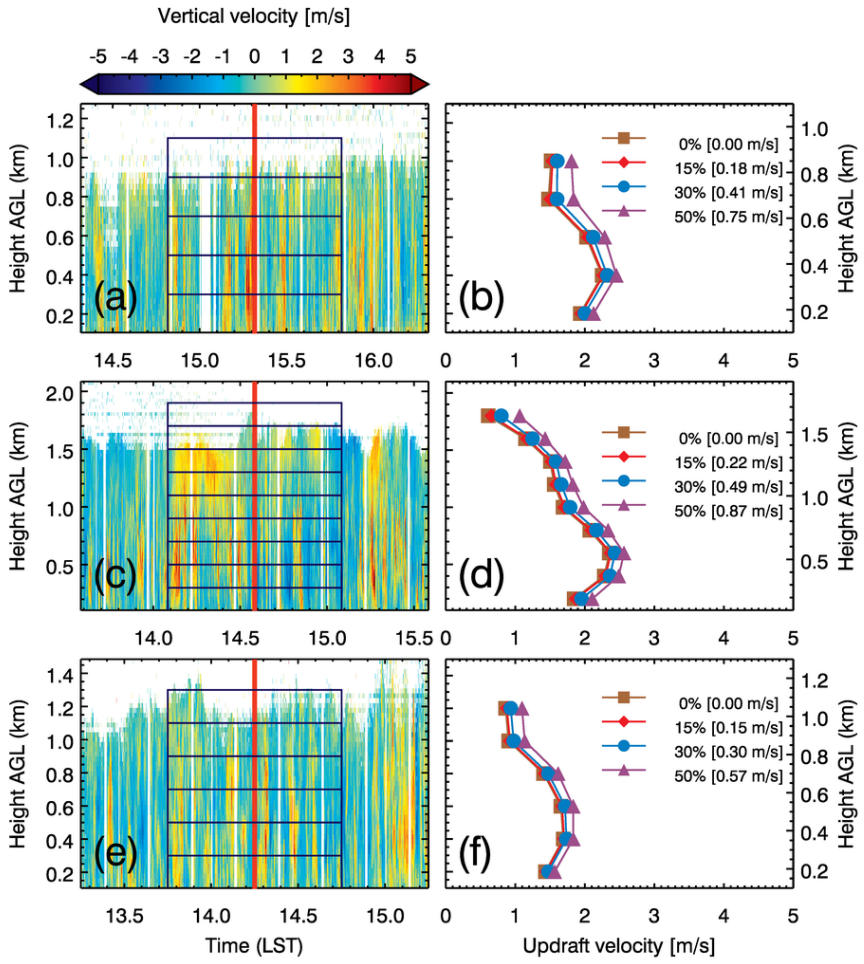

Figure 3.1: Three representative cases on (a, b) 24 March 2013, (c,d) 25 Jun 2013 and (e, f) 2 February 2013. Left panels are height-time display of vertical staring data from Doppler lidar in SGP site. Signal-to-noise ratio (SNR) is set to 0.012 to visualize the PBL tops. Red lines mark the NPP overpass time. Black rectangles denote the height-time areas within which vertical velocity pixels are selected for updraft speed calculation using Eq. (2.11). Right panels are corresponding calculated updraft speeds at each height for different percentiles of vertical velocity (0%, 15%, 30% and 50%). The values in the brackets denote the corresponding threshold vertical velocity used to define updraft.

Although the W_b is the primary focus, we start with W_{max} that is the maximum updraft speed in the vertical. The reason is that the W_{max} occurs at altitudes where the assumption of buoyancy dominantly driving updrafts is best fulfilled. As shown in Figure 3.1, updrafts speed initially increases with altitude, which is driven by buoyancy. After reaching its maximum, the updrafts speed start to decrease. Such decrease is caused by increasingly stronger entrainment when the thermals are approaching the PBL top, dilution of the thermals with environmental air, and drag effects. All these effects are extremely difficult to be quantified, but they contribute to the W_b. As such, we first study the W_{max} that is least affected by these effects. Then we will expand the results from W_{max} to W_b.

3.2 "Temperature-gradient" method

3.2.1 Simple physics model

The dominant role of buoyancy was quantitatively reflected by well-known convective velocity scale w_* introduced by Deardorff (1970), which is written as:

$$w_* = [\frac{gz_i}{T_v}\overline{(w'T_v')}_s]^{1/3} , \qquad (3.1)$$

where g is the acceleration of gravity, z_i is the PBL height, T_v is the mixed-layer mean virtual temperature, and $\overline{(w'T_v')}_s$ stands for the vertical kinetic heat flux near the surface. The convective velocity scale has been demonstrated to effectively scale turbulence velocities in experimental studies (Kaimal et al. 1976; Druilhet et al. 1983), and other studies have used this scale to estimate the quantitative structure of updrafts of the convective PBL by observation (Manton 1977; Lenschow and

Stephens 1980; Greenhut and Singh Khalsa 1982, 1987; Chandra et al. 2010) and modeling (Schmidt and Schumann 1989).

Thus, the convective velocity scale constitutes an alternative means of estimating vertical velocity using PBL height z_i and surface heat flux $\overline{(w'T_v')}_s$ in the convective PBL. However, great uncertainties in surface heat flux estimation represent a serious barrier to a useful estimation of convective velocities. We address this practical problem by approximating the effects of surface heat flux using ground-air temperature difference and surface wind as proxies for surface heat fluxes. According to the traditional model first proposed by Taylor (1960), the vertical kinematic heat flux near surface $\overline{(w'T_v')}_s$ is proportional to the wind speed multiplied by the temperature difference between the ground and the air, which could be expressed by a bulk aerodynamic formula:

$$\overline{(w'T_v')}_s = C_H V(T_s - T_a), \qquad (3.2)$$

where C_H is the bulk transfer coefficient, V stands for the mean surface wind speed, and T_s and T_a are surface skin temperature and air temperature at a reference level (typically 2 meters above the ground), respectively. According to Eq. (3.2), fluxes approach zero in the limit of calm winds, which is unlikely to happen in the real atmosphere. In the convective PBL, the well-mixed layer is usually capped by an inversion layer. When thermals approach the inversion base, they will gradually lose their buoyancy due to downward heat flux, spread out laterally, and then fall back into the mixed layer as downdrafts, forming convective circulation (Fig. 3.2). In this case, even when the horizontal mean vector wind is zero, the horizontal mean scalar

wind should be non-zero because of the near-surface random perturbation gusts caused by convective circulation (Deardorff 1972; Schumann 1988).

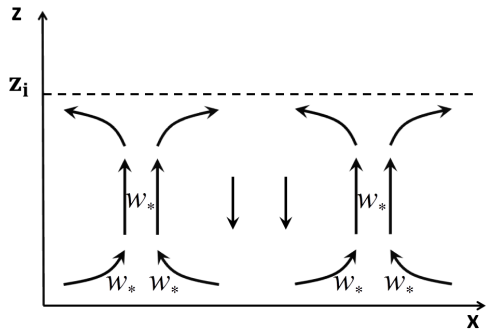

Figure 3.2: Schematic of idealized convective circulation, adapted from Stull (1988). The updraft velocity and surface-layer gusts have a magnitude of w_*, according to the Deardorff convective scale.

The vector velocity of the horizontal gust speed in the surface layer is usually assumed to be of order w_* (Businger 1973; Schumann 1988). This modifies Eq. (3.2) in the following way:

$$\overline{(w'T_v')_s} = C_H(V + w_*)(T_s - T_a), \quad (3.3)$$

which is similar to an expression proposed by *Stull* (1994).

Under the condition of free convection, where the turbulent energy is generated by buoyancy forces and where the mean horizontal wind vanishes, Eq. (3.3) reduces to:

$$\overline{(w'T_v')_s} = C_H w_*(T_s - T_a). \quad (3.4)$$

Substituting (3.4) into (3.1), we have:

$$w_* = [\frac{gz_i}{T_v} C_H (T_s - T_a)]^{1/2} \qquad (3.5)$$

Equation (3.5) shows that the scale of convective velocity is proportional to the square root of the product of PBL height and ground-air temperature difference in the regime of extreme free convection.

3.2.2. Examining the simple physics model using ARM observations

3.2.2.1.Clear boundary layer

Based on Eq. (3.5), the convective velocity scale should be linearly proportional to the square root of the product of z_i and the ground-air temperature difference (T_s - T_a). Based on this theoretical relation, we assume:

$$W_{est} = B_1[z_i(T_s - T_a)]^{1/2} + B_2, \qquad (3.6)$$

where B_1 and B_2 are coefficients that could be assumed as constants here, although they may be functions of other factors affecting updraft speeds such as air drag, surface wind speed and PBL wind shear. We determine the value of B_1 and B_2 by taking the linear regression analysis between lidar-measured W_{max} and observed $[z_i(T_s - T_a)]^{1/2}$. The T_a and z_i are obtained from ARM ground-based measurements (Table 2.1). T_s is provided by VIIRS Land Surface Temperature (LST) Environmental Data Record (EDR), at a spatial resolution of ~ 0.75 km at nadir and ~1.3 km at the edge of the swath. The LST EDR products are averaged within an 0.25°×0.25° area. Considering the advection of thermals by horizontal winds, we calculate the 1-hour vector-mean of 10-m wind direction and select the 0.25°×0.25° region for averaging upwind from the SGP site. Using data quality flags, we discard

samples that are contaminated by thin cirrus. The reason we use spatial averages of satellite-retrieved T_s instead of ARM surface measurements of T_s is that the T_s depends highly on surface type and any single point measurements of T_s cannot represent large-scale surface forcing that drives the updrafts. With the value of the coefficients ($B_1 = 0.24$ and $B_2 = 0.99$) and observed $[z_i(T_s - T_a)]^{1/2}$, we calculate the W_{max} and validate it by lidar-observed W_{max} (Fig. 3.3). The correlation coefficient (R) is 0.74 and the RMSE is 0.34 m s^{-1}. When the surface wind speed is large (V > 6.7 m s^{-1}), on the one hand, the correlation coefficient decreases due to the decreasing robustness of the free convection assumption. On the other hand, updraft speeds for strong wind cases tend to be underestimated, which is consistent with the idea that enhanced shear-driven eddies facilitate the transport of heat in the surface layer, increasing buoyancy and hence updraft speed.

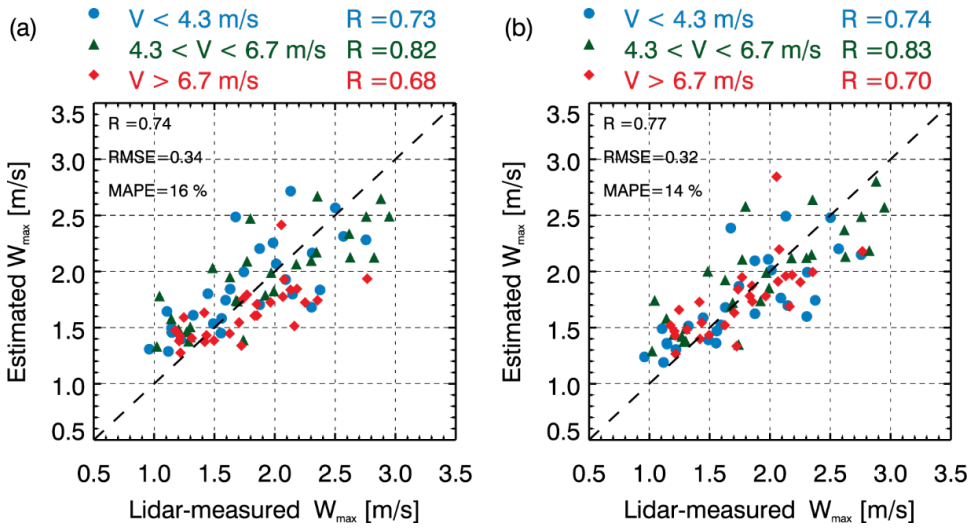

Figure 3.3: Comparisons between lidar-measured W_{max} and (a) estimated W_{max} based on Eq. (3.6) without the surface wind and (b) estimated W_{max} based on Eq. (3.7) which corrects for the surface wind. The R, RMSE and MAPE are given for the full datasets in each figure. Both correlations are significant at the 99.9% confidence level based on t-test.

Hence, taking into account surface wind speed as well as ground-air temperature difference and PBL height results in a more universal estimation of updraft speed. Given the complex and possibly chaotic impacts of mechanical turbulence on thermals, the incorporation of surface wind speed into Eq. (3.6) in a way that has a physical basis seems a daunting task. Here, we only consider the facilitating effect of mean wind on the vertical transport of heat in the surface layer. In Eq. (3.6) that is based on the free convection assumption, (T_s - T_a) characterizes the transport of heat caused by temperature gradient. Assuming that wind-induced transport of heat, characterized by $V(T_s$ - $T_a)$ based on Taylor's formula (1960), is

quasi-independent of transport action resulting from temperature gradient (T_s - T_a), we perform a linear superposition of these two terms, yielding:

$$W_{est} = C_1[z_i(1 + C_M V)(T_s - T_a)]^{1/2} + C_2, \quad (3.7)$$

where C_1 and C_2 are coefficients. C_M is mechanical transport coefficient for heat, the value of which is found empirically to be 0.25 (Fig 3.3b) by taking the linear regression between W_{max} and $[z_i(1 + C_M V)(T_s - T_a)]^{1/2}$ with the use of different values of C_M and selecting the value corresponding to the largest R. Apart from physical considerations, another reason we include wind speed in our method in the form of Eq. (3.7) is that it accounts for situations wherein surface mean wind ceases. In fact, in calm wind conditions where wind speed approaches zero, Eq. (3.7) reduces to Eq. (3.6), and our method still works with a valid theoretical basis. The W_{max} estimated by Eq. (3.7) is in statistically better agreement with lidar-measured W_{max} than that by Eq. (3.6) according to the larger R, smaller RMSE and smaller MAPE (Fig 3.3b). In addition, points with different wind speeds distribute more uniformly in Fig 3.3b than in Fig 3.3a, further confirming the universality of using Eq. (3.7) to estimate updraft speeds.

After demonstrating the effects of shear-induced eddies on enhancing the heat flux in the surface layer, it is informative to see if mechanical eddies play a role in the well-mixed layer. Here we use the wind shear (WS), calculated by dividing the horizontal wind speed difference between PBL top and surface by PBL depth, to characterize the mixed-layer mechanical eddies. Then, we examined the variation of ratio of estimated W_{max} by Eq. (3.7) to measured W_{max} with wind shear, and found no correlation (not shown). This indicates that for clear PBL the accuracy of our method

for estimating W_{max} is not affected by PBL wind shear. Actually, the wind shear and surface wind speed (V) are not independent. Much of the wind shear effect may already be accounted for by V in Eq. (3.7).

3.2.2.2.Cloud-topped boundary layer

Cloud behavior is regarded as an important factor in the modification of subcloud-layer (well-mixed layer) dynamic systems (Stull 1985; Neggers et al. 2006). However, due to the complicated processes and feedbacks in this coupled system of cloud and subcloud layers, a well-established theoretical framework quantifying the impacts of cloud behavior on subcloud-layer updrafts is still missing. Does our algorithm for estimating W_{max} also apply to cloud-topped PBL? The answer is yes, as shown in Figure 3.4. Figure 3.4 show the W_{max} estimated based on Eq. (3.7), validated by lidar-measured W_{max} in cloudy condition (black lines and dots). In cloudy cases, although the satellite cannot retrieve the surface temperature under clouds, convective clouds always leave holes between them with valid LST data, which are averaged in the 0.25°×0.25° area to calculate the T_s. In addition, we use the cloud base height H_b to replace the z_i in Eq. (3.7) since H_b is easier to retrieve from a satellite with satisfactory accuracy (this will be demonstrated in section 3.2.3). Here it should be emphasized that the assumed equality of PBL height and H_b may not always be valid. Nonetheless, according to the theory introduced in section 3.2.1, the PBL top is identified with the height that thermals can reach. The processes pertaining to wet thermals, driven partially by latent heating in cloud, are beyond the scope of the theory considered in this study. Therefore, when clouds are present, the cloud base

height, which is at the top of the dry thermals, is a valid approximation of PBL height at least for this specific study.

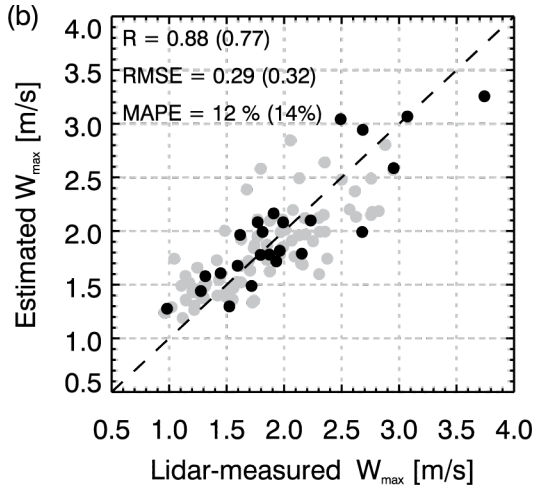

Figure 3.4: Comparisons between lidar-measured W_{max} and estimated W_{max} based on Eq. (3.7) for cloudy (black) and clear (gray) PBL cases. Because Doppler lidar observations are not available for 4 of the 28 cloudy cases, only 24 cases were plotted. The R, RMSE and MAPE are given for the datasets corresponding to black points and gray points in each figure. Values in the parentheses correspond to gray points.

Comparison of estimated updraft speeds in cloudy (black lines and dots) and clear PBL (gray lines and dots) suggests that in cloud-topped PBL we can estimate W_{max} with relatively better agreement with lidar-measured W_{max} in view of R, RMSE and MAPE. This is consistent with the idea that convective circulation is more likely to be well-formed when convective clouds are present. Generally, thermals produced from surface heating may die before reaching the PBL top. This is caused mainly by the entrainment of environmental air into the rising thermals. When clouds are

present, there must be thermals with sufficient intensity to reach cloud base to trigger them in the first place.

Figure 3.5 shows that unlike in clear-sky conditions, cloud-topped PBL wind shear appears to affect updraft speeds. With the enhancement of wind shear, the ratio of updraft speed estimated by Eq. (3.7) to lidar-measured updraft speed decreases. A negative correlation coefficient of -0.42 was found, which is statistically significant at the 95% confidence level based on *t*-test. In other words, we tend to overestimate the W_{max} when the wind shear is strong. A possible explanation may be that the shear-induced eddies can rip thermals apart, thus weakening updraft speeds. The more well-formed convective circulation under cloudy conditions amplifies the signal of wind shear's impact on thermals that cannot be detected in clear-sky conditions. In addition, the deeper PBL (1.59 km on average for cases in this study) for cloudy conditions than for clear conditions (1.19 km on average) provides more room for shear-induced mechanical eddies to impinge on the thermals.

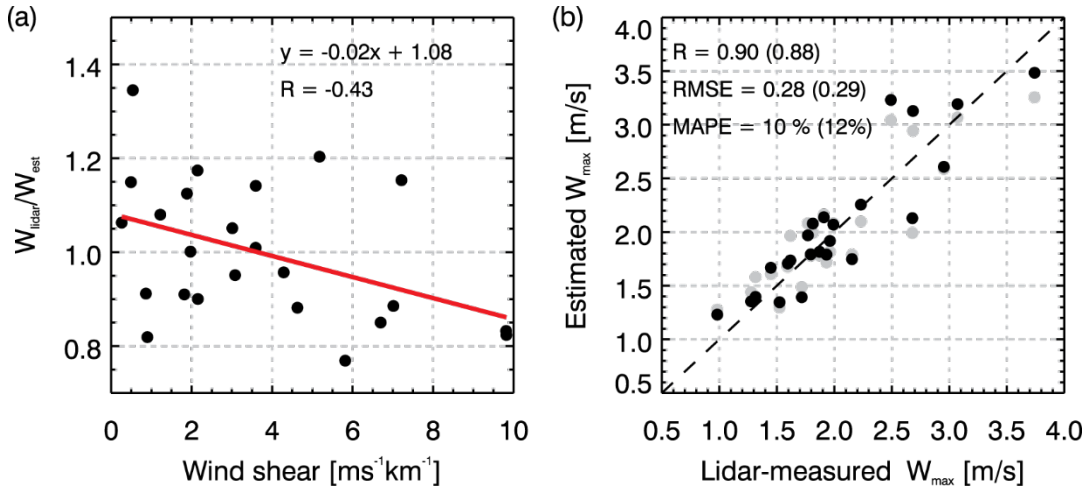

Figure 3.5: (a) Variation of ratio of lidar-measured W_{max} to estimated W_{max} with wind shear for cloud-topped PBL conditions. The R and best-fit line are given. The correlation is significant at the 95% confidence level. (b) Comparison between lidar-measured W_{max} and estimated W_{max} based on Eq. (3.8) which applies a wind shear correction (black) and Eq. (3.7) which does not correct for wind shear (gray). The R, RMSE and MAPE are given for the datasets corresponding to black points and gray points in each figure. Values in the parentheses correspond to gray points.

To take advantage of the above-noted finding, we simply multiply the right side of Eq. (3.7) by the regression equation between wind shear and the ratio of updraft speed estimated by Eq. (3.8) to lidar-measured updraft speed, to yield the following equation:

$$W_{est} = (D_1 WS + D_2)\{C_1[z_i(1 + C_M V)(T_s - T_a)]^{\frac{1}{2}} + C_2\}, \quad (3.8)$$

where D_1 and D_2 are coefficients for wind shear correction. For W_{max} estimation in cloudy PBL, $D_1 = -0.02$ and $D_2 = 1.08$, as shown in Fig 3.5a. Figure 3.5b shows

the slightly improved estimation of W_{max} by Eq. (3.8) (black lines and dots) compared with that by Eq. (3.7) (gray lines and dots) in terms of R, RMSE and MAPE.

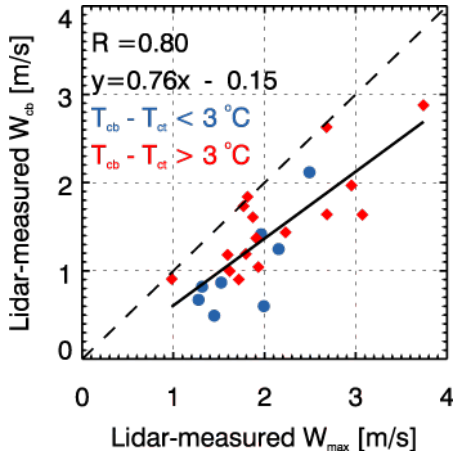

Figure 3.6: Comparison between lidar-measured W_b and W_{max}. The R and best-fit line are given for the full datasets.

Compared to W_{max}, cloud base updraft speed, W_b, is of greater interest because of its significant impact on the formation and evolution of convective clouds (see the introduction). Figure 3.6 shows a statistically significant correlation (R=0.80) of W_b with W_{max} in cloud-topped PBL. The W_b is smaller than W_{max}, which is primarily attributable to a stabilizing of the environment near the top of the mixed layer, though dilution with environmental air and drag may also play a role. We use the temperature difference between satellite-retrieved cloud base and cloud top, $T_b - T_t$, to identify cloud thickness. All 24 cloudy cases here are divided into three equal-sized subsets differentiated by ($T_b - T_t$), and each subset contains 8 cases. Based on the limited number of cases, we roughly classify the clouds of the three subsets as thin ($T_b - T_t <$ 3 ºC), medium-thick (3 ºC < $T_b - T_t$ < 11 ºC) and thick ($T_b - T_t >$ 11 ºC) clouds. Blue points correspond to thin clouds and red points represent the medium-thick and thick

clouds. Comparison of these two subsets of cases suggests that on days with thin clouds the W_b tends to be significantly smaller than W_{max}, whereas for other cases W_b is comparatively more consistent with W_{max}. This systematic distinction is illustrated in Fig. 3.7. The thin clouds (left) are usually topped by a strong inversion layer to prevent them from developing. The highly negative buoyancy induced by the strong inversion remarkably decelerates the updraft speeds as they reach cloud base, resulting in a much smaller W_b than W_{max}. In the meantime, the inability to quantify the effects of the entrainment makes it more difficult to estimate the W_b after such deceleration, which indicates that if the satellite-retrieved (T_b – T_t) is small, the estimated W_b is less reliable. For the clouds with medium or long vertical extent, the updrafts are less influenced by the stabilizing of the entrainment layer. The air rising in the thermals can continue to ascent through the cloud base and circulate through the cloud. In this situation, W_b is more consistent with W_{max}.

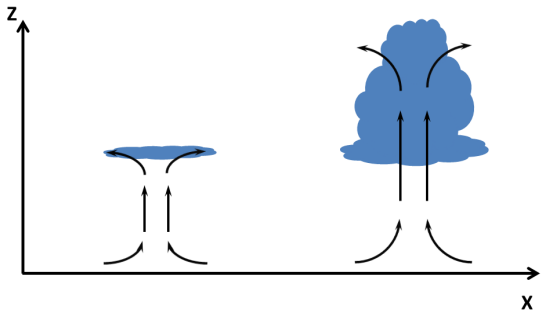

Figure 3.7: Schematic diagram showing the difference in convective circulation between thin clouds (left) and clouds with medium and deep extent (right).

Given the statistically significant correlation between W_{max} and W_b, we assume that the approaches for estimating W_{max} introduced in this study are also applicable for W_b estimation. Following the same procedure as for estimating W_{max}, we estimated W_b with similar Eq. (3.8) but with different values of the coefficients (Table 3.1). The validation result is presented in Fig.3.8, which shows a correlation coefficient of 0.74 and a MAPE of 24%. This demonstrates a useful performance of our method and provides a possibility of estimating W_b based on observed surface and PBL parameters (V, H_b, T_s, T_a, and WS). In fact, if we use the calculated W_{max} as an intermediate parameter and the linear regression equation between W_{max} and W_b for estimating W_b (gray points in Fig. 3.8), the results are very similar to the direct estimation of W_b (black points). This supports the assumption that the method for estimating W_{max} also works for W_b.

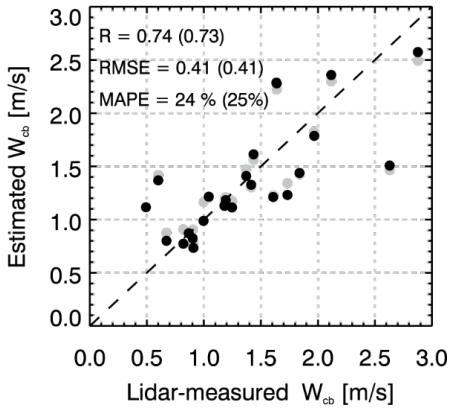

Figure 3.8: Validation of estimated W_b based on surface and PBL parameters (equation 3.8) against lidar-measured W_b. The black and gray points correspond to W_b calculated directly and W_b estimated with the intermediate calculation of W_b, respectively.

Here, as shown in Table 3.1, we summarized all the values of the coefficients in Eqs. from (3.6) to (3.8), which are used to estimate the updraft speeds in clear and cloudy PBLs.

Table 3.1: Summary of coefficients used in updraft estimations

Equation Number	Estimated parameters (in clear or cloudy PBL)	Coefficient value	Coefficient value
3.6	W_{max} (clear)	B_1 = 0.24	B_2 = 0.99
3.7[a]	W_{max} (clear)	C_1 = 0.17	C_2 = 0.93
	W_{max} (cloudy)	C_1 = 0.27	C_2 = -0.18
	W_b (cloudy)	C_1 = 0.20	C_2 = 0.26
3.8[b]	W_{max} (cloudy)	D_1 = -0.02	D_2 = 1.08
	W_b (cloudy)	D_1 = -0.04	D_2 = 1.13

[a] *C_M=0.25 for Eqs. (3.7) and (3.8)*

[b] *In Eq. (3.8), the values of C_1 and C_2 are identical to those in Eq. (3.7) for W_{max} and W_b estimations in cloudy PBL.*

3.2.3. Validation against "ground truth" measurements

We have theoretically derived the estimation equations with coefficients being empirically determined. To test the potential for satellite-based application of this relationship, we utilize the ECMWF reanalysis and VIIRS-retrieved data to estimate the inputs for retrieving W_b by the following:

1. T_s was retrieved by VIIRS/NPP in the same way mentioned in section 3.2.2.

2. T_a and V are obtained from ECMWF reanalysis 2-m air temperature and 10-m wind product, respectively.
3. H_b is retrieved based on VIIRS-retrieved T_b and the air temperature product at 2-m height from the ECMWF reanalysis. We assume that the 2–m air temperature decreases at a dry adiabatic lapse rate until it reaches T_b. The height corresponding to T_b is the H_b .
4. Wind shear can be obtained with retrieved H_b and vertical profile of wind speed from ECMWF reanalysis.

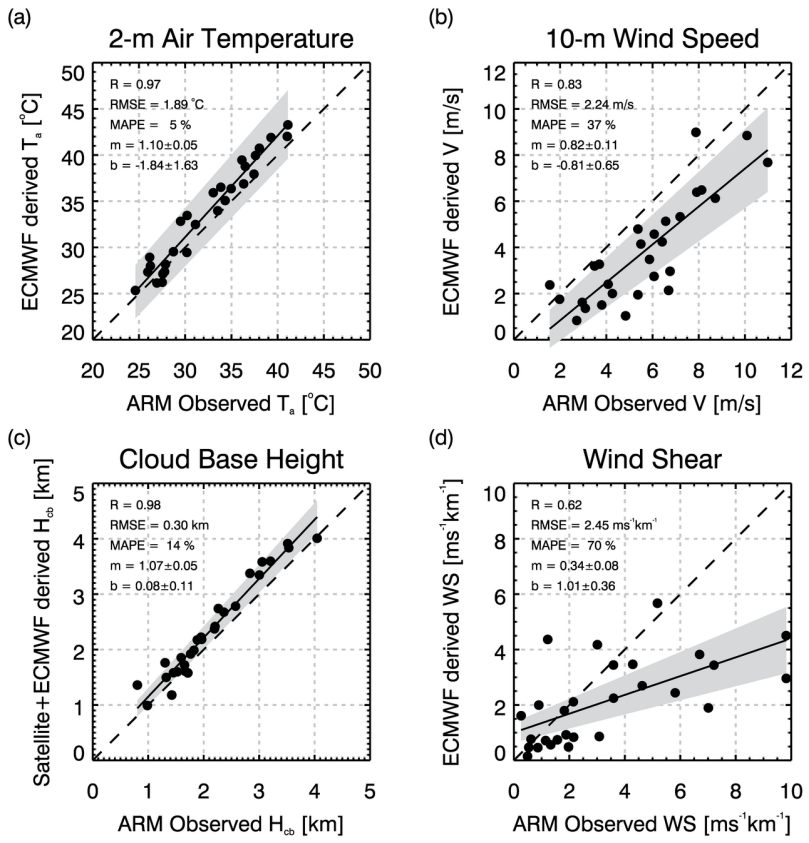

Figure 3.9: Comparison between ECMWF- and satellite-derived parameters and those from ARM observation for (a) 2-m temperature, (b) 10-m wind speed, (c) cloud base

height obtained by adiabatic cooling of the surface air temperature to satellite-retrieved cloud base temperature, and (d) wind shear.

The four parameters derived from satellite and reanalysis data are compared with ARM measurements over the SGP site and shown in Figure 3.9. Good agreements were found for H_b and T_a with correlation coefficient of 0.97 and 0.98 respectively. The RMSE is 1.89 °C for T_a and 300 m for H_b, which correspond to MAPE of 4% and 13%, respectively. The good agreement for H_b largely benefits from accurate 2-m air temperature from reanalysis and reliable satellite retrieval of cloud base temperature (RMSE = 1.1 °C). Compared with 2-m air temperature, the estimation of 10-m horizontal wind speed derived by reanalysis is much worse (MAPE = 38%). This can be attributed primarily to the fact that the spatial distribution of horizontal wind speed is much less continuous than that for surface air temperature, in which condition the spatial interpolation will produce larger errors for 10-m wind speed from reanalysis. The quantity least accurately estimated is the wind shear. This is partially caused by high spatial variability of wind speeds measured by instruments onboard the observing platform tethered to the balloon, whereas the vertical profile of ECMWF-based wind speed has already been smoothed. This inconsistency leads to a large discrepancy between SONDE-measured and ECMWF-derived wind shear. Applying these satellite-retrieved parameters and Eq. (3.8), we estimate the values for W_{max} and W_b and compare them with those measured by lidar (Figure 3.10). The RMSEs (MAPEs) are 0.32 m s^{-1} (12%) and 0.42 m s^{-1} (24%) with respect to W_{max} and W_b, respectively. The effect of wind shear from reanalysis on constraining the estimations is negligible as the metrics evaluating the estimated

updrafts are nearly the same for updrafts estimated using Eqs. (3.7) and (3.8). It is interesting to see that the accuracy of satellite-retrieved updrafts is comparable to that retrieved by ground measurements that are expected to be more reliable. The surprisingly good performance of satellite retrieval benefits greatly from the area of coverage of the input variables retrieved by satellite or reanalysis. The satellite-retrieved updrafts are therefore on large scale, which spatially match the scale of the lidar-measured updrafts. The validation results are encouraging. It bolsters our confidence in utilizing satellites, augmented by reanalysis data, to estimate updraft speeds in convective PBL with satellite coverage of large areas.

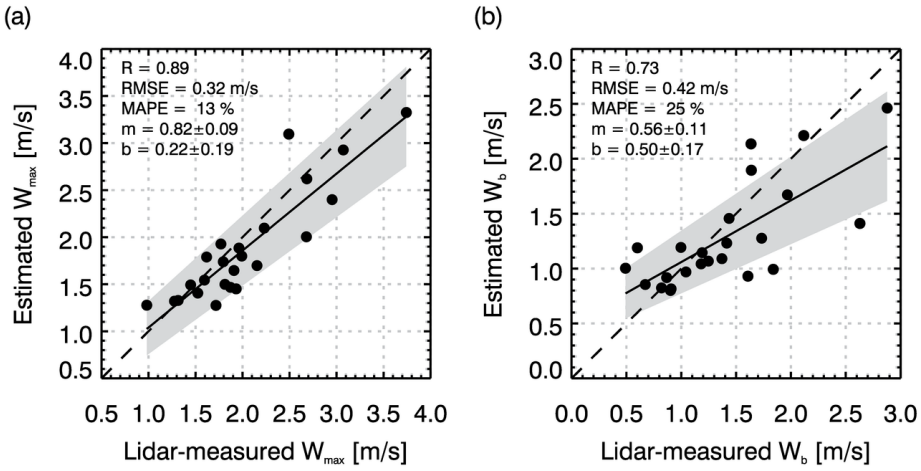

Figure 3.10: Validation of satellite-estimated W_{max} (a) and W_b (b) based on Eq. (3.8) against those measured by Doppler lidar. The R, RMSE and MAPE are given for the datasets corresponding to black points and gray points in each figure.

3.2.5.Uncertainty analysis

The good performance of this algorithm partially benefits from the sound-quality reanalysis data that are well constrained in the SGP region where ground-

based measurements are routinely assimilated to reanalysis products. Here, we analyze the uncertainties in updrafts estimation by analyzing the uncertainty for each input parameter and the error propagation.

a. Uncertainty in T_s

Evaluation of satellite-derived T_s has been difficult due to the mismatch in spatial scale of measurements between satellite sensors (a few km) and field sensors (a few m or cm), and the large spatial variability of T_s. Consequently, only a few surface types are suitable for T_s validation. The uncertainty is ±1 K at the pixel scale (Li et al. 2013b).

b. Uncertainty in T_a and V

Systematic comparison between interpolated T_a from reanalysis and ground-based measurements show RMSEs ranging from 0.95 to 4.85 K, depending on local elevation and topographical complexity (Zhao et al. 2008). Unlike T_a whose spatial distribution is continuous, wind speed is much more variable within a gridbox of reanalysis data product. Thus the spatial interpolation will produce larger errors (Figure 3.9 a and b). The RMSE for SGP cases surveyed in this study is 2.24 m/s, which is used here for uncertainty evaluation. Over oceans, the error should be smaller due to more homogeneous surfaces, which is demonstrated by Li et al. (2013a) who show a RMSE of 1.96 m/s over the Southern Ocean.

c. Uncertainty in z_i

In clear conditions, estimations of z_i are typically very uncertain by any observational instrument (Liu and Liang 2010). In the context of this study,

however, cloud-topped PBLs are of major interest. Therefore, based on the validation results in Figure 3.9c, we assign an error of 14%.

The error propagation is summarized in Figure 3.11. The biggest uncertainty comes from reanalysis data (T_a and V) that are well constrained in some regions while less constrained in others. This causes a range of uncertainties in updrafts estimation (21% to 32%). It is noteworthy that the estimated uncertainties in updrafts are solely from uncertainties in input data and do not include those induced by the theoretical model. Therefore the actual uncertainties are expected to be larger. The limitations of the theoretical models will be discussed in Section 3.4.

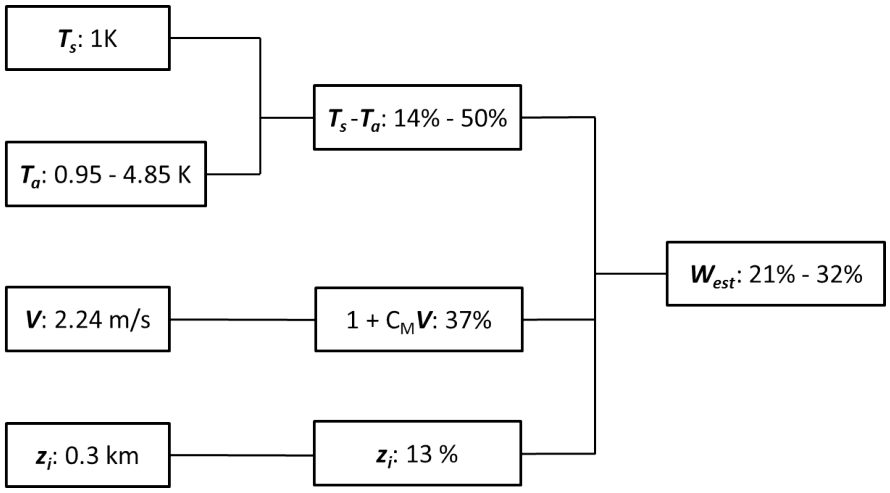

Figure 3.11: Flowchart illustrating the error propagation for W_b inference.

3.3 "Cloud-base height" method

3.3.1. Simple physics model

Williams and Stanfill (2002) reasoned that, in convective PBL topped by clouds, as the surface becomes drier, the relative humidity drops, leading to higher cloud base. In addition, smaller fraction of the solar radiation is invested in evaporation and more sensible heating is available for accelerating thermals. Hence, updrafts are stronger in PBLs topped by clouds with higher cloud bases. This argument has been used to explain the physical basis for the land-ocean contrast in global lightning activity. However, a quantitative description of the relation between cloud base height and updraft in convective PBL is still missing. In agreement with these considerations, a tight linear relationship between cloud base height and updraft speed was found in this study over both continent and ocean.

3.3.2. Examining the relation between updrafts and H_b using ARM observations

Figure 3.11a and b show the variation of lidar-measured W_{max} with H_b over the SGP site and the GOAmazon campaign, respectively. A statistically significant (R = 0.87) and tight (residual standard deviation, RSD, is 0.32 m/s) relationship is found over the SGP site. In the GOAmazon campaign, the relationship is statistically less significant (R = 0.44), which is primarily due to the small variance of H_b. The "green ocean" feature of Amazon region is characterized by very moist surface and therefore low cloud base. A *t*-test, with null hypothesis that two slopes are equal, was used for comparing the slopes of the regression lines of SGP (slope is 0.86) and GOAmazon (slope = 0.81). The value of p is 0.21 that is larger than 0.05, indicating that the

slopes of the regression lines of SGP and GOAmazon are not statistically different. Combining the two groups of datasets, we found a good correlation with R = 0.88. This observed relation between W_{max} and H_b is visually linear. Since no theory is available for a quantitative description of this relation, we assume a linear relation to capture the basic relationship for simplicity. Indeed, a large range of H_b (0.5~3 km) is captured so that the linear relationship is sufficiently robust.

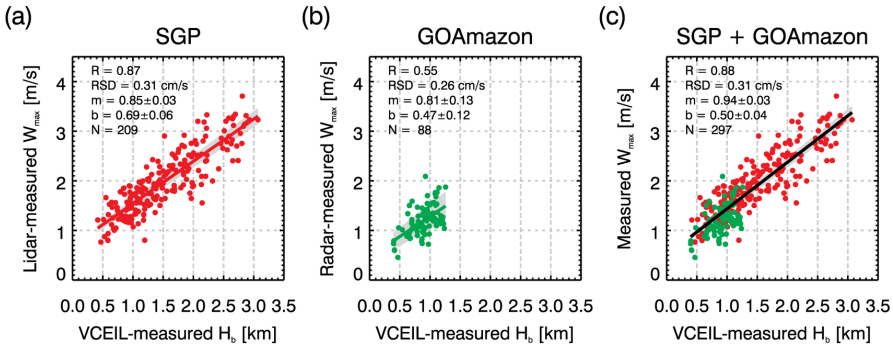

Figure 3.12: Variation of lidar-measured W_{max} with H_b measured by VCEIL at the (a) ARM SGP site, (b) GOAmazon campaign and (c) SGP + GOAmazon. MAGIC cases are not available because MWACR cannot detect aerosol particles and not able to retrieve W_{max}.

When we use the W_b to replace W_{max}, similar linear relationships are noted, despite considerate scatter, for cases of SGP, MAGIC and GOAmazon (Figure 3.12). The statistically less correlated correlation between W_b and H_b over the SGP site and the GOAmazon campaign, compared with that for W_{max} shown in Fig 3.11, are due to dilution with environmental air and ML top entrainment, processes not considered in the reasoning of positive updrafts-H_b relation hypothesized by *Williams and Stanfill* [2012], when thermals approach ML top. Again, the *t*-test shows no statistical

difference of the slopes of regression lines for the three locations and the combination of the three groups of cases indicate good correlation with R = 0.72. These statistically significant relations suggest that updrafts (W_{max} and W_b) are linearly correlated with H_b in convective PBL over both continent and ocean, and that the H_b already accounts for the differences between land and sea surfaces.

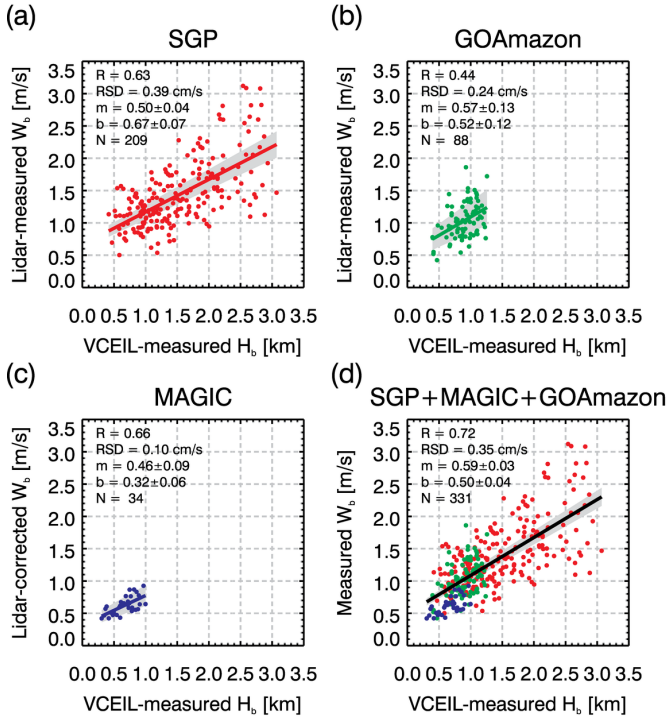

Figure 3.13: Variation of observed W_b with VCEIL-measured H_b at (a) SGP site, (b) MAGIC campaign, (c) GOAmazon campaign, and (d) SGP + MAGIC + GOAmazon. In (d), red, blue and green dots stand for SGP, MAGIC and GOAmazon, respectively.

Because Doppler lidar is not available over MAGIC, we use the WACR instead. To examine the updraft difference retrieved by lidar and Radar, we compared the W_b measured by Doppler lidar and WACR at the GOAmazon T3 site for all the suitable cases in this study, as shown in Fig. B.1. The WACR systematically overestimates the W_b because, unlike lidar whose signal is strongly attenuated by cloud, radar signal can

penetrate through the entire depth of the cloud. This means that WACR captures much more cloudy pixels well above cloud bases than DL and therefore gives larger W_b due to acceleration of parcels caused by condensational heating. We use the best-fit line forced through origin between WACR- and DL-retrieved W_b, $W_{DL} = W_{WACR}/1.48$, to grossly correct for the WACR-retrieved W_b.

3.3.3. Validation

The observed linear relations between updraft speeds and H_b provide us with an approach to remotely sense updraft speeds from space using satellite-retrieved H_b. The linear equations in Figure 2.11c and 2.12d can be used as estimation equations:

$$W_{max} = 0.94H_b + 0.49 \quad \text{[m/s]} \quad (3.9a)$$

$$W_b = 0.59H_b + 0.50 \quad \text{[m/s]} \quad (3.9b)$$

Thermodynamically speaking, when $H_b = 0$, no thermals are present to mix the PBL. In this situation, the W_b should also be zero. Equation 3.9a and 3.9b, however, show positive y-intercepts of 0.49 and 0.50 m/s, respectively. These values can be viewed as the contributions from mechanically-driven turbulence. When we force the best-fit lines through origin, these relations still keep the identical values of correlation coefficients, despite larger RSDs (Figure B.2 and B.3 in *appendix B*).

Using satellite-estimated H_b and equation 3.9a and 3.9b, we estimated the W_{max} and W_b by the satellite data only, and validated them against lidar and Radar measurements (Figure 3.13). Good agreements are found with MAPE of 19 % and 21 % for the retrieval of W_{max} and W_b, respectively.

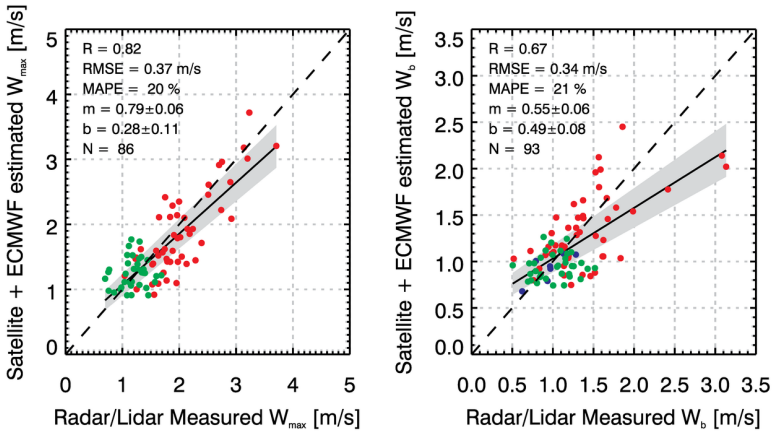

Figure 3.14: Validations of satellite-estimated W_{max} (a) and W_b (b) based on equation 3.9 against those measured by Doppler lidar and MWACR. The red, blue and green dots stand for SGP, MAGIC and GOAmazon, respectively.

3.4 Discussion

Two methods have been developed to estimate the updrafts for convective clouds using satellite and reanalysis data. The "temperature-gradient" method is based on sound theoretical basis, but its application is limited to continental convective clouds. Over oceans, the sea-air temperature difference is so small (< 1K) that the variance of sea-air temperature is insufficient for a robust relationship to be found within measurement uncertainty. On the contrary, the "cloud-base height" method is applicable to both continental and maritime clouds, but the relations between updrafts and H_b, upon which this method is based, is empirical. A sound theoretical basis is still missing. Therefore, the two methods are complementary to each other.

The W_b retrieval errors for "temperature-gradient" and "cloud-base height" methods are 24% and 21%, respectively. These accuracies are very useful for aerosol-cloud interaction studies. For example, the values of k in Towmey's analytical equation on cloud droplets activation, $N_d(w) = N_{ccn1}^{2/(k+2)} w^{3k/(2k+4)}$, typically lay in the range 0.5 to 1.0 over continents (Khvorostyanov and Curry 2006), which correspond to an error in N_d (retrieval error and natural variability) of 7 to 11% respectively, when caused by a retrieval error of 24% in W_b.

Despite the good performance in W_b retrieval, some limitations need to be noted. Firstly, the theoretical basis of this study assumes convective PBL, and all the cases selected for this study took place in the early afternoon, when turbulence in the PBL is primarily driven by buoyancy. Both of these two methods will fail in mechanically-driven PBLs. Its applicability to other phases of the diurnal cycle over land is yet to be determined. The restriction of our method to the buoyancy-driven PBL leads to another practical issue: how do we identify convective PBLs? Typically, convective cloud-topped PBLs are characterized by a dry adiabatic lapse rate below the clouds. Given the satellite-retrieved T_b and vertical profile of temperature from ECMWF reanalysis, we can derive the H_b as the height at which T_b occurs. If this H_b is consistent with the H_b derived by 2-m air temperature from a reanalysis based on the assumption of a dry adiabatic lapse rate, it means that the clouds are coupled with surface heating, indicating a convective PBL. However, this method may depend largely on the reliability of reanalysis-derived vertical profiles of temperature, which requires further study and is not the focus of this paper.

Secondly, the heterogeneities of surface properties can induce mesoscale circulations caused by different turbulent fluxes for different land surfaces (Lynn et al. 1995). Such physical processes are unaccounted for in the theoretical basis of this study, which assumes a homogeneous surface. Further study is required to examine our methods' ability to estimate updraft speeds over regions with heterogeneous surfaces.

Lastly, none of the cases selected for the present study produce precipitation. The boundaries of rain-generated cold pools tend to induce updrafts that are not directly related to the mechanism explored in this study. This will be the subject of future work.

Chapter 4 Quantifying cloud-base updraft speeds of stratocumulus from cloud-top radiative cooling

Having established approaches of W_b retrieval for convective clouds, we turn to marine stratocumulus (Sc) clouds, the dominant cloud type in terms of cloud area covered (Warren et al. 1986; Warren et al. 1988; Hahn and Warren 2007; Wood 2012). Three chapters (4~6) are devoted for Sc clouds. The present chapter introduces a method that quantifies the W_b from cloud-top radiative cooling, which lays the foundation for satellite inference of W_b. The next chapter discusses in what conditions this quantification scheme is valid, and how to identify the conditions from space. The results for the W_b retrieval and validations are presented in Chapter 6.

4.1 Introduction

Marine stratocumulus is critical to the Earth's energy budget, not only because of its broad coverage, but also its high efficiency of reflecting incoming solar radiances as low clouds. A small perturbation to marine stratocumulus cloud cover and depth is sufficient to offset the warming effect of greenhouse gases (Slingo 1990). The extensive solid cloud cover produces considerable infrared radiative cooling concentrated near cloud top, which is the dominant driving mechanism for convection under marine conditions (Lilly 1968; Moeng et al. 1996). Unlike convective clouds, which are propelled mainly by surface heating, Sc is propelled primarily by cloud top radiative cooling (CTRC). A relationship between W_b and CTRC may thus exist which can serve as a basis for a simple approach for quantifying W_b for marine stratocumulus by using combined satellite measurements

of cloud top temperature and vertical profiles of moisture above cloud tops using reanalysis data. We exploit the approach by using island and ship-based observations of a large number of marine Sc clouds across the northeastern Atlantic and Pacific Ocean.

4.2 Methodology

4.2.1. Study region

In addition to MAGIC field campaign introduced in the previous chapter, we also used the datasets from fixed-site facility of DOE/ARM on the island of Graciosa (GRW), Azores, in the northeastern Atlantic Ocean. Figure 4.1 shows the location of the MAGIC field campaign and the geography of the GRW Island. The Graciosa Island is located in the Azores Archipelago (Figure 4.1b). The ARM Mobile Facility (AMF) was deployed near the north shore of the island ((June 2009 ~ December 2010)). Although the island has a small area of ~ 60 km^2 and is assumed to provide observations with maritime behavior, the island effect should not be overlooked. Observations with southerly wind are exposed to effects by the underlying ground, and the island effect is amplified, whereas in northerly wind conditions the island effect is minimized. The effects include change in surface temperature compared to sea surface temperature, and some topography that may induce changes in updraft speed.

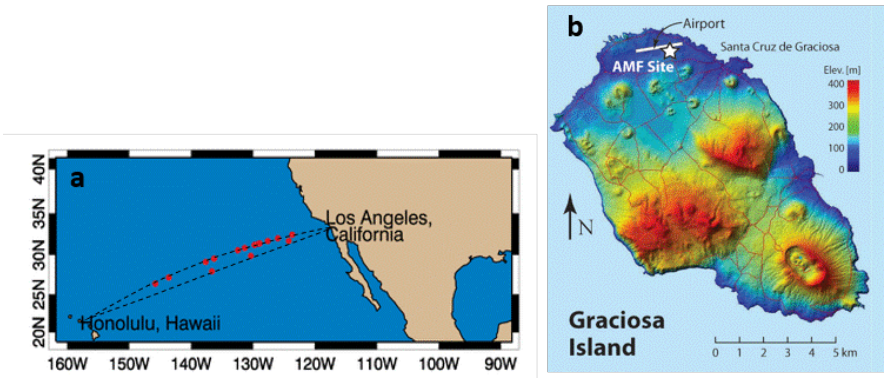

Figure 4.1: (a) Approximate track of MAGIC ship legs between California and Hawaii. The red dots mark the locations of the ship for the selected MAGIC cases. (b) Map of Graciosa Island showing the location of the AMF site, which is adapted from Wood et al. (2015). Copyright by American Geophysical Union.

4.2.2. Calculation of W_b and CTRC

Figure 4.2 presents a representative case on 11 Sep 2013 during the MAGIC campaign. Similar to the methodology in the previous chapter, W_b was computed based on WACR pixels of positive Doppler velocity during a two-hour time window and within the layer from the mean cloud-base height (H_b) to the half of cloud depth (red box in Figure 4.2b). It is noteworthy that the H_b here is associated with Sc decks. Sometimes, patches of cumulus clouds are formed below Sc clouds in particular in poorly mixed Sc-topped boundary layers (to be discussed in detail in next chapter). In such situations, only cloud bases of the overlying Sc decks are accounted for. As before, the equation (2.11), $W_b = \sum N_i w_i^2 / \sum N_i w_i$, was used to compute the W_b. To ensure high-quality, pixels with Doppler spectrum width values below 0.1 m s^{-1} and signal-to-noise ratio (SNR) values below -10 dB were removed. Here we assume that

cloud droplet have negligible terminal velocities and use the cloud droplets to trace the vertical air motion, as our main interest is in non-precipitating clouds. This assumption becomes invalid when drizzles or raindrops are present (Kollias et al. 2001). To minimize the effect of raindrops, we perform the following two quality controls. First, we removed pixels with reflectivity larger than -17 dBZ (Kogan et al. 2005). Second, we remove the entire column of radar pixels in the height-time radar plot if the distance between the VCEIL-observed cloud base and WACR-observed rain base is larger than 200 m for that specific column (Figures C.1a~e). Unlike VCEIL that is insensitive to raindrops and provides accurate cloud base heights, WACR is highly sensitive to raindrops and thus measures the bases of rain. The distance between the cloud base and rain base is considered as a measure of rain intensity. The threshold of 200 m is somewhat arbitrary but we found that the measured W_b is not sensitive to this value (Figure C.1f in *appendix C*).

The radiative transfer model used in this study is Santa Barbara DISORT Atmospheric Radiative Transfer (SBDART) model. The vertical profiles of temperature, water vapor density and ozone density are obtained from the closest radiosonde. The cloud base and top heights were determined using VCEIL and WACR respectively. The LWP was obtained from the MWR. The cloud droplet effective radius was set as the default value of 8 μm in SBDART model. This may introduce some uncertainties but sensitivity test results (Figure C.2) indicate that CTRC is not sensitive to cloud effective radius. An example of the vertical profiles of the longwave and shortwave heating rates during daytime as simulated by the SBDART are shown in Figure 4.2d. A strong longwave (LW) cooling occurs within

the upper reaches of the cloud. A cloud behaves nearly as a blackbody with respect to long-wave radiation and produces large upward blackbody flux that significantly exceeds the downward radiation originating from the above atmosphere with lower temperature and humidity. The heat losses at cloud top due to infrared radiation are partially offset by cloud-top solar heating during daytime. At the base of a cloud, the cloud is typically slightly heated when the downward flux is exceeded by the flux from below. In this study, CTRC is quantified by integrating the heating rate through the entire cloud layer. The CTRCs for all the cases analyzed in this study are tabulated in Table C.1. Each case corresponds to a two-hour segment of measurements. Assuming a BL wind speed of ~5m/s, two-hours correspond to 36 kilometers in length, which corresponds to a spatial scale of ~1000 km^2.

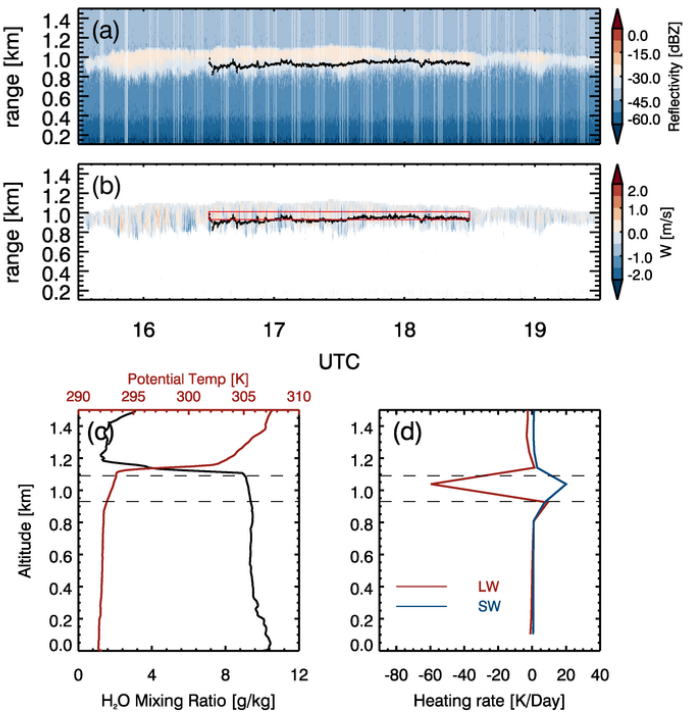

Figure 4.2: Height-time displays of WACR (a) reflectivity and (b) vertical velocity from WACR during MAGIC campaign. Black points denote the VCEIL-measured cloud base heights. The red box in (b) denotes the height-time areas for cloud base window within which pixels are selected for computing W_b. Vertical profiles of (c) potential temperature (red line) and water vapor mixing ratio (black lines) as measured by the closest radiosondes, and (d) heating rates of long-wave (red line) and short-wave (blue line) simulated by SBDART. The horizontal dashed lines mark the position of cloud base and top heights. Copyright by American Geophysical Union.

4.2.3. Case selection

Cases with non-precipitating Sc were selected. The selection criteria were as follows: (1) The stratocumulus has to be full cloudy with VCEIL-measured cloud fraction larger than 90% during the two-hour segment. (2) Typically, the Sc cloud top

is radiatively cooled so that an inversion layer is present, capping the cloud. Therefore cases with distance between cloud top and inversion layer greater than 200 meters will be excluded to assure Sc identification. (3) The clouds must not precipitate significantly. Strong precipitation, for one part, distorts the vertical velocity measurements by WACR, and for the other part may modify the thermodynamic structure that is not accounted for in radiative transfer simulations. If considerable precipitation is present, the quality control processes (removing pixels with reflectivity > -17 dBZ and distance between cloud base and rain base exceeds 200 m) will remove most radar pixels at the cloud base. Therefore cases are identified as precipitating clouds and will be excluded if the ratio of the number of remaining radar pixels with positive vertical velocity after quality controls (N_{use}) to the total number of pixels (N_{tot}) within the cloud base window (red box in Figure 4.2b) is less than 5%. (4) Only single-layer clouds were selected by WACR. A total of 53 cases in GRW and 17 cases in MAGIC were selected. There are two reasons for the small samples in MAGIC. First, four-month measurements (12 January to 9 May 2013) are missing due to the dry dock scheduled for the ship during the MAGIC campaign. Second, along transect of the ship *Spirit*, cloud regimes vary from Sc near Los Angeles to cumulus near Honolulu (Zhou et al. 2015). Sc cases can only be found in the northern part of this transect (red points in Figure 4.1a).

4.3 Results

4.3.1. W_b-CTRC relation over the MAGIC

Figure 4.3 shows the variation of WACR-measured W_b with CTRC over the MAGIC campaign. A statistically significant (R = -0.84) and tight (residual standard

deviation, RSD, is 10 cm/s) relationship is present. The result is consistent with a dominant role for CTRC in driving the updrafts by virtue of enhancing the convective instability of the marine BL. The daytime cases (red) are characterized by weaker CTRCs than nighttime ones (black) due to solar absorption offsetting part of the LW cooling at cloud tops, as revealed in Table C.1.

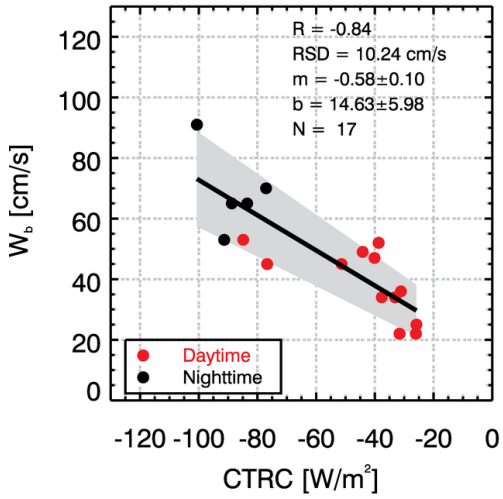

Figure 4.3: Variation of WACR-observed W_b with the cloud-top radiative cooling over MAGIC campaign. The red and black points stand for the daytime and nighttime cases, respectively.

4.3.2. The Island Effect on the GRW Island

Unlike the MAGIC field campaign where the measurements were made over open oceans, the measurements on GRW island suffer from island effect. Either surface heating or orographic uplifting may produce additional vertical velocity and disturb the relation. As shown by Figure 4.4a, W_b correlates with CTRC over the GRW site with much weaker correlation coefficient and greater scatter. As noted in

section 4.2.1, island effect in GRW is amplified when the BL winds come from the south. To elucidate the island effects, we divide the datasets into two groups based on BL wind direction: southerly BL winds (SBLWs) and northerly BL winds (NBLWs). Results in Figures 4.4b and c show that the W_b and CTRC are more strongly correlated in NBLWs condition than in SBLWs, supporting the likelihood that the sensitivity of W_b to CTRC depends greatly on the island effect. Compared with the result from MAGIC, the scatter is much greater even for the NBLWs cases. There are two possible reasons. First, the cliffs to the north of the AMF site may bring additional upward wind in NBLWs condition, which adds noise to the relationship. Second, considering the small range of the W_b (20 ~ 100 cm/s), any island disturbance will considerably affect the relation, even if such disturbance is minimized in NBLWs condition. The evidence that island surface heating increases W_b and affects the W_b-CTRC relation is presented in Figure C.3, which shows stronger W_b of GRW cases for a given CTRC than their MAGIC counterparts during daytime. This enhanced W_b on GRW during daytime with lower values of CTRC reduces the sensitivity of W_b to CTRC. The slope of best-fit linear equation decreases from 0.58 on MAGIC to 0.35 on GRW. Despite the disturbances from island effects, when we combine the datasets of GRW in NBLWs condition and MAGIC, the relationship still holds, with a correlation coefficient of -0.68 and RSD of ~13 cm/s (Figure 4.5a). Such relationship becomes more scattered when we add the removed precipitating cases (Figure C.4), suggesting that this relationship is susceptible to the effects of precipitation.

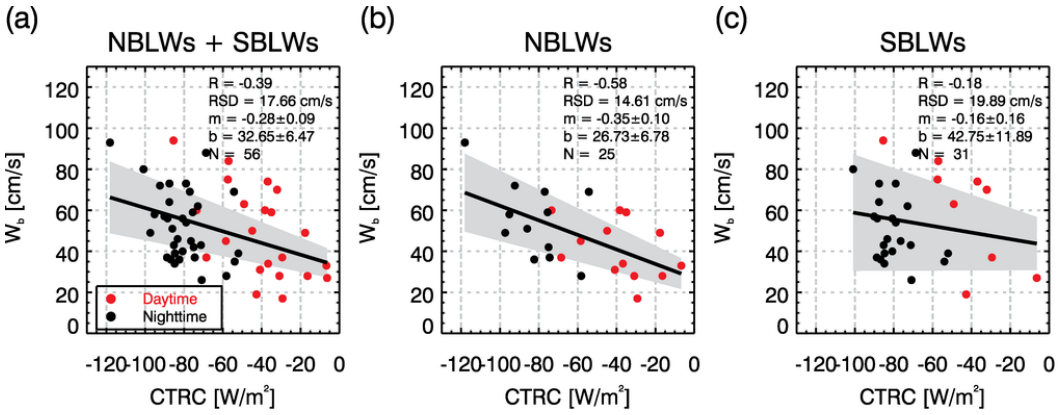

Figure 4.4: Variation of WACR-observed W_b with the cloud-top radiative cooling rate on GRW island for (a) all cases, (b) NBLWs cases, and (c) SBLWs cases. The red and black points stand for the daytime and nighttime cases, respectively.

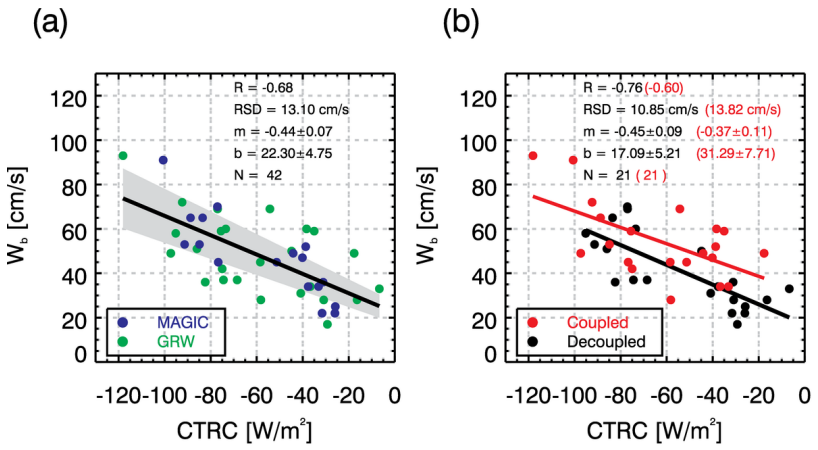

Figure 4.5: Variation of W_b with cloud top radiative cooling for MAGIC and GRW cases. The cases are color-coded based on (a) locations and (b) coupling state. In (a), the blue and green dots represent the MAGIC and GRW cases, respectively. In (b), the black and red dots/values represent the decoupled and coupled cases, respectively.

Figure 4.5b shows the CTRC-W_b relation in coupled and decoupled BLs. We use 0.15 km of difference between H_b and LCL as the threshold to discriminate between coupled and decoupled cases. In decoupled regimes, clouds are less likely to be affected by the underlying surface. Two salient features are present in Figure 4.5b. First, the updrafts for coupled cases are systematically stronger by 8 to 13 cm/s than for decoupled cases. In a coupled BL, a steady state is maintained by both the "pull" effect of CTRC and "push" effect of heat flux from surface (Wood 2012). The "push" effect produces additional energy for the convection. Second, the relation in decoupled condition is tighter than in coupled state primarily due to the reduced perturbations from surface effects. This feature is especially prominent on GRW, where the W_b-CTRC correlation for decoupled cases (R = -0.68 and RSD = 11.65 cm/s) is considerably higher than for coupled cases (R = -0.50 and RSD = 16.16 cm/s), shown in Figure C.5a.

4.3.3 CTRC: the main driver of updrafts

Figure 4.6 illustrates the means by which CTRC regulates the W_b. Stronger CTRC enhances the W_b firstly by increasing the convective instability. With stronger convective instability, the turbulent eddies are intense enough to penetrate down into the lower sub-cloud layer to couple with the surface. For one part, in a coupled BL, surface heat flux provides additional "push" to promote stronger W_b. For another, being coupled, the stratocumulus gains more moisture supply from the surface than uncoupled stratocumulus and grow in thickness. In the meantime, CTRC cools the cloud layer, thickening the clouds via reducing the moisture holding capacity of air.

Such dependence of cloud depth on CTRC is found in this study (R = -0.49 in Figure C.6). Thicker clouds provide stronger latent heating, which further accelerate air parcels. These combined effects cause stronger vertical velocities in clouds, leading to stronger cloud-top mixing. The entrainment of dry air could potentially result in considerable evaporative cooling of cloud droplets in cloud top, further enhancing the convective instability and forming a positive feedback. Of course, the entrainment will also dry the BL and prevent the cloud from growing too thick, which serves as a negative feedback to maintain a steady state for this dynamic system.

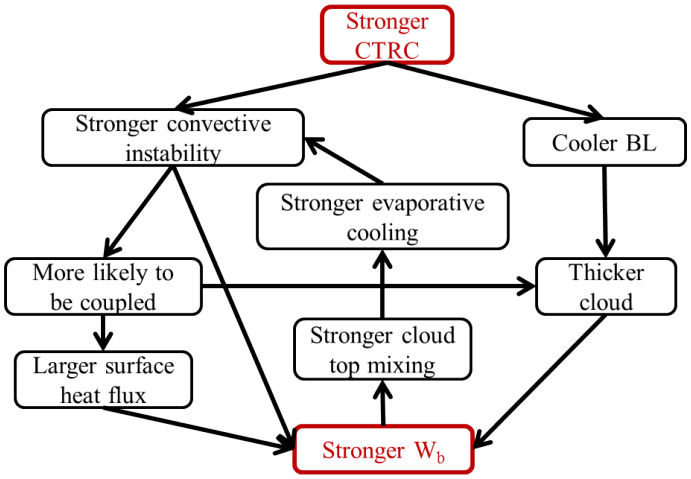

Figure 4.6: Conceptual diagram illustrating how CTRC regulates the W_b in stratocumulus clouds. This control of W_b by CTRC is one pathway of a more complicated system that involves numerous interactions and feedbacks, as noted by Wood (2012).

4.4 Conclusions

In this study, a simple relation is found between the W_b and radiative cooling at cloud top for marine Sc clouds using comprehensive ground-based observations from

the DOE/ARM over the MAGIC oceanic campaign and GRW site. The major conclusions are:

1. The relation between W_b and CTRC provides a simple means of quantifying the W_b using the formula: $W_b = m \times CTRC + b \pm 13$, in which $m = -0.44 \pm 0.07$ and $b = 22.30 \pm 4.75$ (Figure 4.5a). The units of W_b and CTRC are cm/s and W/m^2, respectively.
2. On GRW, by removing the SBLWs and coupled cases, we minimize the island effects and significantly improve the R of W_b-CTRC relation from -0.39 to -0.68. This fact, together with the statistically significant correlation (R = -0.84) over MAGIC, attests to the robustness of this relation for Sc over open oceans.
3. The W_b-CTRC relation is modulated by the coupling degree of the Sc clouds. For relatively decoupled Sc clouds (larger values of H_b - LCL), the CTRC is less efficient in driving updrafts due to reduced contributions of TKE from surface fluxes.
4. This relation can be used for satellite remote sensing of W_b. The computation of CTRC requires the atmospheric soundings and observations of cloud properties (e.g., cloud-base height, cloud-top height, cloud optical depth, and cloud droplet effective radius) as the inputs of the radiative transfer simulation. All of these inputs are available from satellite with different degrees of uncertainties. The sensitivity tests (Figure C.2) show that the CTRC is not sensitive to the cloud effective radius and cloud optical depth. Theoretically the CTRC is most sensitive to the cloud-top temperature and overlying moisture. It has been a mature practice of retrieving cloud-top temperature by satellite with reliable

accuracy. The application for satellite remote sensing will be covered in Chapter 6.

Chapter 5 Satellite inference of coupling state for marine stratocumulus clouds: to couple or not to couple?

As suggested in the preceding chapter, W_b is modulated by coupling degree of Sc clouds with surface fluxes. Therefore, to apply the W_b-CTRC relation to satellite retrieval of W_b, it is necessary to determine the coupling state of marine Sc clouds from space. Satellite determination of the coupling degree has been difficult because retrieved cloud properties represent cloud-top or column-integrated values while it is through cloud bases that Sc clouds interact with local sea surface. Our novel methodology for retrieving cloud-base properties described in Chapter 3 is not valid for Sc clouds because such clouds are typically overcast, leaving no gap for satellites to see through. Due to the above-noted inherent limitation of satellite remote sensing, studies on satellite-based estimation of the coupling degree have been scant. The most seminal study with such pursuit is Wood and Bretherton (2004)'s paper. They assume a thermodynamic structure of marine boundary layer, and estimate the coupling degree using MODIS-retrieved cloud-top temperature and liquid water path and reanalysis data. Their study, however, is flawed because of the careless way they interpret the term "coupling". They use the degree of mixing to define the coupling degree of a stratocumulus-topped boundary layer (STBL), which has been extensively adopted in meteorological literatures. Based on such definition, a STBL is *decoupled* from the sea surface when it is not well mixed. Here we argue that this conventional definition of "coupling" is inappropriate because it fails to appreciate that a STBL could be poorly mixed but strongly coupled with sea surface. A good example is

cumulus-fed Sc clouds. Such clouds are observed at the top of poorly mixed STBLs, but they often sustain full cloud cover by feeding on moisture form the sea surface that ascends through underlying cumulus clouds (Martin et al. 1995; Miller and Albrecht 1995).

The inappropriateness of the conventional "coupling" definition, which is based on a STBL's degree of mixing, motivates us to use the term "coupling" in its fundamental sense: a cloud is defined as coupled with the surface when the vapor that condenses into cloud water originates near the local sea surface. Actually these two definitions are not contradictory to each other. They differ in their defined objects: one is for boundary layers and the other is for clouds. In a coupled STBL that is well mixed, the clouds are coupled with the surface and these two definitions reach an agreement. In a decoupled poorly mixed STBL, however, coupled Cu clouds often coexist, which transport surface moisture to sustain the overlying Sc sheets against entrainment drying, forming a Cu-coupled STBL (Bretherton and Wyant 1997; Wood 2012). Such a distinction is necessary to differentiate the two fundamentally different processes associated with marine boundary clouds and marine boundary itself.

The Cu-fed Sc (or Cu-coupled STBLs) are abundant (Klein et al. 1995). Similar to well-mixed STBLs, they are often persistent with nearly 100% cloud cover and lifetime up to several tens of hours (Betts et al. 1995). Their persistence makes them climatologically important, which motivates us to examine the "coupled" nature of Cu-fed Sc with a focus on their maintenance. In this chapter, we will propose a theory and present observational evidence suggesting that the Cu-coupled STBL are basically no different from a well-mixed STBL in terms of their coupling state and

maintenance mechanism. Previous observation-based studies on Cu-fed Sc are limited either to scant number of cases (Albrecht et al. 1995; Martin et al. 1995; Miller and Albrecht 1995) or insufficient measurements due to ill-prepared instrumentations (Klein et al. 1995). The MAGIC field campaign (Lewis and Teixeira 2015; Zhou et al. 2015) deploys a series of state-of-the-art passive and active instruments with unprecedentedly long (six month) ship-borne observations of marine clouds. This allows comprehensive analysis of Cu-fed Sc. We will first put forth the mechanism of the maintenance of Cu-fed Sc in the next section. The hypothesis will be examined and quantified by the MAGIC ship-borne measurements. Finally, the ship-based findings and the theoretical hypothesis will be further tested using geostationary satellite data to help develop a novel method for inferring the coupling state of Sc from space.

5.1 Hypothesis

In a well-mixed STBL, as the dominant source of convection, the CTRC drives turbulent mixing and causes entrainment at cloud tops, which regulates surface fluxes. Increasing the CTRC induces stronger entrainment, which brings the free-tropospheric dry air into the boundary layer, reduces the surface relative humidity and elevates the LCL. This drives stronger surface latent heat fluxes to maintain moisture balance (Fig. 5.1a). At the upper limit of CTRC, surface relative humidity would reach its lowest limit that is around 55% from reanalysis data of surface relative humidity over global oceans (Wood and Bretherton 2006). This corresponds to the maximum possible LCL of ~1.1 km. After this limit has been reached, the cloud-top entrainment keeps eroding the inversion and deepening the STBL. This helps lifting

cloud bases higher than the upper limit of LCL, forming a two-layer feature: a surface-flux driven mixed layer and a CTRC-driven cloud layer (Fig. 5.1b). These two layers are decoupled by a weakly stable layer between them. In a decoupled state of STBL, without the surface moisture supply, the entrainment drying will desiccate the clouds, leading to less solid cloud layers. The thinning clouds will reduce the CTRC, which generates weaker turbulent eddies required for mixing the STBL (Fig. 5.1b). This will form a positive feedback that will eventually collapse the STBL. Very often, however, parcels associated with the newly formed Cu clouds from the moist layer near surface can overcome the weakly stable layer and reach their level of free convection. This pushes them into the existing Sc decks to supply moisture, which reconnects the Sc decks with the surface fluxes (Fig. 5.1c). As long as the clouds remain overcast, the CTRC will be the main driver of convective instability, which drives convective overturning and entrainment at Sc deck tops. Again, the entrainment will desiccate the boundary layer and enhance the surface latent heat fluxes to maintain moisture balance. This forms a new CTRC-driven system with Cu clouds serving as the conduits to couple the Sc decks with the surface (Fig. 5.1c).

The preceding discussion implies that as long as extensive Sc sheets exist, a CTRC-driven steady STBL should also exist, which couples the Sc decks with the surface, irrespective if they are in a well-mixed or Cu-coupled STBL. Otherwise the extensive Sc sheets cannot be efficiently maintained in a decoupled state of Sc. Although the overlying strong inversion can slow their dissipations, the totally decoupled Sc without Cu feedings are essentially unsteady systems and should rarely occur. The only exception is a STBL advected over colder water (Stevens et al.

1998). This phenomenon, however, is not characteristic of the subtropical Sc decks, which evolve downstream and thus move over warm water (Bretherton and Wyant 1997).

Here we examine and quantify this hypothesis, and show how it can be used for satellite inference of the coupling state of any Sc system in three forms: (1) coupled single-layer Sc, (2) decoupled single-layer Sc, and (3) Cu-fed Sc.

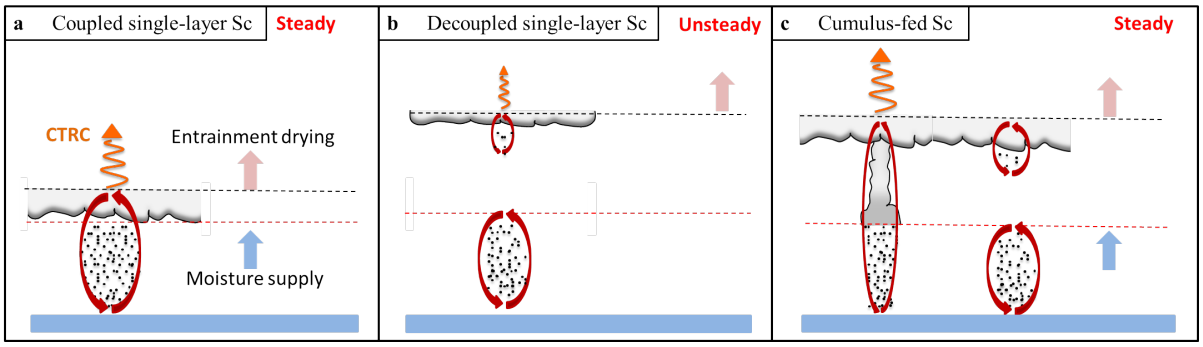

Figure 5.1: Schematic diagram illustrating the dynamics of STBLs with various coupling states. **a**, Coupled single-layer Sc. **b**, Decoupled single-layer Sc. **c**, Cu-fed Sc. The horizontal red and black dashed lines mark the LCLs and the cloud tops, respectively.

5.2 Results

5.2.1 Abundance of Cu-fed Sc clouds

A total of 98 overcast STBL cases with 1°×1° warm cloud cover larger than 90% are selected by 15th Geostationary Operational Environmental Satellite (GOES-15) during the MAGIC field campaign. Each case represents a 1°×1° satellite scene centered on the ship location. Since the ship speed is ~ 30 km/hr, we select three-hour ship measurements that covered a distance of ~ 90 km, comparable to the horizontal

size of a 1º×1º satellite scene. During each three-hour segment, we use the skewness of the ceilometer-measured cloud-base height, in combination with the Ka-band ARM Zenith Radar (KAZR), to differentiate the single-layer and Cu-fed Sc. This method is based on the fact that the probability density function (PDF) of cloud-base height for Sc decks typically follows normal distribution (Wood and Taylor 2001) and the occurrence of underlying scattered Cu clouds makes the PDF negatively skewed. This is illustrated in Fig. 5.2, which shows examples of single-layer and Cu-fed Sc from ship-based observations. The KAZR reflectivity image of single-layer Sc (Fig. 5.2a) presents coupled Sc decks with cloud bases close to LCL calculated from the temperatures measured at ~20 m above sea level (ASL). The PDF of ceilometer-measured cloud-base height (Fig. 5.2c) shows a narrow width (from ~0.7 to ~0.9 km), which has a small value of skewness (S_{CBH}). The Cu-fed Sc case, however, reveals a markedly negatively skewed PDF (S_{CBH} = -2.61; Fig. 5.2d) with a noticeable amount of cloud-base height measurements much lower than the median value. These low cloud bases, as shown in KAZR reflectivity picture of Fig. 5.2b, correspond to the scattered Cu clouds underlying the Sc decks. These Cu clouds' bases are close to LCL, indicating they are developed from moist surface layer. Some cumuli have already developed so appreciably that they penetrate into the overlying Sc decks. The penetration causes thickened clouds with more drizzling and cloud tops higher than the surroundings. Here we found a S_{CBH} threshold of -1 to be most optimal for separating the single-layer and Cu-fed Sc. This threshold value is somewhat arbitrary, but seems to differentiate between the single-layer and Cu-fed Sc according to visual examinations of their KAZR reflectivity images for all the 98 cases. A total of 37 out

of the 98 cases are classified as Cu-fed Sc. This is a considerably high frequency of occurrence, which points to the coupling between the Sc clouds and the moist surface layer for maintaining the persistence of Sc sheets.

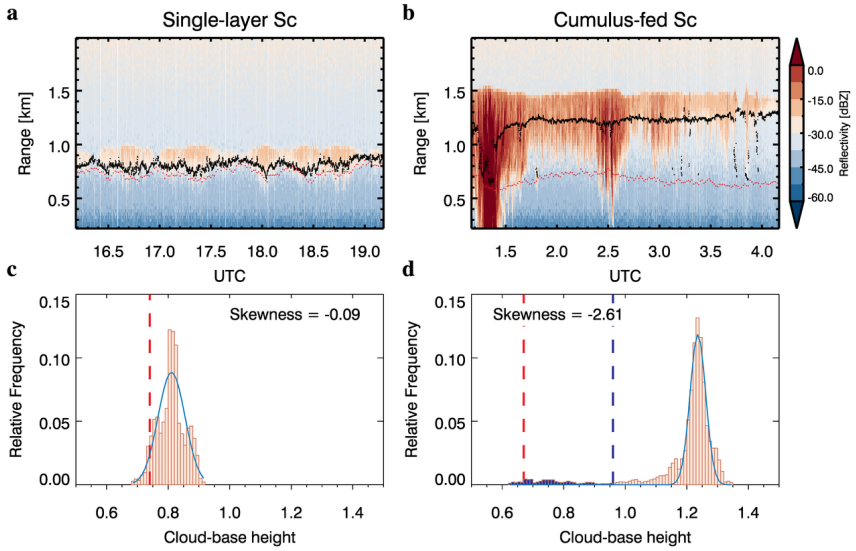

Figure 5.2: Example cases for single-layer and Cu-fed Sc. **a**,**b**, Time-height plots of KAZR reflectivity. The black and red points stand for the ceilometer-measured cloud base heights and LCLs, respectively. **c**,**d**, PDFs of ceilometer-derived cloud-base heights. The vertical red dashed lines represent the mean LCL during the three-hour segment. The light blue solid lines are the Gaussian-fit lines. In **d**, the vertical dashed blue lines mark the reference altitude (median value minus two standard deviations), below which the measurements (blue bins) are identified as "outliers". The dates for the two example cases are June 3, 2013 (**a**,**c**) and July 9, 2013 (**b**,**d**).

5.2.2. Examining the coupling limit

As predicted by our hypothesis, in any CTRC-driven regime, either well-mixed or Cu-coupled STBL, there exists a coupling limit that is constrained by CTRC. This

coupling limit is associated with the maximum possible LCL that represents the upper limit of depth that the turbulent eddies generated by CTRC can mix through. To examine the coupling limit, we use the averaged cloud-base heights of the deepest and most active cloud elements, denoted as H_b, to represent the depth, through which turbulent eddies need to mix in order to couple the clouds with the surface (see *Appendix D* for H_b calculation in detail). We use H_b – LCL as the measure of the coupling degree. A threshold of 0.2 km is used to differentiate the coupled and decoupled clouds, which is slightly higher than the 0.15 km used by Jones et al. (2011). The reason is that Jones et al. (2011) calculated the LCL from the temperatures measured at ~150 m above sea level (ASL), which is higher than the altitude of temperature measurements (~ 20 m ASL) in this study. Thus we tend to underestimate the LCL due to the fact that surface-layer air parcels are less representative of the air parcels associated with convective cloud development than mixed-layer air parcels (Craven et al. 2002).

Figure 5.3 shows the comparisons between the H_b and H_b – LCL for single-layer (Fig. 5.3a) and Cu-fed Sc (Fig. 5.3b). Each case is color-coded by the height of the capping inversion layer base (z_i) derived from radiosonde data. For single-layer Sc clouds (Fig. 5.3a), a coupling threshold of ~1.1 km is noted. If the H_b is lower than 1.1 km, the vast majority of the Sc clouds are coupled with surface with only one exception. Once the H_b reaches 1.1 km, the H_b - LCL becomes increasingly larger as the boundary layer deepens. The threshold of 1.1 km agrees with the maximum possible LCL predicted from surface relative humidity reanalysis over global oceans (Wood and Bretherton 2006).

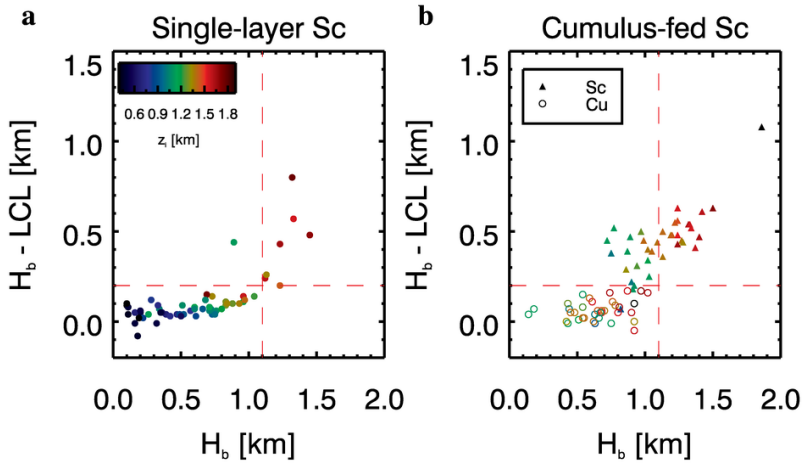

Figure 5.3: Variations of H_b - LCL with H_b. **a**, Single-layer Sc. **b**, Cu-fed Sc. The horizontal and vertical red dashed lines mark the threshold of the coupling measure of H_b - LCL and the empirically found coupling limit of H_b, respectively. Each case is color-coded by z_i.

Results for Cu-fed Sc are presented in Fig. 5.3b. Each case has two components: Cu clouds and overlying Sc decks, which are differentiated based on the PDFs of ceilometer-measured cloud-base height (see *Appendix D*). There are two noteworthy features. First, Cu components (open circles) are dominantly coupled with the surface, which reveals the "coupled" nature of Cu-fed Sc cloud system. Air parcels brought by updrafts in the Cu clouds diverge at the cloud tops and subside in the surrounding regions. This causes the surrounding Sc clouds, or Sc anvils, dominantly decoupled (solid upward triangles). Second, the coupled Cu clouds share a similar limit of ~ 1.1 km with single-layer Sc. Based on our hypothesis, both the well-mixed and Cu-coupled STBL are CTRC-driven systems. Since they share the same driving source and maintenance mechanism, they share the same coupling limit. This result

serves as observational evidence favoring our hypothesis. The conventional wisdoms originating from the theoretical framework of the popular mixed layer model (Lilly 1968; Schubert et al. 1979; Bretherton and Wyant 1997), e.g., *deepening-warming theory* (Bretherton and Wyant 1997), could predict the existence of coupling limit of H_b for well-mixed STBLs (see *Appendix E* for analysis), but fails in Cu-coupled STBLs. This is because their definition of "coupling" is based on the well-mixedness of a STBL, and once the STBL ceases to be well mixed, decoupling occurs. Such a decoupling, however, is not the real decoupling because of the Cu feedings as previously discussed. The finding here favors our definition of "coupling" that is based on the connections between the clouds and the moisture supply from the local sea surface, which offers more reasonable explanation for the shared coupling limit of H_b for Cu-coupled and well-mixed STBLs.

It is noteworthy that only 8 out of the 98 cases are totally decoupled (decoupled single-layer Sc). This is also consistent with our hypothesis which suggests that decoupled single-layer Sc clouds are essentially unstable systems due to the lack of moisture supply. The entrainment or drizzling effectively consume the cloud liquid water, thus reducing the CTRC, turbulent mixing, and, as a result, cloud lifetimes.

5.2.3. Insights from satellite and applications to satellite inferences

Although ship-based observations can provide detailed information about the coupling feature of marine Sc, they are essentially one-dimensional measurements, which sample a line of cloud parameters in a two-dimensional (2-D) cloud field. To gain 2-D insights, GOES-15 satellite data were surveyed. Figure 5.4 displays the

GOES-estimated liquid water path (LWP) for the same example cases of single-layer (Fig. 5.4a,c) and Cu-fed Sc (Fig. 5.4b,d) as those in Fig. 5.2. The "cumulus-fed" feature is clearly seen in Fig. 5.4b where patches of cloud elements have much higher values of LWP than the surroundings. In contrast, the LWP distribution for the single-layer Sc is markedly less variable. The PDFs of derived adiabatic cloud geometrical thickness (CGT_a)[2] mimics the PDFs of ceilometer-measured cloud-base height in Fig. 5.2c,d. The range of CGT_a variability for the single-layer Sc is narrow whereas the CGT_a PDF of the Cu-fed Sc is markedly skewed. A comparison between the ship-measured S_{CBH} and the opposite of the satellite-derived CGT_a skewness (S_{CGT}) shows an overall agreement (Fig. 5.5). A least-square fit suggests that a S_{CBH} threshold of -1 corresponds to -S_{CGT} of -0.45. The reason for less skewed CGT_a is that the resolution of GOES retrievals are 4 km, which is coarser than that of ceilometers. Thus, the averaged CGT_a in a 4-km pixel tends to underestimate the geometrical thickness of the most active Cu clouds with sizes smaller than 4 km, leading to less skewed PDFs. There, however, are some exceptions, in which cases satellite data identify them as Cu-fed Sc (-S_{CGT} < -0.45) whereas the corresponding S_{CBH} has smaller absolute values. This is probably attributed to the sampling limitation of ship-based measurements, which unfortunately miss the scarcely distributed Cu clouds and only capture the decoupled Sc decks. Examining the decoupled single-layer Sc identified by ship measurements (upward triangles) confirms this hypothesis as three out of the four ship-identified decoupled single-layer Sc are classified as Cu-fed Sc by GOES

[2]We derive the CGT_a by $CGT_a = (2LWP/c_w)^{1/2}$, in which c_w is a weak function of temperature and pressure (Albrecht et al. 1990) and we simply use the value of 2 g m^{-3} km^{-1} that is typical for marine warm clouds.

data. This suggests that the already scant cases of decoupled single-layer Sc (8 out of 98), identified by ship-borne measurements, stand a high chance to be decoupled Sc decks in Cu-fed Sc regimes. This further supports the conclusion that decoupled single-layer Sc with extensive fractional cloudiness rarely exist, and the commonly observed decoupled Sc clouds (Jones et al. 2011; Dong et al. 2015; Zheng et al. 2016) by either aircraft- or ship-based measurements are likely the decoupled Sc decks in Cu-fed Sc systems.

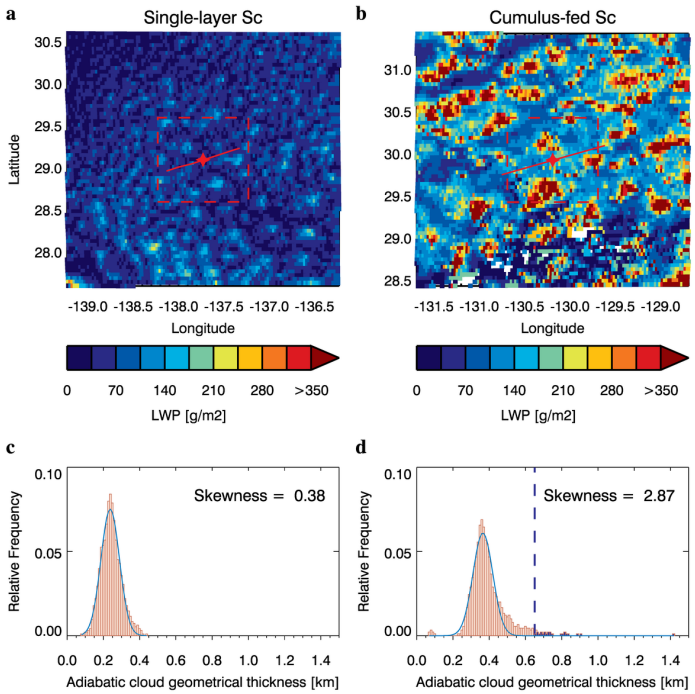

Figure 5.4: 2-D view of the GOES-15 data for the two example cases. **a**,**b**, GOES-derived LWP. The dashed rectangles mark the 1°×1° sampling regions centered on the ship locations marked by red stars. The red lines denote the ship tracks during the three-hour courses. **c**,**d**, PDFs of GOES-derived CGT_a. The two example cases are identical to that shown in Fig. 5.2.

This finding offers a satellite-based approach for inferring the coupling state of overcast Sc. A S_{CGT} threshold (in this study 0.45) could be used to differentiate the Cu-fed and single-layer Sc. The single-layer Sc is simply inferred as coupled. If defined as Cu-fed Sc, the Sc anvils, which could be identified as pixels with CGT_a less than a certain critical value (e.g., median value plus two standard deviations; the blue dashed line in Fig. 5.4d), are inferred as decoupled. The performance of this method is examined by ship-measured H_b – LCL of Sc decks, which are used to color-code each case in Fig. 5.5. The result shows that this method correctly infers the coupling state of Sc decks for 89% cases (39 out of 44) surveyed in this study. Despite the robustness of this method, e.g., sensitivity of S_{CGT} threshold to satellite sensor's spatial resolution, requires further investigations, the results are promising.

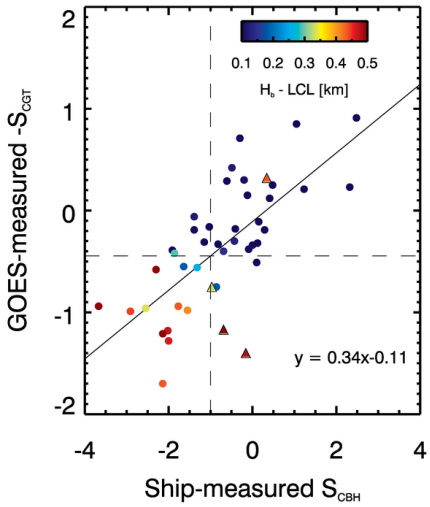

Figure 5.5: Comparison between S_{CBH} and $-S_{CGT}$. The upward triangles mark the decoupled single-layer Sc clouds identified by ship-borne measurements. Each case is color-coded by the ship-based measured H_b – LCL of Sc decks.

5.3 Conclusions

In summary, this chapter shows that coupled clouds can exist and be maintained at the top of a decoupled STBL. Such clouds are Cu-fed Sc clouds, which are maintained by CTRC in a similar way as Sc clouds in a well-mixed STBL. The cloud-top radiative cooling rate determines the amount of surface heat flux required to balance it. This, in turn, determines the surface relative humidity and the LCL of either coupled Sc or Cu underlying the Sc that is fed by the Cu. The observational support includes: (1) 38% of overcast Sc clouds are Cu-fed Sc clouds, as identified by the ship-based measurements during MAGIC field campaign. Considering the sampling limitation of ship measurements that are likely to miss the scarcely spaced Cu clouds, the percentage of Cu-fed Sc could be up to 45% as inferred from GOES-15 satellite data. (2) Extensive Sc clouds that are not fed by Cu in decoupled STBLs are very rare, indicating that the commonly observed decoupled Sc clouds are likely the Sc decks in a Cu-fed Sc system. (3) Ship-based observations reveal that the Cu-coupled and well-mixed STBL share a similar upper limit of mixed-layer depth of ~1.1 km, which are determined by the CTRC. The "coupled" nature of Cu-fed Sc, as suggested in this work, determines their extensive cloud coverage, abundance and persistence, rendering them climatologically important.

Finally, we apply the findings to develop a method for using satellite data to infer the coupling state of Sc decks, and find agreements with ship-based measurements for 89% of the cases. The advantage of satellites' near global coverage allows large-scale mappings of the marine Sc's coupling state, which could allow

more physical insights into the interactions of Sc clouds with large-scale dynamics and aerosol-Sc interactions.

Chapter 6 Satellite inference of updrafts for marine stratocumulus clouds

We are now in a position where the two ingredients required for satellite retrieval of W_b for marine Sc are available: (1) the estimation equation proposed in Chapter 4, which is W_b = -0.44×CTRC + 22.30, and (2) the capability of determining the coupling state of Sc clouds from space. To apply them to W_b retrieval, two major challenges, however, need to be addressed. First, estimations of W_b rely on the accuracy with which the CTRC is calculated. Uncertainties in satellite-retrieved quantities (e.g., cloud base and top heights) will inevitably incur additional errors in CTRC computation and thus W_b estimation. Second, precipitation may distort the W_b-CTRC relationship by generating cold pools (Zheng et al. 2016). Due to the difficulty in measuring updrafts in precipitating clouds using cloud radar, the W_b-CTRC relationship is only verified in non-precipitating STBLs and remains rather uncertain in precipitating ones. Therefore, precipitating cases have to be identified and studied with caution. Compared with a ground-borne W-band cloud radar that can offer detailed information of precipitation and, in combination with ceilometers, coupling state, satellite inferences of precipitation and coupling state are more uncertain. Therefore it is necessary to explore to what extent the added errors and misclassifications by satellite data affect the performance of W_b retrieval. This chapter concerns itself with this task.

6.1 Case selection based on satellite data

Since our objective is to perform satellite retrieval, the case selection is satellite-

based. We use GOES-15 data, not NPP/VIIRS, simply because of the scant number of cases where ship locations overlap with NPP satellite overpasses during the MAGIC field campaign. Since the Sc clouds typically have full cloud coverage with homogeneous cloud tops, the need for high spatial resolution of satellite sensors is largely alleviated. The horizontal resolution of GOES-15 cloud product[3] used in this study is 4 km. GOES-15 data were collocated with the ship track during MAGIC field campaign by sampling pixels within a 0.5°× 0.5° rectangle centering on the ship location every 30 min. The GOES-retrieved warm cloud fraction was calculated within the rectangle. Sc clouds were identified by finding collocated samples with warm cloud fraction higher than 90% for two consecutive hours. Cases without an inversion layer ($dT/dz > 0$ K/km, where T and z are temperature and altitude, respectively) below 4 km in the reanalysis temperature profile are excluded to assure the identification of stratocumulus. Cases with significant precipitation have to be removed due to their significant distortions to radar measurements of Doppler velocity, and rain-induced cold pool that drives additional updrafts (Zheng et al. 2016). Here, cases with GOES-derived $r_e > 13$ μm (Rosenfeld et al. 2012a) were identified as rainy cases and discarded. During the night without satellite measurements of r_e, we simply followed Zheng et al. (2016) who designated the rainy cases based on a WACR-based method that sets thresholds for radar reflectivity (-17 dBZ), spectral width (0.2 m/s) and length of rain streaks (200 m).

Table 6.1 summarizes the criteria and data screening for case selections. The identification of precipitation during nighttime is, however, based on ship-based

[3]The GOES-15 cloud parameter data are from National Aeronautics and Space Administration (NASA) Langley Research Center (LaRC) cloud products (http://www-angler.larc.nasa.gov).

cloud radar, not satellite, due to the missing solar near-infrared radiances at night. This should not be considered as a limitation because of minor radiative forcing of stratocumulus during nighttime when the W_b retrieval is not as necessary as that in daytime. It is noteworthy that precipitation occurs more frequently during nighttime (~3/4) than daytime (~1/2), which is consistent with the greater cloud depth and LWP at night reported in many studies (Bretherton et al. 2004; Stevens et al. 2005).

Table 6.1: Criteria for case selection.

Criteria	Percent (case number)	Day/Night
Consecutive two-hour overcast warm clouds by GOES-15	100% (305)	132/173
Above + ECMWF inversion layer check	92% (280)	122/158
Above + Precipitation check (r_e < 13 μm for daytime cases)	30% (91)	48/43
Above + functional ground-based instruments	25% (77)	36/41

6.2 Calculating CTRC using satellite and reanalysis data

As the single parameter for estimating W_b, the CTRC is of the greatest significance. GOES-derived cloud quantities used for CTRC computations are cloud top temperature (T_t), cloud visible optical depth (τ) and cloud droplet effective radius (r_e), which are retrieved by visible infrared solar infrared split-window technique (VISST) from the multispectral GOES imager data. Specifically, the theoretical basis for VISST is that the radiances of solar infrared (3.9 μm), visible (0.65 μm) and the split-window channel (10.8 μm) are primarily sensitive to changes in r_e, τ and T_t, respectively. Iterative process is employed to determine these cloud parameters by

matching the observed radiances to computed top-of-atmosphere radiances using pre-calculated look-up-tables (Minnis et al. 1995; Minnis et al. 1998). LWP was estimated as LWP = (2/3).r_e.τ. Unlike the original LaRC products (Minnis et al. 1992) that used a fixed lapse rate of 7.1 K km^{-1} between the reanalysis sea surface temperature (SST) and T_t to estimate the cloud top height (H_t), we use the parameterized lapse rate (Eq. (8) in Wood and Bretherton (2004)) to estimate the H_t. As a major revision of LaRC cloud base height (H_b) products, an adiabatic parcel model was used to calculate cloud geometrical thickness with the retrieved cloud top temperature, pressure and LWP, and the H_b is equal to H_t minus cloud geometrical thickness. During nighttime when the retrievals from visible and near infrared channels are not available, climatological mean values of τ (10) and r_e (12 μm) were used instead for calculation. The validations of the retrieved H_t and H_b against ship-based surface measurements show overall good agreements (Fig. 6.1a and b) despite an overestimated H_t is noted. The H_b retrieval based on our methodology that uses adiabatic parcel theory (black points) performs much better than the original H_b product from NASA LaRC (gray points) that is based on empirical relationships between cloud geometrical thickness and τ.

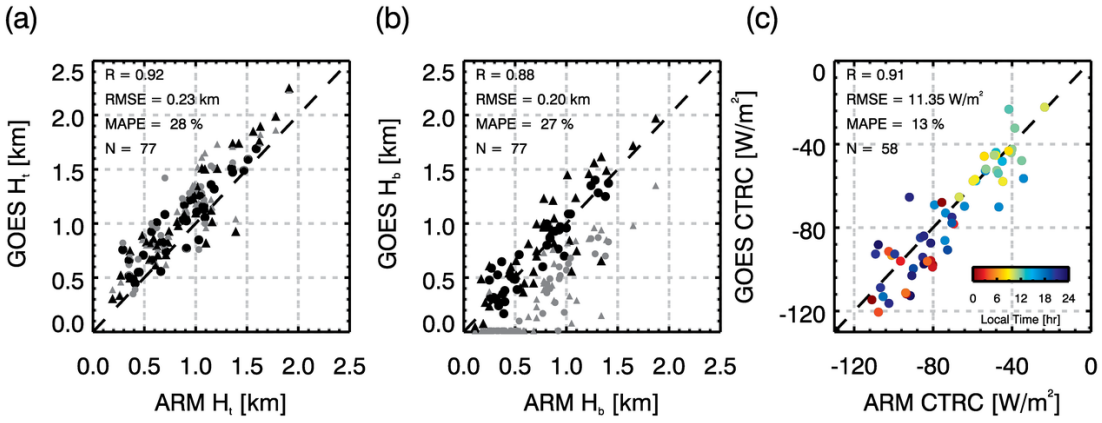

Figure 6.1: Comparisons between GOES-derived (a) H_t, (b) H_b, and (c) CTRC against ARM ground-based measurements. The H_t and H_b are two-hour averages, measured from WACR and ceilometer, respectively. Filled circles and upward triangles stand for daytime and nighttime cases, respectively. In (a) and (b), the black and grey symbols correspond to the GOES retrievals by methodology applied in this study and that from NASA LaRC products, respectively. In (c), cases are color-coded by the local time. The number of cases in (c) is limited by the availability of radiosondes used for ARM CTRC calculation. The correlation coefficient (R), root-mean-square-error (RMSE), mean-average-percentage-error (MAPE) and number of cases (N) are given.

The sounding of temperature and moisture is from ECMWF ERA-Interim reanalysis data. Due to insufficient vertical resolution, the reanalysis data typically underestimates the strength of temperature inversion and moisture contrast at top of stratocumuli, to which the CTRC is particularly sensitive. To overcome this sounding bias, we use the GOES-derived T_t as the constraint to revise the reanalysis

temperature sounding (Fig. 6.2). Assuming a relative humidity of 100%, water vapor density at cloud top can be calculated with retrieved T_t. The in-cloud temperature and moisture soundings are adjusted assuming moist adiabatic profile. The large abundance of liquid water in most stratocumulus makes them opaque to longwave radiations (Stephens 1978), thus the soundings in sub-cloud layers have negligible effect on the longwave cooling which typically concentrates within the upper few tens of meters of the cloud.

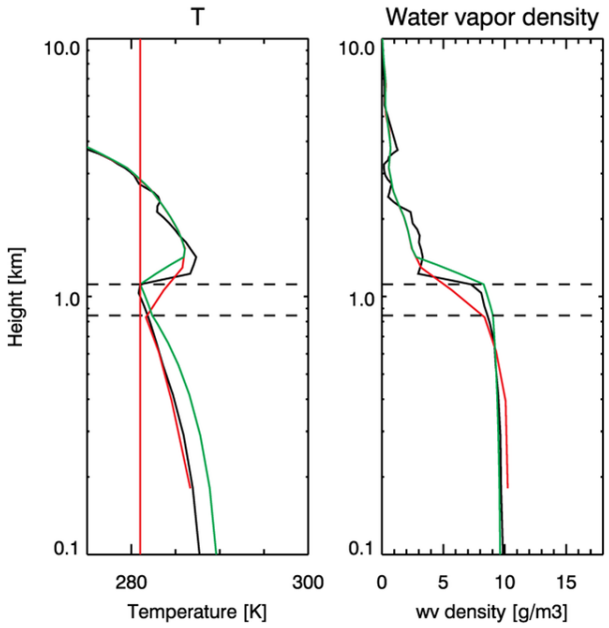

Figure 6.2: Vertical profiles of temperature (left panel) and water vapor density (right panel) from original reanalysis data (red line), revised reanalysis data (green line) and the balloon-based sounding (black line) launched in 16:45 UTC, Sep 11, 2013. The red vertical straight line in the temperature profile stands for the value of GOES-retrieved cloud-top temperature. Horizontal dashed lines in both profiles stand for GOES-derived cloud boundaries.

To evaluate the accuracy of the estimated CTRC, we use the ARM ground-based measurements (ceilometer-derived H_b, WACR-measured H_t, balloon-based soundings) as inputs for the SBDART model to calculate the "ground truth" CTRC. The τ and r_e are from the GOES-15 retrieval, to which the CTRC is insensitive (Zheng et al. 2016). The validation result (Fig. 6.1c) shows a good agreement with correlation of 0.91 and root-mean-square-error (RMSE) of 10.8 W/m^2. The feature of CTRC diurnal variation is salient with weaker CTRC during daytime (~6 to ~18 hours in local time) due to the solar absorption that partially offsets the cloud top thermal cooling.

6.3 Dependence of satellite-retrieved W_b on coupling state

Figure 6.3a shows a validation of W_b estimated using satellite-derived CTRC against WACR-derived W_b. The cases are color-coded by the difference between ceilometer-derived H_b and LCL derived from surface meteorological measurements. There is a general agreement, but the scatter is considerable. A systematic overestimation of W_b for relatively decoupled cases (bluish symbols) is noted. The systematic overestimation is not likely to be caused by biases in the estimated CTRC that exhibits no systematic dependence on the H_b – LCL (not shown). These cases with overestimated W_b are dominantly cumulus-fed Sc clouds that are identified by satellite-derived S_{CGT} and by ceilometer-derived S_{CBH} for daytime and nighttime cases, respectively. According to findings in Chapter 5, Sc decks in cumulus-fed Sc regimes are mostly decoupled from sea surfaces. The decoupling disconnects the clouds from surface heat fluxes that are important sources of buoyant TKE. Without

contributions from surface fluxes, W_b is driven by CTRC only and thus becomes weaker. Indeed, the W_b in cumulus-fed Sc regimes are systematically overestimated by 13.8 cm/s whereas there is no marked bias in estimated W_b for single-layer Sc clouds, as shown in Figure 6.3b. To correct for the decoupling-induced bias, we empirically substract 13.8 cm/s from the CTRC-estimated W_b for cumulus-fed Sc clouds. This markedly improves the performance of W_b retrieval (Fig. 6.4); R increases from 0.52 to 0.64 and MAPE decreases from 30% to 23%.

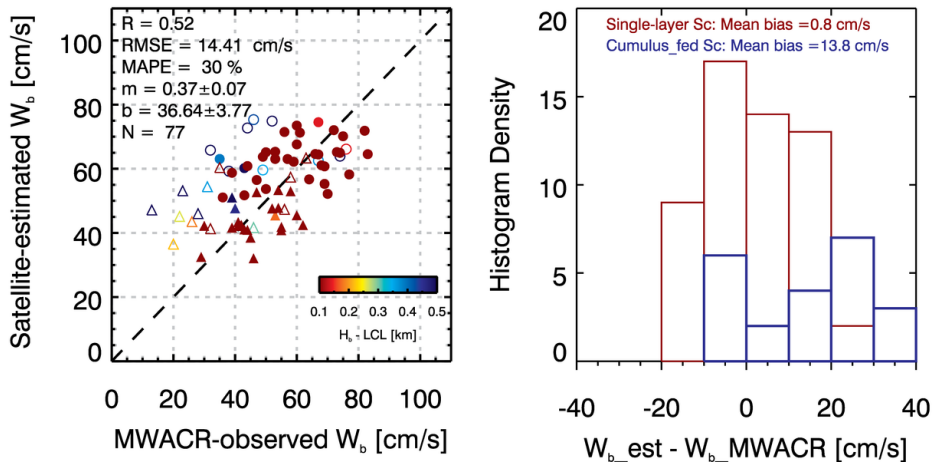

Figure 6.3: (a) Comparisons between the satellite-estimated W_b against the WACR measurements. (b) The histograms of the difference between satellite-estimated and WACR-measured W_b for single-layer (red) and cumulus-fed Sc (blue), respectively. In (a), the upward triangles and circles stand for the daytime and nighttime cases, respectively. The open and filled ones represent the cumulus-fed and single-layer Sc, respectively. Each case is color-coded by H_b – LCL.

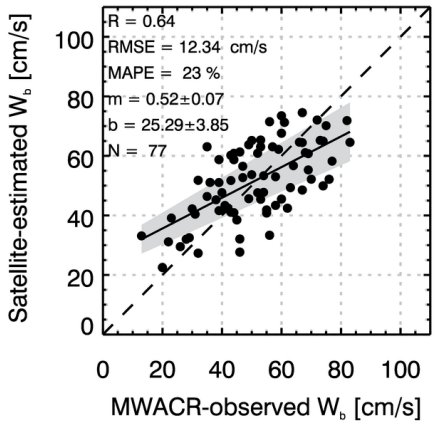

Figure 6.4: Validation of the satellite-estimated W_b against WACR-measured W_b. The CTRC-estimated W_b for the cumulus-fed Sc cases are corrected by a reduction of 13.8 cm/s to account for the effect of decoupling in weakening the W_b.

6.4 Physical mechanisms and extended application.

Here, we provide a detailed physical interpretation of how W_b is regulated by the coupling state. The interpretation is based on the hypothesis proposed in the preceding chapter (Zheng et al. 2017). According to the hypothesis, CTRC, as the dominant driving force of turbulence in a STBL, controls how deep turbulent eddies can mix through. On one hand, deep well-mixed STBLs are associated with stronger CTRC and W_b. On the other hand, as the STBL further deepens, it becomes increasingly difficult for CTRC to maintain a well-mixed boundary layer, causing decoupling that in turn weakens the W_b. To examine how these two factors compete with each other, we investigate the variation of W_b with H_b, as shown in Figure 6.5a. Each case is color-coded by CTRC. The filled and open circles represent Sc decks in single-layer and cumulus-fed Sc regimes, respectively. The size of each circle is proportional to H_b – LCL; bigger circles represent larger degree of decoupling. When

STBLs are shallow, the W_b increases with H_b. This is consistent with the role of CTRC in driving surface fluxes and thus H_b (Fig 6.5b). When the H_b reaches ~0.8 km, the systematic increase of W_b with H_b ceases. This cessation is manifested by sudden drops in W_b for some cases. Most of these cases have small values of CTRC while cases with sufficiently strong CTRC (reddish circles) still follow the W_b-H_b relation (dashed line). This could be explained using the conceptual cartoon sketched in Figure 6.5c. As the H_b increases, some Sc decks become decoupled from the sea surfaces due to an increased difficulty for CTRC to maintain a well-mixed boundary layer. This allows formations of cumulus clouds developing from moist surface layers, which serve as conduits to connect the Sc decks with surface moisture supplies. In a cumulus-coupled STBL, air parcels rise through the cumulus convection, diverge at cloud tops, and descends through the surrounding Sc decks. This renders most of the Sc decks in cumulus-fed Sc regimes decoupled from the surface, which weakens the W_b for the Sc decks. The weakening effect, however, is not present for STBLs driven by strong CTRC that generates sufficiently large TKE to well mix the boundary layers, preventing the decoupling of Sc decks. Even if in cumulus-fed Sc regimes, strong CTRC can recouple previously decoupled Sc decks to the sea surfaces and maintain the strong W_b. This explains why cases with strong CTRC, even cumulus-fed Sc ones, still fit the W_b-H_b relation after the H_b reaches 0.8 km.

When the coupling limit of 1.1 km (found in the preceding chapter) is reached, the CTRC is no longer able to maintain a well-mixed STBL no matter how strong the CTRC is (Fig. 6.5d). This leads to a dominance of cumulus-fed Sc clouds because

single-layer Sc clouds cannot be effectively maintained in a decoupled environment. The W_b for all the cases fall far below the extended best-fit line for W_b-H_b relation, regardless of CTRC strength.

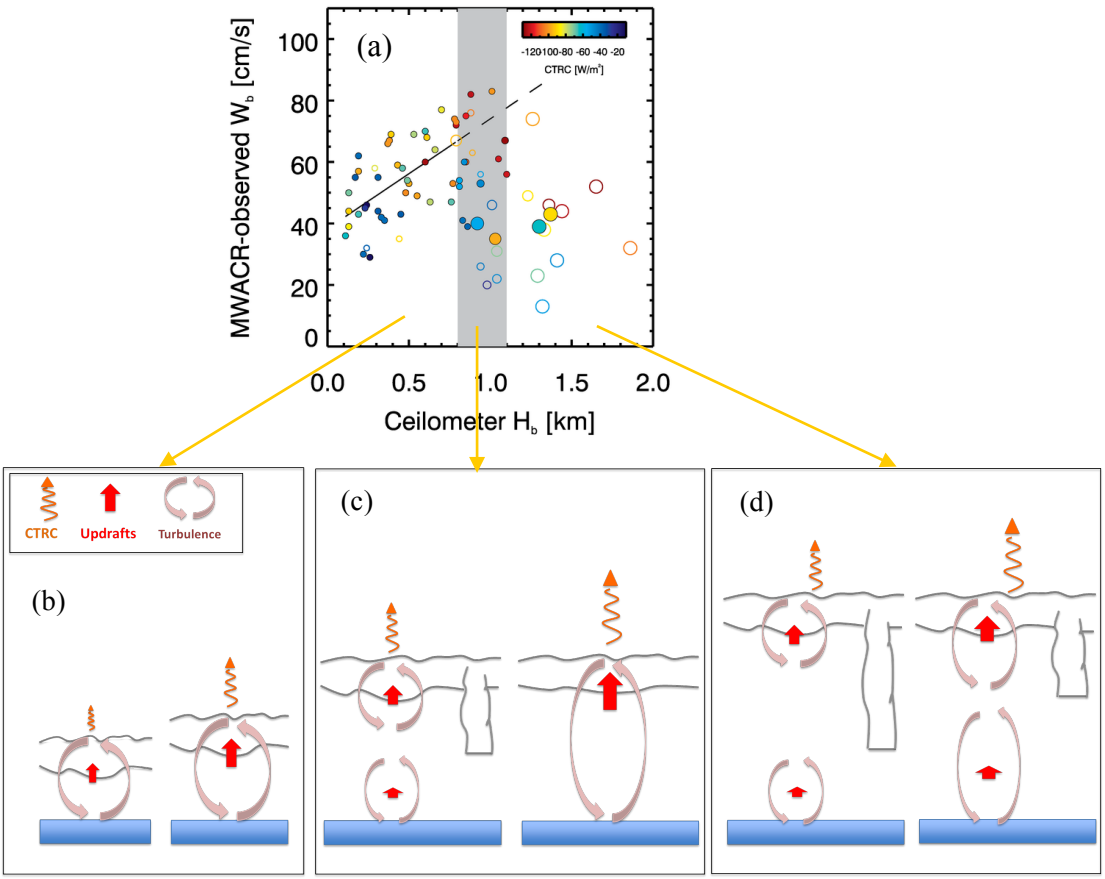

Figure 6.5: (a) Variation of W_b with H_b, and schematic illustrating the dependence of W_b-CTRC relation on H_b for (b) "coupled" phase, (c) "transition" phase, and (d) "decoupled" phase. In (a), each case is color-coded by CTRC. The filled and open circles represent the single-layer and cumulus-fed Sc clouds. The circle size is proportional to H_b – LCL. The grey region ranges from 0.8 to 1.1 km. The solid line is the best-fit line between W_b and H_b for cases with $H_b < 0.8$ km. The dashed line is the extension of the solid one.

Figure 6.6 shows a dependence of the W_b-CTRC relation on H_b. The cases are divided into three groups according to their phases in the above-described process: "coupled" phase (H_b <0.8 km), "transition" phase (0.8 < H_b <1.1 km), and "decoupled" phase (H_b > 1.1 km). The W_b is more sensitive to CTRC (larger slope of best-fit line) in "transition" phase than that in "coupled" phase. The reason is that in "transition" phase, decrease in CTRC not only causes decreased W_b, but also leads to decoupling that further weakens the W_b. In "decoupled" phase, Sc decks are dominantly decoupled, leading to weak W_b across a full spectrum of CTRC.

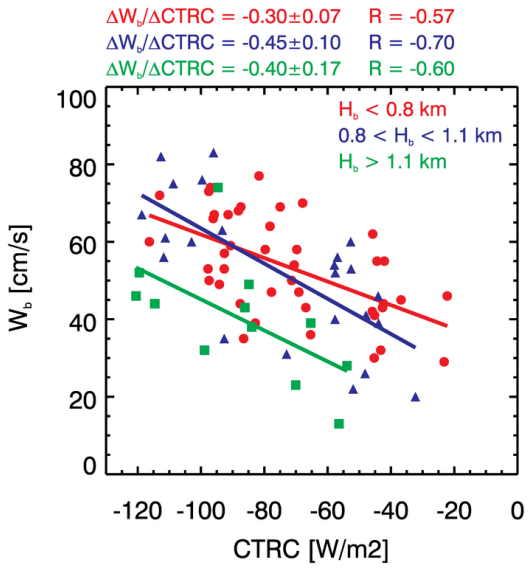

Figure 6.6: Variations of W_b with CTRC for three groups of cases: H_b < 0.8 km (red), 0.8 < H_b < 1.1 km (blue), and H_b > 1.1 km (green).

The above-described mechanism dictates the role of H_b in regulating the coupling state and the W_b. This offers a possibility of using satellite-derived H_b to

infer the coupling state of Sc clouds. The advantage of using H_b instead of S_{CGT} is that deriving H_b requires thermal channels only whereas S_{CGT} estimations need visible and near-infrared channels that are only available in daytime. Here we examine the performance of satellite-derived H_b by using the H_b threshold of 1.1 km to tease out the decoupled Sc cases whose W_b are highly dependent on the coupling state. Then we subtract 13.8 cm/s from the estimated W_b of these decoupled cases. Validation against the WACR-measured W_b shows a retrieval accuracy comparable with the skewness-based method performed in the preceding section.

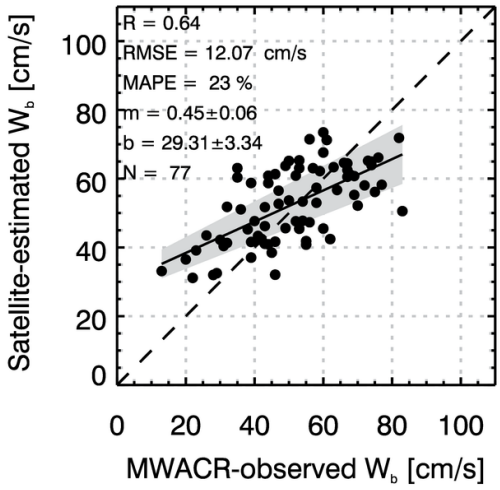

Figure 6.7: Validation of the satellite-estimated W_b against WACR-measured W_b. The CTRC-estimated W_b for cases with satellite-derived H_b > 1.1 km are corrected by a reduction of 13.8 cm to account for the effect of decoupling in weakening the W_b.

6.5 How useful is the method?

There are two limitations of this method. First of all, a correlation of 0.64 can only explain ~41% variability. However, it is worthwhile to note that the magnitude of updrafts for marine Sc is located in the lowest extreme (typically less than 1 m/s)

in the spectrum of atmospheric updrafts. The correlation coefficient of 0.64 for such a narrow range of vertical velocity (between ~0.2 and ~0.8 m/s in this study) is very encouraging given the 0.1 m/s measurement uncertainty of vertical velocity from WACR. Second, the method cannot be validated for STBL with considerable precipitation (r_e > 13 μm). Wet scavenging processes are very efficient to remove aerosols, in which situations clouds are mostly aerosol-limited and thus there is a less need for W_b retrieval.

A major advantage of this method is that all the cloud parameters required for W_b estimations are conventionally retrievable from current geostationary and polar-orbiting satellites. Among all the parameters, T_t is the most influential one. For one part, accuracies with which the H_t and H_b are derived depend on the accuracy of retrieved T_t. For another, the T_t is used to modify the specific humidity profiles from reanalysis data, to which the CTRC is sensitive. Fortunately, the T_t has long been retrieved from satellite with very satisfactory accuracy.

6.6 Summary

A method was developed to estimate W_b for marine Sc clouds from satellite along with ECMWF reanalysis data. This method is based on the dependence of the W_b on CTRC, which can be calculated by a radiative transfer model with satellite-retrieved cloud quantities and reanalysis soundings as inputs. Validation against ship-based updrafts measurements made by WACR shows a good agreement with RMSE of ~12 cm/s and MAPE of 22%. All the procedures for W_b retrieval, e.g., identification of Sc clouds, identification of precipitation, determination of coupling

states and the retrieval itself, are satellite-based. It is the first study, to our knowledge, that demonstrates the feasibility of retrieving W_b for marine Sc clouds from space.

Chapter 7 Satellite inference of cloud condensation nuclei concentrations

A successful satellite retrieval of W_b completes the last missing piece of the concept of retrieving CCN by using natural clouds as CCN chambers introduced in Chapter 1. Recalling Eq. (1.1), estimations of W_b and N_a allow for inferring the S, which together with N_a constitutes CCN(S). Next section introduces how to take advantage of high-resolution data from NPP/VIIRS to estimate the N_a.

7.1 Satellite estimation of adiabatic cloud droplet number concentration

Traditionally, cloud droplet number concentration (N_d) is inferred from passive satellite observations using the equation:

$$N_d = LWC/Mr_v, \tag{7.1}$$

where LWC and Mr_v are liquid water content and mass of a cloud drop with a mean volume radius r_v, respectively. The LWC is inferred from the satellite-derived LWP and assumes that the LWC increases linearly with altitude. The Mr_v is calculated as:

$$M_{rv} = (4/3)\rho\pi(r_e/1.08)^3, \tag{7.2}$$

where ρ and r_e are liquid water density and effective radius, respectively. An empirical relationship, $r_v = r_e/1.08$ (Freud et al. 2011), is used.

The N_d represents an average value that is affected by mixing of cloudy air with its surrounding ambient air. Therefore, N_d is smaller than N_a due to entrainments that cannot be estimated from satellite data. In non-precipitating marine layer clouds, the entrainment is typically weak and the satellite-derived N_d is close in value to N_a. For convective clouds, however, the entrainment is much stronger and the inability of

quantifying the adiabaticity from space makes the estimation of N_a much more challenging. Taking advantage of high-resolution data from the VIIRS, this challenge is overcame, allowing for the retrieval of the adiabatic LWC (LWC_a) and adiabatic r_e (r_{ea}) as described below.

7.1.1. Estimation of LWC_a

The LWC_a is dependent on the T_b and P_b. As introduced in section 2.2, T_b, defined as the warmest temperature in a convective cloud field, could be retrieved using VIIRS 375-m resolution data that can see through gaps between clouds and make visible cloud elements at different heights (Figure 2.3). Validation of the VIIRS-retrieved T_b against independently-measured T_b show a standard error of 1.1°C (Zhu et al. 2014). The good estimation of T_b allows for an accurate calculation of LWP_a using the adiabatic parcel model (Rosenfeld et al. 2016).

7.1.2. Estimation of r_{ea}

The estimation of r_{ea} is based on the assumption that mixing does not affect the value of r_e. This assumption is based on the fact that to a first-order of approximation, cloudy air mixes inhomogeneously with surrounding air (Paluch and Baumgardner 1989). Such extreme inhomogeneous mixing occurs because cloud droplets directly exposed to mixing with unsaturated air evaporate completely, thereby cool the mixed air and form downdrafts while leaving the original updraft and its cloud droplets little affected. The mixing decreases N_d and LWC, but it does not affect the value of r_e in the updraft. This process is illustrated by data from aircraft measurements shown in

Figure 7.1. The values of N_d vary substantially whereas the values of r_e do not. In this study, the satellite-derived r_e is used as a proxy for r_{ea}.

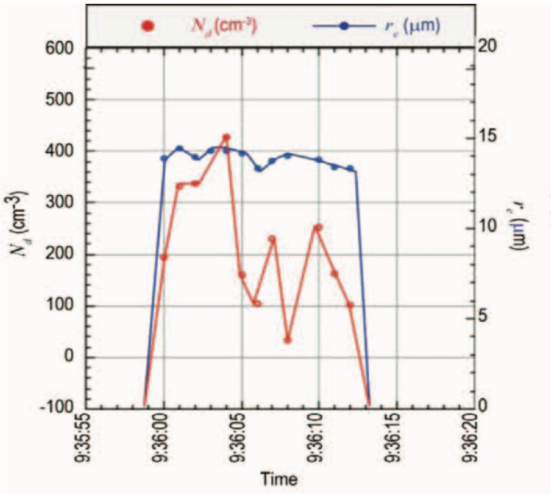

Figure 7.1: Values of N_d and r_e measured by an aircraft flying horizontally through a convective cloud at an altitude of 3.4 km. Adapted from Freud and Rosenfeld (2012).

7.2 Satellite retrieval of CCN(S)

An example for retrieving and validating CCN(S) is given here for a case on 26 July 2013 over the SGP site. Figure 7.2 presents a NPP/VIIRS high-resolution (375 m) image of the analyzed area centered on SGP site. A total of 2150 retrieved pairs of T [4]and r_e are obtained within the rectangle marked by yellow lines. The r_e values for each 1°C interval of T are sorted. The 50th percentile of r_e is plotted as a function of T, which is the commonly known "T-r_e" relations as shown in Figure 7.3.

[4] The T here is essentially cloud-top temperature retrieved in each 375-m pixel. To differentiate it from the averaged cloud-top temperature, T_t, of large-scale cloud fields used previously, we use T here.

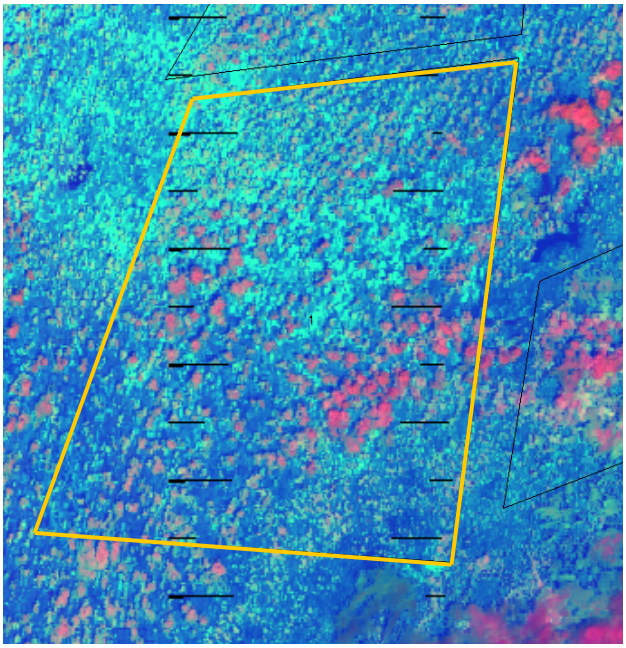

Figure 7.2: NPP/VIIRS high-resolution (375 m) image of the analyzed area (yellow rectangle) centered at the SGP site, at 26 July 2013, 19:53 UT. The rectangle size is about 45 × 45 km. The color scale is microphysical red-green-blue, where clouds with larger r_e appear redder. The red modulates the visible reflectance, green the 3.7 μm solar reflectance, and blue modulates the 10.8 μm brightness temperature, as done by Rosenfeld et al. (2014b).

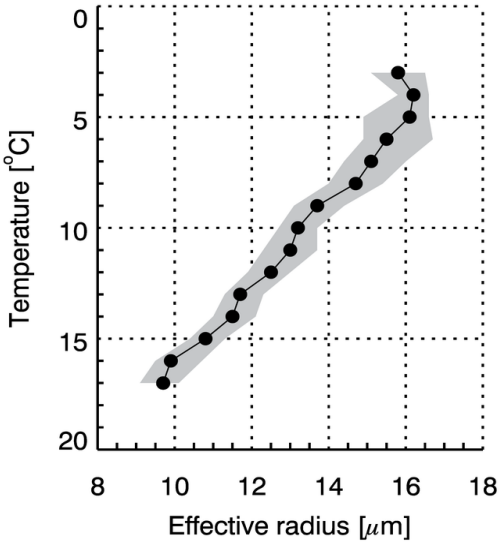

Figure 7.3: *T*-r_e relation of the convective clouds over the SGP site within the rectangle shown in Figure 7.2. The grey-shaded region denotes the 50% ± 20% percentiles of r_e.

An adiabatic cloud water profile, $LWC_a(T)$, was calculated based on the retrieved T_b and P_b. The calculation of N_a is illustrated in Figure 7.4 as the slope of the relation between the adiabatic Mr_v (Mr_{va}) and the LWC_a. In an ideal adiabatic rising cloud parcel, LWC_a should increase linearly with Mr_{va}. Therefore, a linear best-fit is calculated between LWC_a and Mr_{va}. According to equation (7.1), the slope of the best-fit line is N_a. The calculated best-fit line is forced to zero at $LWC_a = 0$. The calculated r_e for cloudy pixels that are close to cloud base (open circles) may be distorted due to surface contaminations, and are thus removed for calculation. The value of the calculated N_a is divided by 1.15 to account for the mean deviation from the assumption of extreme inhomogeneous mixing (Freud et al. 2011).

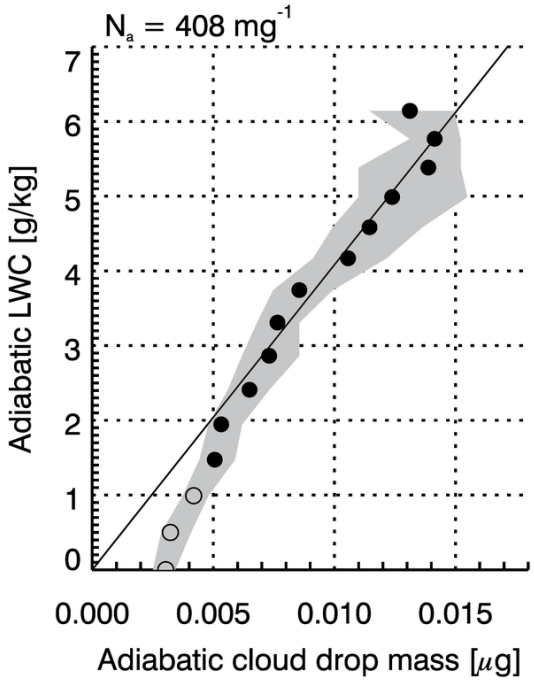

Figure 7.4: The calculation of number of activated cloud drops, N_a, based on the T-r_e relations shown in Figure 7.3. N_a is the slope of the relation between adiabatic cloud water and the mass of an adiabatic cloud drop, as shown in Equation (7.1). The grey-shaded region denotes the LWC_a calculated from 50% ± 20% percentiles of r_e. The units of LWC_a and N_a are expressed in mixing ratios, so that the changes in air density with height would not be a factor in the calculated values.

At this stage, we have satellite-retrieved W_b and N_a. Next step is validating the calculated CCN(S) against surface-based measurements made at the several ARM sites. Comparisons of surface with cloud-base measurements may be valid only if there is a well-mixed boundary layer. This was verified for the selected case studies by a vertical continuity of the radar and lidar features between the surface and cloud base and by having a radiosonde uninterrupted dry adiabatic lapse rate between the

ground and cloud base height. The cloud-base CCN(S) in units of mg^{-1} had to be converted to cm^{-3} using the surface air density for compatibility with the units of the ground-based measurements.

The retrieved and instrument-measured CCN concentration (N_{CCN}) for the same S as calculated in equation (1.1) were compared, as shown in Figure 7.5. The ground-measured CCN(S) is from a CCN diffusion chamber in the ARM Aerosol Observation System (AOS). Insufficient available time for stabilization of temperatures at low S caused the CCN readings at $S \leqslant 0.25\%$ to be grossly underestimated or zero, and therefore they could not be used. The points with $S > 0.25\%$ were fit with a second-order polynomial that was forced through the origin, because CCN must be zero for $S = 0$.

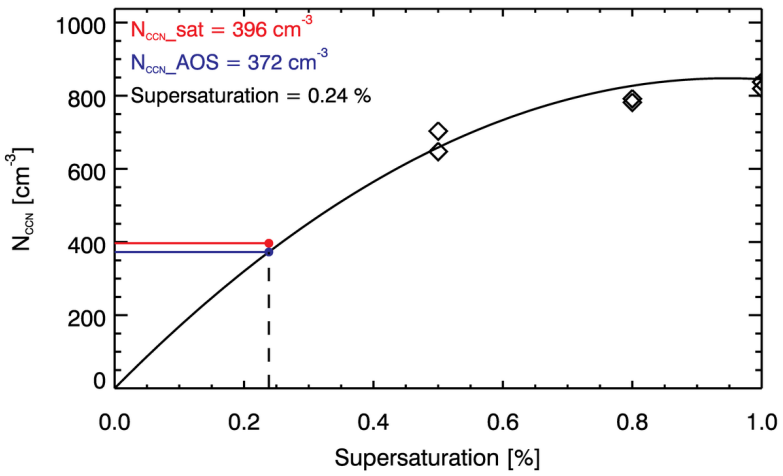

Figure 7.5: The matching between satellite-retrieved and surface-measured CCN for the case shown in the previous figures. The black open diamonds represent the measured activated aerosol number concentrations by AOS. The black line is the second-order polynomial fit line. The satellite-retrieved N_{CCN} is shown as the red horizontal line. The cloud-base supersaturation derived based on equation (1.1) is shown by the vertical dashed line. The intersection of the vertical dashed line with the polynomial fit line corresponds to the AOS-measured N_{CCN}, to which the satellite-derived N_{CCN} should be compared.

Validation cases were selected over several ARM sites at the SGP in Oklahoma, at Manacapuru near Manaus in the Amazon, and over the northeastern Pacific onboard the MAGIC ship. In addition, CCN measurements were made from the Amazon Tall Tower Observatory (ATTO) site 150 km to the northeast of Manaus. Data were obtained from the start of availability of VIIRS data in 2012 until early 2015. The case selection criteria are listed below:

(1) No obscuration from high clouds is allowed. An automatic detection of semitransparent clouds screens them from the selected area for analysis.

(2) Satellite overpass has to occur at a zenith angle between 0° and 45° to the east of the ground track, which is the sunny side of the clouds. For a specific location, these satellite views occur once or twice every six days.

(3) Convective clouds must have a vertical development that spans at least 6 K of cloud temperature from base to top. This limits the retrieval to clouds with thickness >1 km.

(4) The clouds must not precipitate significantly (i.e., without a radar or lidar detectable rain shaft that reaches the ground). The precipitation causes cold pools that disconnect the continuity of the air between the surface and the cloud base. Therefore, cloud elements with retrieved r_e > 18 μm are rejected from the analysis that is likely to rain/drizzle heavily.

The comparisons between the satellite retrievals of N_{CCN} and S at cloud base, and the ground-based measurements of N_{CCN} at the same S are shown in Figure 7.6. A large dynamic range of S for both low and high values N_{CCN} is covered in the figure. The value of $R^2 = 0.76$ means that the fit explains more than 3/4 of the variability between the satellite and ground-based measurements of CCN(S). There is a systematic underestimate bias of 14% in the satellite-retrieved CCN. It follows that the estimation errors decrease almost linearly with smaller N_{CCN}. The variation of the satellite with respect to the ground-based measurements is within 20–25% of the ground-based measurements.

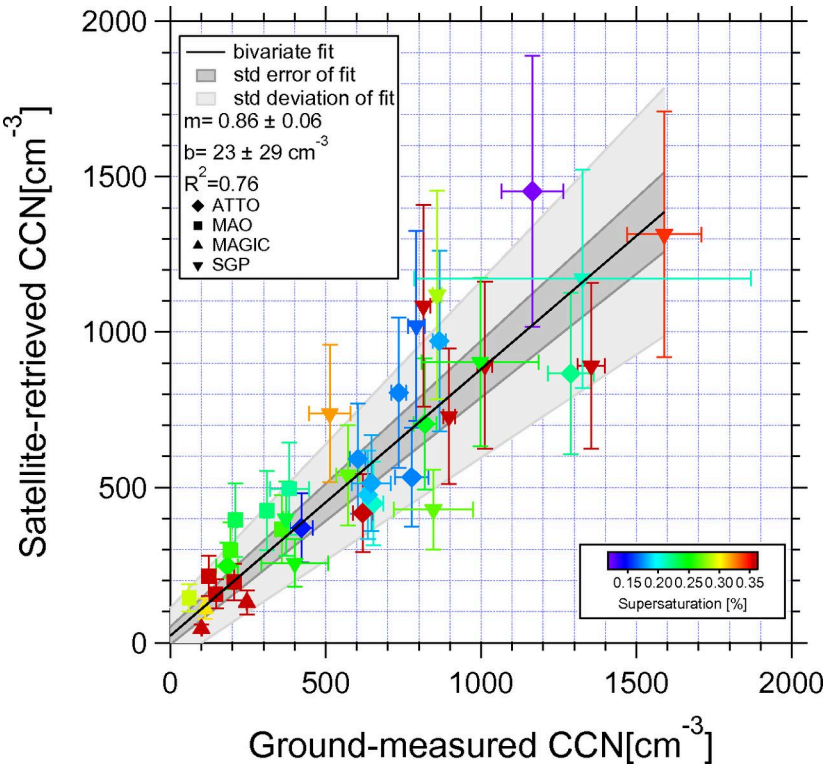

Figure 7.6: The relationship between satellite-retrieved N_{CCN} and S at cloud base, and ground-based instrument measurements of N_{CCN} at the same S. The slope and intercept of the best fit line are given in the key by m and b, respectively. The validation data are collected from the ARM sites at the SGP in Oklahoma and GOAmazon near Manaus in Brazil (MAO and ATTO), and over the northeast Pacific (MAGIC). In addition, data are obtained from the ATTO. Marker shapes denote the locations , and S is shown by the color.

7.3 Preliminary applications

The method was applied to the Houston area to gain a sanity check of the retrieved CCN(S). As an illustrative example, this procedure was applied to a regular grid of 75 × 75 VIIRS Imager pixels (28 × 28 km at nadir) over the region of Houston

during conditions of onshore flow of a tropical marine air mass. The results are displayed in Fig. 7.7. The CCN concentrations more than triple over and downwind of the urban area compared with the cross-wind areas. Meanwhile, *S* decreases over the urban area to less than half of the values over the rural areas, suggesting that CCN for the same *S* is enhanced by a factor much larger than 3. Additionally, the very low CCN concentrations over the ocean experience only a modest increase in CCN over the rural area inland. The robustness of this methodology could be dictated by the similar CCN concentrations in adjacent areas with similar conditions.

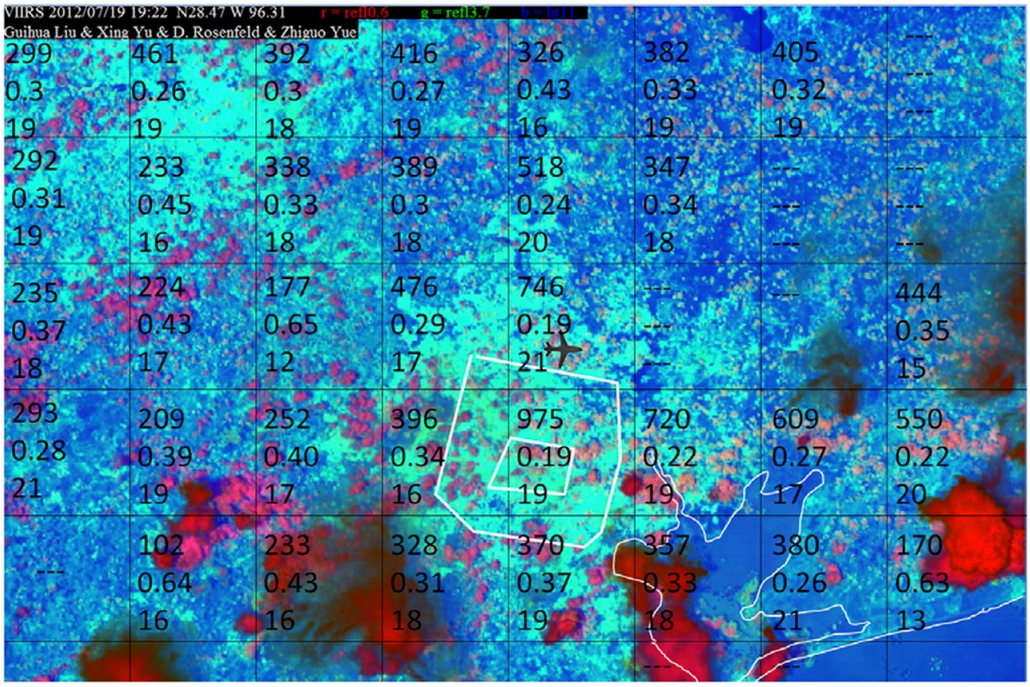

Figure 7.7: Application of the methodology to the Houston area. The retrieval is done for a regular grid of 75 × 75 375-m VIIRS/Imager pixels (~28 × 28 km at nadir). The numbers in each area are: top, N_{CCN} (cm^{-3}); middle, *S* (%); and bottom, cloud base temperature (^{o}C). Unstable clean tropical air mass flows northward (upward in the image) from the Gulf of Mexico. The Houston urban effect is clearly visible by

more than tripled CCN concentrations over Houston and the reduction of *S* to less than half. This represents an even larger factor in enhancing CCN for the same *S*. A smaller effect is seen over the urban and industrial areas to the east of Houston. The color composite is red, green, and blue for the visible reflectance, 3.7-μm solar reflectance, and thermal temperature, respectively, as in *Rosenfeld et al.* [2013].The Houston bay and beltways are marked by white lines.

Chapter 8 Limitations, future work, and ultimate goal: a key to unlocking climate forcing?

8.1 Summary

To complete the last missing piece of the novel concept of satellite retrieval of CCN(S) by using clouds as CCN chambers, a set of algorithms for inferring the W_b of warm low clouds using satellite and reanalysis data have been developed. Validations against ground-based updrafts measurements by Dopper lidar/Radar at Oklahoma, at Manaus, and onboard a ship in the northeast Pacific showed retrieval accuracy of 21% and 22% for convective clouds and stratocumulus clouds, respectively. The retrieved W_b, in combination with satellite-derived N_a, were applied to estimating CCN(S). The retrieval accuracy is 30%. Although these methods are restricted to certain conditions (to be discussed in the next section), they open a new door for constraining the uncertainties in estimates of ACI-induced climate radiative forcing.

Apart from advancement in satellite remote sensing, this dissertation contributes to the existing body of knowledge in dynamics of cloud-topped boundary layers in at least four ways:

(1) For the first time to our knowledge, robust observational evidence was found to support Williams and Stanfill (2002)'s argument that updrafts at convective cloud bases should increase with cloud-base heights. This argument has been used extensively to explain the contrast in lightening activities between continents and oceans.

(2) The dominant role of cloud-top radiative cooling in driving updrafts in stratocumulus-topped boundary layer has been known for a long time, but its quantitative description supported by comprehensive observational evidences has been lacking. This is primarily due to the difficulty in measuring both quantities (updrafts in particular) and in conducting measurements over oceans. Taking advantage of the unprecedentedly long measurements made by state-of-art instruments during the MAGIC field campaign, this dissertation provides the quantitative relationship between the cloud-top radiative cooling and updrafts.

(3) We challenge the conventional wisdom on the definition of "coupling" for marine stratocumulus-topped boundary layer, and propose new insights into the coupling of marine stratocumulus clouds with sea surfaces. Such insights are confirmed by both ship-based and satellite observations on various aspects of stratocumulus-topped boundary layers.

(4) Satellite inference of coupling state of stratocumulus clouds is a new capability. Although originally developed for updrafts retrieval, the technique itself is useful for studying the dynamics of stratocumulus-topped boundary layer from a large-scale view. This may open a new door for advancing our understanding of interactions between marine warm clouds and large-scale dynamics.

8.2 Limitations and Future work

While the general soundness of the novel approaches has been demonstrated, their limitations are considerable. Such limitations can be classified into two categories: the inherent limitations and solvable limitations. The former ones refer to the limitations inherent to satellite remote sensing or to the retrieval concepts

themselves, which are improbable (or exceedingly difficult) to be addressed in the near feature. These limitations are as follows: (1) The methods are essentially indirect approaches for inferring quantities and the compromised physics of the empirical (or semi-empirical) quantifications will always incur errors. (2) Boundary layer clouds cannot be obscured by upper layer clouds, including semitransparent cirrus. (3) The solar backscattering angles cannot be large (< 25° for CCN(S) retrieval). (4) Only non-precipitating clouds are considered.

The second category of limitations refers to the ones that could be addressed (or alleviated) if certain amounts of efforts are devoted. Most of these limitations are associated with assumptions or theoretical hypothesis that are used in algorithm development but have not been tested in a systematic way. Such limitations are quite a few. Here I just list some of them followed by actionable work to be done in the future.

Firstly, the linear relation between H_b and W_b provides an intriguingly simple approach to infer W_b from satellite data, but its theoretical basis needs more thorough investigation. The highly simplified conceptual theory of Williams and Stanfill (2003) provides a qualitative explanation to our finding of the H_b-W_b relation. To fully understand the H_b-W_b relation and its general applicability to the satellite-based estimation of W_b, a more rigorous evaluation is required and the theoretical framework needs to be established in a more quantitative way. Emphasis should be given to investigating the diurnal cycle of this relation. The observational data used in this study were collected during the NPP overpass (~13:30) when convective clouds are developing and strongly coupled with surface fluxes. How does the relationship

hold in other phases of diurnal cycle remains uncertain. Given the considerable longwave radiative forcing exerted by clouds during nighttime (Betts et al. 2013), such investigation is desirable. This will be done using a combination of theoretical derivations and large-eddy simulations.

Another assumption that needs to be examined is that Sc clouds are nearly adiabatic. This assumption is made for the estimation of N_a for Sc clouds. Although typically valid for non-precipitating Sc clouds for which our method is designed, definite observational evidence for this assumption, however, is scarce. One primary reason for the scarcity of observational evidence is the difficulty in measuring the cloud adiabaticity. Traditionally, cloud adiabaticity, f_{ad}, is calculated as $f_{ad} = LWP/LWP_a$. The LWP_a is determined by the cloud geometrical depth and T_b. The f_{ad}, however, is very sensitive to the uncertainties in cloud geometrical depth and LWP. Errors of ±20% in both cloud geometrical depth and LWP cause errors in f_{ad} of ±30% and ±20%, respectively. Such large sensitivities demand accurate measurements of cloud geometrical depth and LWP. Only ground-based observations may meet the accuracy needed. This could be done by using a combination of ceilometer, cloud radar, and microwave radiometer data to estimate H_b, H_t, and LWP, respectively. Based on the estimated f_{ad}, it is hopeful to gain a better understanding of how such an assumption can affect the CCN estimation and how we can further constrain the estimation using satellite data.

Finally, more investigations are needed before the algorithms can be applied operationally. Since the research areas of our previous investigations are limited to specific regions and cloud scenes, more rigorous and extensive validation studies are

required for better understanding the conditions of their applicability, limitations, and uncertainties, which will allow us to further improve our algorithms. The generation of operational products requires an automated system that processes the incoming streams of satellite radiance data and outputs the retrieved geophysical quantities with retrieval quality flags. Such automation system is still under development with a number of challenges such as automatic classification of cloud regimes, establishing well-established quality controls, and computational efficiency. Here, motivated by the dependence of our algorithms on cloud regimes, I try to shed some light on satellite-based approaches for automatic identification of cloud regimes. Conventional means for separating Cu and Sc clouds are based on two characteristics that differ between these two regimes: (1) Sc has extensive cloud cover while Cu clouds manifest themselves as patches of clouds with much smaller cloud coverage; (2) Sc is typically confined to a layer of little vertical development with a relatively smooth cloud top while Cu cloud tops are more variable. The former distinct is reflected in satellite retrieved warm cloud amount, and the latter one is recognizable in visible channels that provide cloud texture information. Based on these two distinctions between Cu and Sc clouds, a threshold-based cloud classification algorithm could be used. However, like any method using thresholds to differentiate two sorts of objects, this algorithm must be sensitive to threshold values when the clouds are in intermediate regimes between Cu and Sc. A typical example is the subtropical Sc-to-Cu transition. This issue may not be serious for the W_b retrieval algorithms introduced in this study. While the retrieval algorithms are different for the two cloud regimes, their fundamental retrieval principles are the same, namely,

quantifying the buoyancy energy that propels updrafts. The buoyancy energy for any boundary layer cloud is generated by two processes: surface heating and CTRC. The Cu and Sc cloud regimes represent the two extreme cases where the surface heating and CTRC play respectively dominant roles. This serves as the theoretical basis for our W_b retrieval algorithms. For clouds in an intermediate regime, both the surface heating and CTRC contribute to the production of buoyancy energy. In this case, our threshold-based classification methods will mostly likely fail. A hybrid method will thus be developed for these cases. I hypothesize that the proportion of their respective contributions is proportional to cloud cover. An increase in cloud cover enhances the role of CTRC in buoyancy energetics relative to surface heating, which shifts clouds regimes toward CTRC-driven Sc regime. So instead of providing binary yes/no answer for cloud regime identification, we could define a weighting parameter whose value ranges from 0 (Cu regime) to 1 (Sc regime) to indicate the relative dominance of the two basic cloud types in any specific satellite scene. This could be tested in future studies using ground-based data from, for example, ARM sites, among others, and model simulations.

8.3 The ultimate goal: constraining GCMs and reducing the uncertainty of climate forcing

The large uncertainties of the climate-forcing caused by aerosols have challenged us for decades. Recently, Donner et al. (2016) posit that atmospheric updrafts might be a key to unlocking climate forcing. Their argument is centered on an imbalance between significant roles of atmospheric updrafts in affecting climate forcing through influencing cloud properties and scant attentions paid on observations

and modellings of the atmospheric updrafts. Evidently, one major approach for addressing this imbalance issue is more intense observations of vertical velocity along with CCN. The development of numerical models is always accompanied with advancement in observations. Observations contribute to model improvement by serving as "constraints" broadly referred to any means that helps reduce the degrees of freedom in a numerical model. The satellite observed W_b and CCN in this study could be used to constrain GCMs in the following four ways.

1) Climate model tuning

Although the general fundamental physics of climate is well established, parameterizations, or submodels, are rather approximate. Parameterizations rely on a set of parameters, some of which are poorly constrained by observations or theory and thus are highly uncertain. Those uncertain parameters are usually tuned, sometimes in a subjective way, to improve the performance of a model. The most common tuning parameters are arguably those entering in the parameterization of clouds (Hourdin et al. 2017). Chiefly among those cloud-related tuning parameters is mixing of convective clouds with the environment, which is significantly dependent upon convective updrafts. This points to the potentials of our W_b retrievals in constraining highly uncertain parameters associated with cloud processes.

2) Empirical relationships

It has been a common practice to use satellite-derived empirical relationships to revise parameterizations of processes on the scales relevant in large-scale modeling. An example is the parameterization of the aerosol-induced reduction in cloud-droplet size toward accounting for the Twomey effect in GCMs. Such parameterization is

based on the statistical relationships of cloud-top droplet effective radius and aerosol index from satellite retrievals (Quaas and Boucher 2005). Similarly, the new retrievals of CCN and W_b could be leveraged in this way. Our CCN product should, in principle, be superior to aerosol index not only because of the advantages listed in the beginning of Chapter 1, but also because of its capability, in combination with W_b, of disentangling the effects of aerosols on clouds from meteorology.

3) Development of new parameterizations

Observations help modelers to pinpoint where further improvement is needed. For example, if parameter values in a parameterization scheme have to be adjusted to unreasonable values in order to reach a model-observation agreement, the parameterization scheme itself needs to be reformulated or even replaced with new ones. The parameterizations associated with cloud processes are particularly susceptible to such examinations given the poor representation of cloud processes in GCMs.

4) Data assimilation

Assimilation of observational data into global modeling is another approach for exploiting the usage of any new observation. It has been a great challenge to assimilating cloud quantities, especially the ones inferred from radiance data, into numerical models. But, challenges also come with possible breakthrough. If such new W_b and CCN information extracted from satellite can be effectively assimilated into climate models, it could revolutionize cloud and precipitation projections, for its uncharted territory that no one has ever tried before.

The above-listed applications, among potential others, makes our remote sensing algorithms rather promising. Although there are numerous challenges to be tackled before the methods proposed in this dissertation could be leveraged to the extent of constraining GCMs, only through confronting the biggest difficulties do we stand a chance of making real breakthroughs.

Appendices

Appendix A: A new technique of measuring updrafts in deep PBLs using Doppler lidar

An Issue concerning the difficulty for Doppler lidar in distinguishing updraft signals from noises in deep PBLs is illustrated in Figure A.1a and b, which presents the height-time image of Doppler lidar for a case on 13 July 2012. The convective cloud base height in this case is ~ 2740 m above ground level, as detected by VCEIL. Each box encloses an area with 200-m height and 2-hour width centered on NPP overpass time marked by the red vertical lines. The top box corresponds to cloud base. Figure A.1a, with a SNR threshold of 0.005, shows a clear structure of vertical velocities in the PBL. Many randomly distributed pixels in the free atmosphere, however, suggest the existence of a certain amount of noise. When we increase the SNR threshold to 0.013 (Figure A.1b), most noisy pixels are filtered out. However, the signals in the higher part of the PBL are also lost with the increasing SNR threshold.

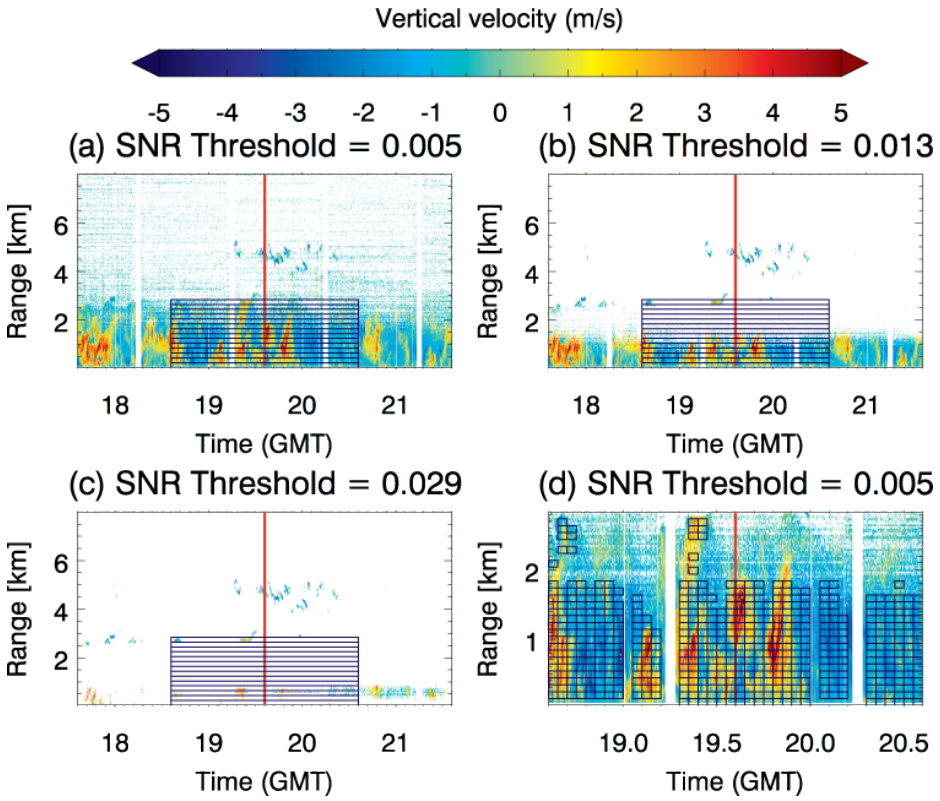

Figure A.1: Height-time display of vertical staring data from the Doppler lidar at the SGP site on 13 July 2012 with SNR threshold of (a) 0.005, (b) 0.013 and (c) 0.029. Black rectangles with 2-hour time window and 200-m height window denote the areas within which vertical velocity pixels are selected for updraft speed calculation using Eq. (6). (d) is similar to (a) but with shorter height range (up to PBL top 2740 m) and shorter time range (2 hours). Boxes in (d) stand for 'continuous' unit areas. Red lines mark the NPP overpass time for all four figures.

This new technique is based on the assumption that the distribution of atmospheric variables is locally continuous. This assumption is supported by Figure A.1a, showing that the lidar pixels within updrafts or downdrafts are continuous, whereas pixels outside thermals are comparatively discontinuous, especially in the upper part of the PBL, which has weak lidar returns. Thus, signal pixels can be distinguished from noise pixels by identifying the continuity of their distribution. Based on this principle, we selected lidar pixels according to the following procedure:

1. In the height-time display of Doppler lidar, divide the area of interest into many smaller unit areas with 100-m height and 3-min width. Each unit area contains about 450 pixels.
2. Increase the SNR threshold to a value that filters out noisy pixels but does not mar the clear structure of the PBL in the lidar image (0.005 for the case in Figure A.1). Although the determination of this SNR threshold value needs visual judgment, the calculated updraft speeds based on this algorithm are not sensitive to the SNR threshold selected in this step. The main impact of losing the signal is loss of the updraft speed altogether from the higher parts of the PBL.
3. Define as ‘continuous’ those unit areas with a ratio larger than 90% of number of remaining pixels after thresholding to the total number of pixels within the unit area (~450 pixels) (‘continuous’ unit areas for the example case are plotted in Figure A.1d).
4. All the pixels within ‘continuous’ unit areas are used to calculate updraft speeds. For pixels outside ‘continuous’ unit areas, only pixels with a SNR larger than the threshold that filters most noises (0.013 for the case in Figure A.1) are selected.

In order to test the validity of this technique, we assume that cloud base updraft is continuous through cloud base, which means that cloud base updraft speed in cloud should be consistent with the updraft speed just below the cloud base (Kollias et al. 2001). If our technique is valid, cloud based updraft speed (W_b) calculated using Eq. (2.11) with inputs from our technique should be in agreement with the in-cloud W_b that can be obtained by selecting cloudy pixels at cloud base by increasing the SNR threshold so that only cloudy pixels remain. Comparison of these two cloud base updraft speeds shows good agreement (Figure A.2) with R = 0.95. This confirms the validity of the technique herein proposed. In addition, we also find that in-cloud W_b is slightly larger than W_b, owing to the enhanced buoyancy induced by latent heat release during the condensation process. Such acceleration behavior is more significant for cases with weak updrafts. Assuming the near square-root dependence of kinetic energy on vertical velocity, the same increase in kinetic energy leads to a larger relative increase in vertical velocity for small vertical velocity.

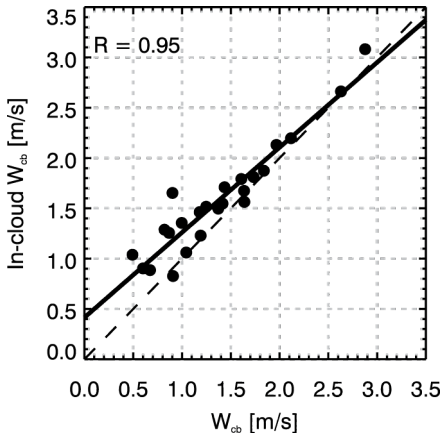

Figure A.2: Comparison between in-cloud W_b and W_b calculated using the input of vertical velocities selected according to our new technique. One data point represents a cloudy case. Solid and dashed lines are linear fit and one-to-one line, respectively. The correlation coefficient (R) is given.

Appendix B: Miscellaneous supplementary information for Chapter 3

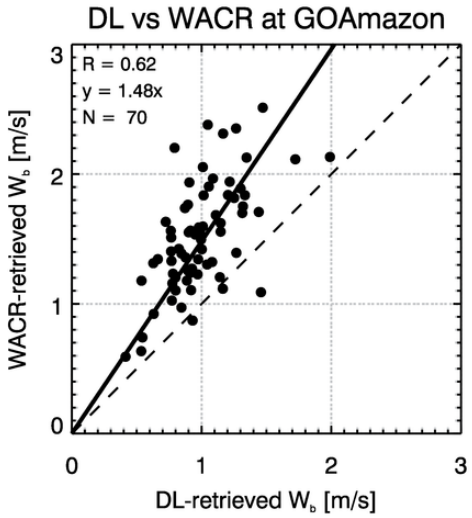

Figure B.1: Comparison between WACR- and DL-retrieved W_b during the GOAmazon campaign.

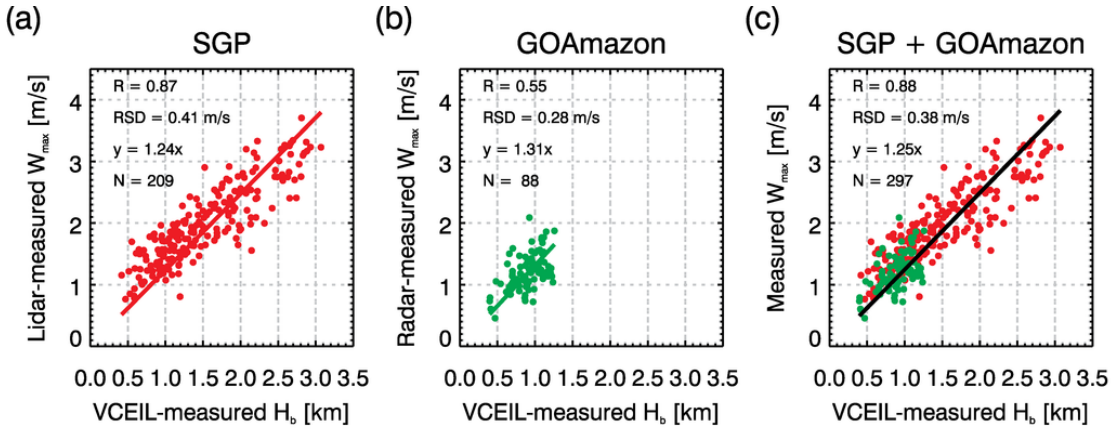

Figure B.2: Same with Fig 3.11 but forcing the best-fit line through the origin.

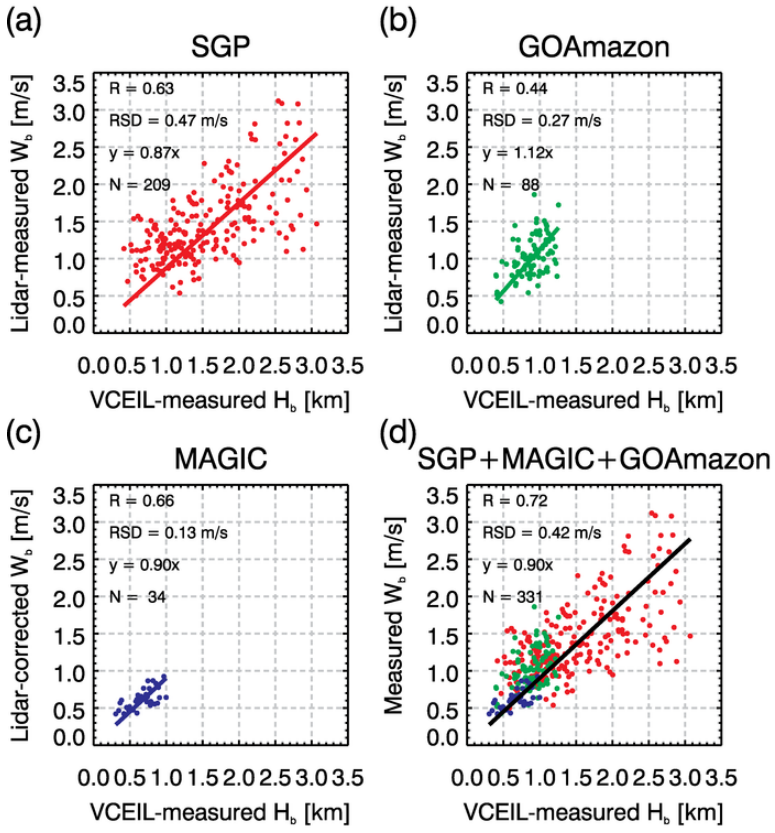

Figure B.3: Same with Figure 3.12 but forcing the best-fit line through the origin.

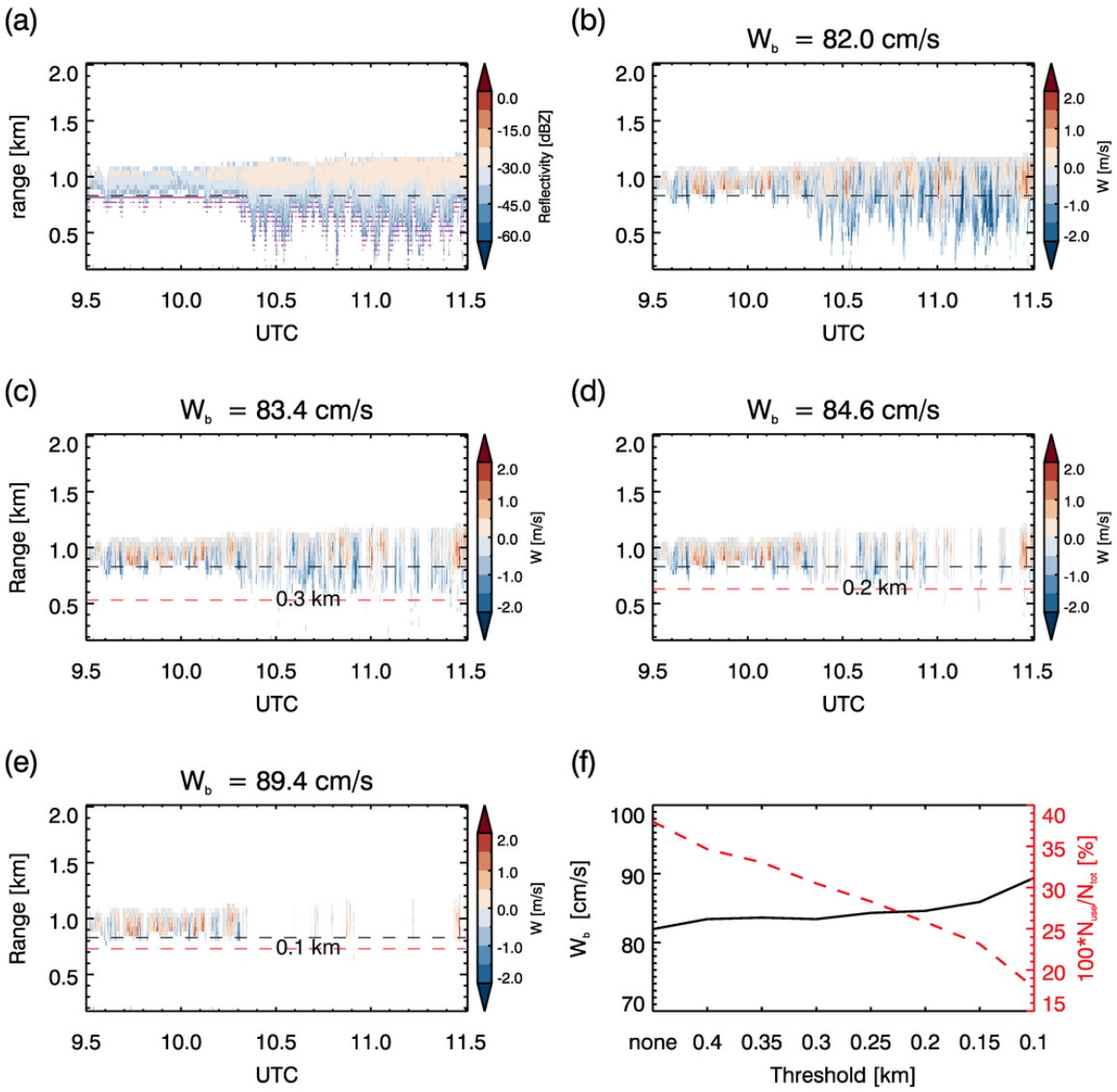

Figure C.1: Height-time displays of WACR (a) reflectivity and (b) vertical velocity for cases on 8 Nov 2010 over GRW Island. The purple dots in (a) mark the bases of rain streaks determined from radar reflectivity. The black dashed lines mark the mean cloud base height measured by VCEIL. Figures (c), (d) and (e) show the height-time displays of vertical velocity after quality controls have been applied with threshold of

the distance between cloud base and rain base of 0.3, 0.2 and 0.1 km, respectively, marked by the red dashed lines. Figure (f) show the dependences of W_b and N_{use}/N_{tot} on the threshold of distance between cloud and rain base. The variation of W_b is only 7.4 cm/s, which is within the measurement uncertainty of 10 cm/s for WACR Doppler velocity.

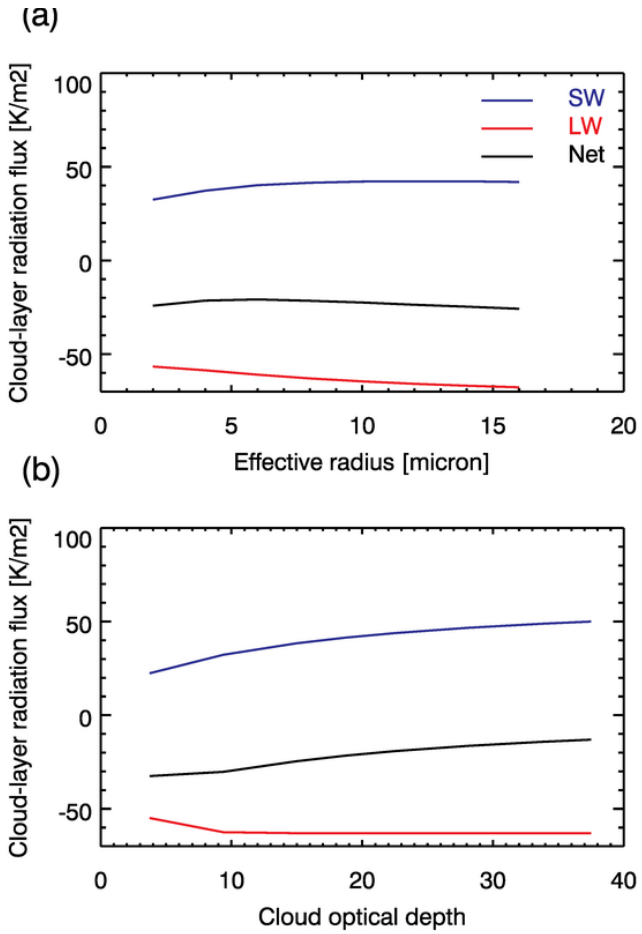

Figure C.2: Variations of cloud-top short-wave (SW), long-wave (LW) and net radiative flux with (a) cloud effective radius and (b) cloud optical depth as simulated by SBDART for the same case in Fig. 3.1.

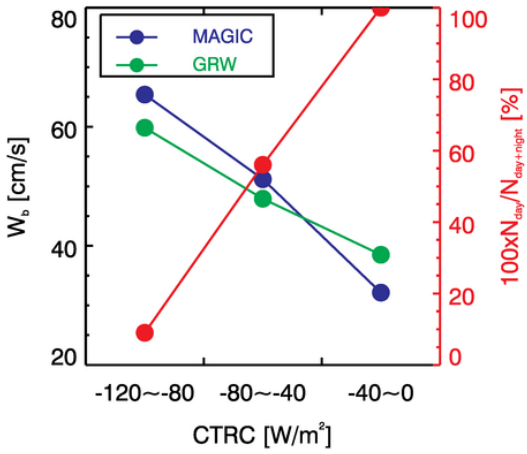

Figure C.3: Variations of W_b for MAGIC (blue dots) and GRW (green dots), and percentage of daytime cases (red dots) with CTRC. The data were grouped in 40 W/m^2 intervals of CTRC. N_{day} and $N_{day+night}$ refer to the number of daytime cases and total cases, respectively, in each bin.

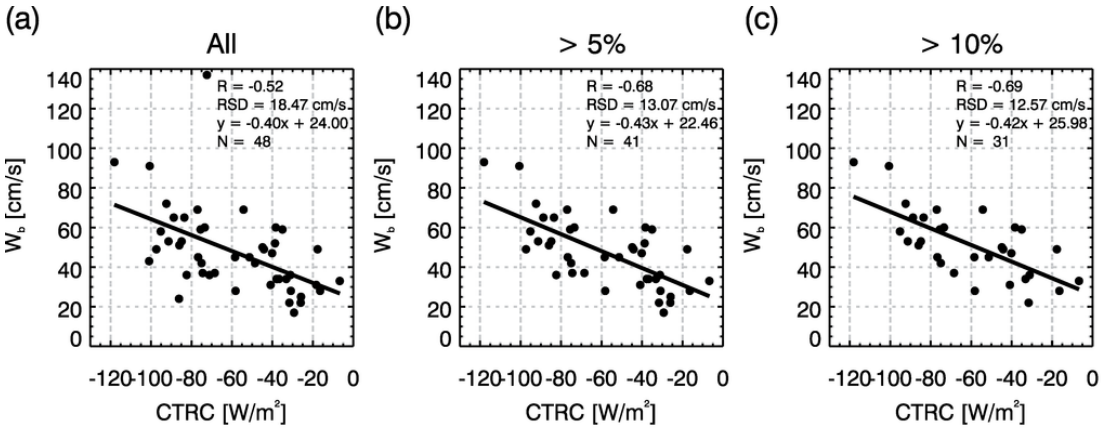

Figure C.4: Variations of W_b with CTRC over MAGIC and GRW for (a) all cases and cases with N_{use}/N_{tot} larger than (b) 5% and (c) 10%. When we increase the threshold from 5% to 10%, the relationship remains almost unchanged but the sample number drops from 41 to 31. This justifies the validity of using the threshold of 5% to minimize the effects of rain.

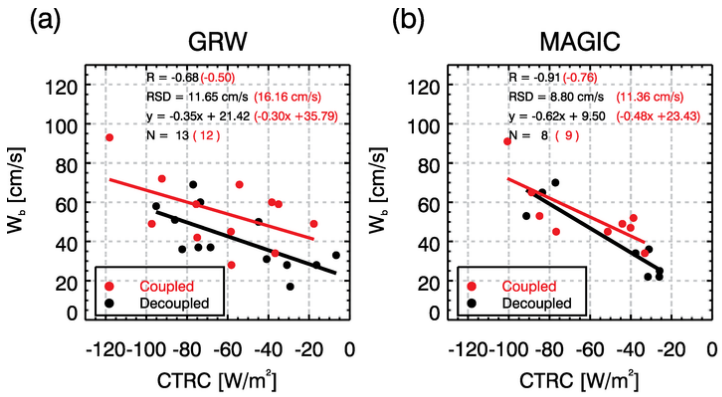

Figure C.5: Same with Figure 5.5b but for GRW (a) and MAGIC (b) cases separately.

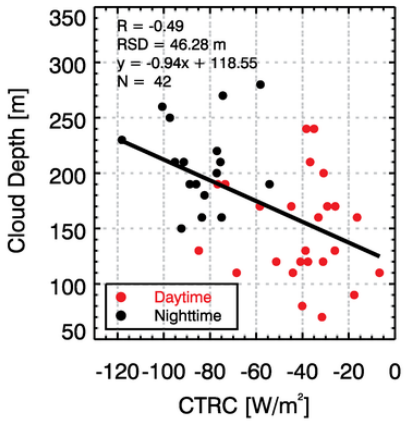

Figure C.6: Variations of cloud depth with the CTRC over MAGIC and GRW. The black and red points refer to the nighttime and daytime cases, respectively.

Table C.1: General characteristics of the cases analyzed[a]

Site	Date	Start time [GMT]	End time [GMT]	Day/Night	CTRC[b] [W/m^2]	$CTRC_{LW}$ [W/m^2]	$CTRC_{SW}$ [W/m^2]	Cloud depth [m]
GRW	20090620	1000	1200	Day	-16.39	-58.82	42.43	160
GRW	20090810	1030	1230	Day	-29.28	-79.33	50.05	170
GRW	20091102	2200	2400	Night	-118.10	-117.35	-0.75	230
GRW	20091103	0430	0630	Night	-58.20	-57.76	-0.44	280
GRW	20091122	0430	0630	Night	-97.34	-96.95	-0.39	250
GRW	20091128	1030	1230	Day	-73.45	-99.96	26.51	190
GRW	20091129	0000	0200	Night	-95.18	-94.94	-0.24	210
GRW	20091129	1030	1230	Day	-44.85	-62.79	17.94	170
GRW	20100131	1630	1830	Day	-68.48	-78.60	10.12	110
GRW	20100131	1830	2030	Night	-92.38	-92.06	-0.32	150
GRW	20100323	2130	2330	Night	-77.00	-76.73	-0.27	220
GRW	20100413	1130	1330	Day	-30.88	-98.62	67.74	200
GRW	20100430	0430	0630	Night	-75.00	-74.10	-0.90	160
GRW	20100513	0430	0630	Night	-82.37	-82.19	-0.18	180
GRW	20100610	1030	1230	Day	-17.65	-36.32	18.67	90
GRW	20100614	1030	1230	Day	-36.70	-93.30	56.60	210
GRW	20100629	0530	0730	Night	-75.50	-74.65	-0.85	210
GRW	20100629	1030	1230	Day	-35.02	-80.94	45.92	240
GRW	20100729	1030	1230	Day	-6.70	-79.59	72.89	110
GRW	20100730	0330	0530	Night	-74.45	-73.97	-0.47	270
GRW	20100731	1630	1830	Day	-40.86	-87.22	46.36	120
GRW	20100731	2200	2400	Night	-85.98	-85.36	-0.62	190
GRW	20100831	0800	1000	Day	-58.45	-66.32	7.87	170
GRW	20101003	1030	1230	Day	-38.34	-70.06	31.72	240
GRW	20101108	0000	0200	Night	-54.26	-54.11	-0.15	190
MAGIC	20121113	2200	2400	Day	-51.34	-71.58	20.24	120
MAGIC	20121202	0630	0830	Night	-77.07	-76.26	-0.81	200
MAGIC	20121212	0330	0530	Night	-100.63	-99.89	-0.74	260
MAGIC	20121224	1100	1300	Night	-83.51	-83.21	-0.30	160
MAGIC	20130603	1700	1900	Day	-38.71	-70.70	31.99	130
MAGIC	20130603	2200	2400	Day	-40.13	-73.09	32.96	80
MAGIC	20130604	1100	1300	Night	-88.75	-88.17	-0.58	190
MAGIC	20130604	1630	1830	Day	-44.17	-89.26	45.09	110
MAGIC	20130604	2200	2400	Day	-37.65	-91.04	53.39	120
MAGIC	20130717	2100	2300	Day	-31.59	-61.98	30.39	70
MAGIC	20130721	2100	2300	Day	-25.85	-95.85	70.00	170
MAGIC	20130722	1500	1700	Day	-76.70	-95.92	19.22	190
MAGIC	20130804	2200	2400	Day	-26.01	-64.54	38.53	130
MAGIC	20130825	1500	1700	Day	-84.86	-88.38	3.52	130
MAGIC	20130910	1030	1230	Night	-91.33	-91.08	-0.25	210
MAGIC	20130910	2200	2400	Day	-31.11	-91.43	60.32	120
MAGIC	20130911	1630	1830	Day	-33.13	-71.27	38.14	160

[a] Dates are shown as YYYYMMDD. Times are shown as HHMM.

[b] $CTRC = CTRC_{LW} + CTRC_{SW}$, where $CTRC_{LW}$ and $CTRC_{SW}$ stand for the longwave and shortwave component of CTRC, respectively.

Appendix D: H_b calculation for single-layer and cumulus-fed stratocumulus clouds in Chapter 5

For each single-layer Sc case, we select the lowest 10% cloud-base heights measured by ceilometer during the three-hour course and use their mean value to represent the H_b. For Cu-fed Sc clouds, H_b corresponds to the cloud base of Cu clouds. In order to extract the Cu clouds measurements, we assume that randomly distributed Cu clouds with low cloud bases are "outliers", which deviate markedly from the cloud bases of Sc decks that typically follows a normal distribution (Fig. 5.2d). Thus, we statistically select Cu clouds measurements by identifying cloud-base heights lower than the median value by two standard deviations (vertical blue dashed line in Fig. 5.2d), leaving the remained measurements to be the Sc decks. This rough classification procedure is able to separate the bulk of the measurements, but may not accurately classify the cloud elements in the transition between the Cu clouds and the Sc decks. To minimize the effect of misclassifications, for Sc decks, we simply use the median value of the classified cloud-base height measurements to represent the H_b. For Cu clouds, the lowest 10% of the extracted Cu cloud-base heights were used to calculate the H_b for excluding the artificially higher cloud bases caused by Cu tilting or possible misclassifications (Fig. 5.2b).

Appendix E: Theoretical analysis for the existence of coupling limit for well-mixed STBLs

We attempt to use *deepening-warming* mechanism (Bretherton and Wyant 1997) as a theoretical framework to interpret the existence of an upper limit of H_b for coupling in a CTRC-driven well-mixed STBL. The precipitation could be important modulators to our arguments, but we chose to neglect their effects for simplicity.

The basic argument of the *deepening-warming* theory can be summarized as follows. In a STBL, there is a large increase in buoyancy flux above cloud base due to latent heating. Such sharp increase in buoyancy flux creates an internal minimum of buoyancy flux just below the cloud base. With sufficiently strong entrainment of free-tropospheric warm air, the minimum buoyancy fluxes below the cloud base must become negative to sustain a mixed layer, which sets the stage for decoupling of the STBL. Based on this argument, Bretherton and Wyant (1997) propose a parameter to diagnose the tendency of a well-mixed STBL to be decoupled:

$$R = (A\eta \frac{\Delta z_M}{z_i}) / (\frac{\Delta F_R}{LHF}) \qquad \text{(E.1)}$$

The z_i is the inversion-layer height, Δz_M is z_i - LCL, ΔF_R is the net radiative cooling across the boundary layer, and LHF is the surface latent heat fluxes. The A and η are two coefficients for the entrainment efficiency and a thermodynamic parameter, which are set to 1.1 and 0.9, respectively (Caldwell et al. 2005; Jones et al. 2011). The decoupling occurs if R greater than a critical value R_{crit}. The term $\Delta z_M / z_i$ represents the cloud geometrical thickness, scaled by the inversion-layer height. A thicker cloud generates greater buoyancy flux in the cloud layer, which drives

stronger entrainments and thus favors decoupling. Increase in LHF can also cause larger in-cloud buoyancy fluxes and promote decoupling, which is associated with decrease in the denominator term and increase in R. All else equal, a rise in ΔF_R, dominantly contributed from CTRC, generates stronger turbulent mixing for maintaining well-mixed state, which helps to prevent the decoupling.

Here, we attempt to link the R with H_b. It is worthwhile to note that we do not intend to provide quantitative insights into the R- H_b relationships, but to use the *deepening-warming* mechanism as a theoretical framework to interpret why a critical value of H_b for decoupling could exist. In a well-mixed STBL, H_b is approximately equal to LCL, causing $z_i = H_b + \Delta z_M$. In the denominator, the $LHF = \rho_{air} L C_T V (q_s - q_M)$ (Stull 2012), where the ρ_{air} is the reference air density, L is the latent heat of vaporization for water, C_T is the transfer coefficient, V is the near surface horizontal wind speed, q_s is the water saturation mixing ratio at SST and the q_M is the mixed layer mixing ratio. The q_M is linked with H_b because the LCL is a function of q_M. Figure S1 shows the variation of calculated R with H_b at a characteristic well-mixed STBL with Δz_M of 0.25 km, SST of 294 K and V of 8 m/s. We select the ΔF_R range of 70 ~ 95 Wm^{-2}, which are typical values in subtropical Pacific oceans (Bretherton et al. 2010; Jones et al. 2011). The R increases with H_b, indicating a tendency to decoupling in a deeper STBL. For fixed H_b, R value is smallest if the ΔF_R reaches maximum, indicating that larger CTRC can support deeper well-mixed STBL. The altitude of H_b where the R value of maximum ΔF_R reaches R_{crit} is the H_b threshold for coupling. Above the H_b threshold, all the R values are greater than R_{crit} and there is no chance for STBL to be coupled even if the ΔF_R reaches its maximum.

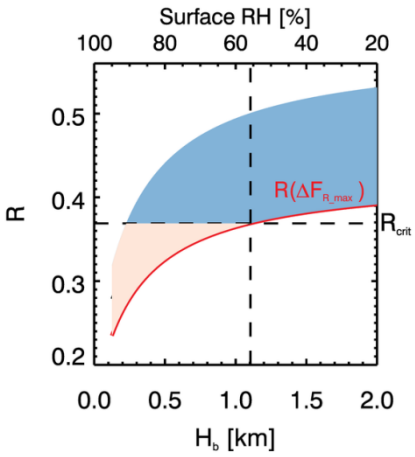

Figure E.1: Variation of the R with the H_b. The red solid line stands for the R value associated with the maximum $\Delta \boldsymbol{F_R}$. The vertical dashed line marks the empirically found coupling threshold of 1.1 km, and the horizontal dashed line marks the R_{crit}. The blue and pink shaded regions stand for the decoupled and coupled STBLs, respectively.

Bibliography

Albrecht, B. A., C. S. Bretherton, D. Johnson, W. H. Scubert, and A. S. Frisch, 1995: The atlantic stratocumulus transition experiment—astex. *B Am Meteorol Soc*, **76,** 889-904.

Albrecht, B. A., C. W. Fairall, D. W. Thomson, A. B. White, J. B. Snider, and W. H. Schubert, 1990: Surface‐based remote sensing of the observed and the adiabatic liquid water content of stratocumulus clouds. *Geophysical Research Letters*, **17,** 89-92.

Andreae, M. O., 2009: Correlation between cloud condensation nuclei concentration and aerosol optical thickness in remote and polluted regions. *Atmospheric Chemistry and Physics*, **9,** 543-556.

Apke, J. M., J. R. Mecikalski, and C. P. Jewett, 2016: Analysis of mesoscale atmospheric flows above mature deep convection using super rapid scan geostationary satellite data. *Journal of Applied Meteorology and Climatology*, **55,** 1859-1887.

Betts, A. K., C. S. Bretherton, and E. Klinker, 1995: Relation between mean boundary-layer structure and cloudiness at the r/v valdivia during astex. *Journal of the atmospheric sciences*, **52,** 2752-2762.

Betts, A. K., R. Desjardins, and D. Worth, 2013: Cloud radiative forcing of the diurnal cycle climate of the canadian prairies. *Journal of Geophysical Research: Atmospheres*, **118,** 8935-8953.

Bretherton, C., R. Wood, R. George, D. Leon, G. Allen, and X. Zheng, 2010: Southeast pacific stratocumulus clouds, precipitation and boundary layer structure sampled along 20 s during vocals-rex. *Atmospheric Chemistry and Physics*, **10,** 10639-10654.

Bretherton, C. S., and M. C. Wyant, 1997: Moisture transport, lower-tropospheric stability, and decoupling of cloud-topped boundary layers. *Journal of the atmospheric sciences*, **54,** 148-167.

Bretherton, C. S., and Coauthors, 2004: The epic 2001 stratocumulus study. *B Am Meteorol Soc*, **85,** 967-977.

Businger, J. A., 1973: A note on free convection. *Boundary-Layer Meteorol*, **4,** 323-326.

Caldwell, P., C. S. Bretherton, and R. Wood, 2005: Mixed-layer budget analysis of the diurnal cycle of entrainment in southeast pacific stratocumulus. *Journal of the atmospheric sciences*, **62,** 3775-3791.

Carslaw, K., and Coauthors, 2013: Large contribution of natural aerosols to uncertainty in indirect forcing. *Nature*, **503,** 67-71.

Chandra, A. S., P. Kollias, S. E. Giangrande, and S. A. Klein, 2010: Long-term observations of the convective boundary layer using insect radar returns at the sgp arm climate research facility. *Journal of Climate*, **23,** 5699-5714.

Craven, J. P., R. E. Jewell, and H. E. Brooks, 2002: Comparison between observed convective cloud-base heights and lifting condensation level for two different lifted parcels. *Weather and Forecasting*, **17,** 885-890.

Deardorff, J. W., 1970: Preliminary results from numerical integrations of the unstable planetary boundary layer. *Journal of the Atmospheric Sciences*, **27,** 1209-1211.

——, 1972: Parameterization of the planetary boundary layer for use in general circulation models1. *Monthly Weather Review*, **100,** 93-106.

Dee, D. P., and Coauthors, 2011: The era‐interim reanalysis: Configuration and performance of the data assimilation system. *Quarterly Journal of the royal meteorological society*, **137,** 553-597.

Dong, X., A. C. Schwantes, B. Xi, and P. Wu, 2015: Investigation of the marine boundary layer cloud and ccn properties under coupled and decoupled conditions over the azores. *Journal of Geophysical Research: Atmospheres*, **120,** 6179-6191.

Donner, L. J., T. A. O'Brien, D. Rieger, B. Vogel, and W. F. Cooke, 2016: Are atmospheric updrafts a key to unlocking climate forcing and sensitivity? *Atmospheric Chemistry and Physics*, **16,** 12983-12992.

Druilhet, A., J. P. Frangi, D. Guedalia, and J. Fontan, 1983: Experimental studies of the turbulence structure parameters of the convective boundary layer. *Journal of Climate and Applied Meteorology*, **22,** 594-608.

Fountoukis, C., and Coauthors, 2007: Aerosol–cloud drop concentration closure for clouds sampled during the international consortium for atmospheric research on transport and transformation 2004 campaign. *Journal of Geophysical Research: Atmospheres*, **112**.

Freud, E., and D. Rosenfeld, 2012: Linear relation between convective cloud drop number concentration and depth for rain initiation. *Journal of Geophysical Research: Atmospheres (1984–2012)*, **117**.

Freud, E., D. Rosenfeld, and J. Kulkarni, 2011: Resolving both entrainment-mixing and number of activated ccn in deep convective clouds. *Atmospheric Chemistry and Physics*, **11,** 12887-12900.

Ghate, V. P., B. A. Albrecht, M. A. Miller, A. Brewer, and C. W. Fairall, 2013: Turbulence and radiation in stratocumulus-topped marine boundary layers: A case study from vocals-rex. *Journal of Applied Meteorology and Climatology*, **53,** 117-135.

Greenhut, G. K., and S. J. Singh Khalsa, 1982: Updraft and downdraft events in the atmospheric boundary layer over the equatorial pacific ocean. *Journal of the Atmospheric Sciences*, **39,** 1803-1818.

——, 1987: Convective elements in the marine atmospheric boundary layer. Part i: Conditional sampling statistics. *Journal of Climate and Applied Meteorology*, **26,** 813-822.

Hahn, C. J., and S. G. Warren, 2007: *A gridded climatology of clouds over land (1971-96) and ocean (1954-97) from surface observations worldwide.* Oak Ridge National Laboratory, Carbon Dioxide Information Analysis Center.

Hartmann, D. L., M. E. Ockert-Bell, and M. L. Michelsen, 1992: The effect of cloud type on earth's energy balance: Global analysis. *Journal of Climate*, **5,** 1281-1304.

Heffter, J. L., 1980: Transport layer depth calculations. *B Am Meteorol Soc*, **61,** 97-97.

Hillger, D., and Coauthors, 2013: First-light imagery from suomi npp viirs. *B Am Meteorol Soc*, **94,** 1019-1029.

Holben, B. N., and Coauthors, 1998: Aeronet—a federated instrument network and data archive for aerosol characterization. *Remote sensing of environment*, **66,** 1-16.

Houghton, J. T., and Coauthors, 2001: *Climate change 2001: The scientific basis.* The Press Syndicate of the University of Cambridge.

Hourdin, F., and Coauthors, 2017: The art and science of climate model tuning. *B Am Meteorol Soc*, **98,** 589-602.

Jeong, M. J., and Z. Li, 2005: Quality, compatibility, and synergy analyses of global aerosol products derived from the advanced very high resolution radiometer and total ozone mapping spectrometer. *Journal of Geophysical Research: Atmospheres*, **110**.

——, 2010: Separating real and apparent effects of cloud, humidity, and dynamics on aerosol optical thickness near cloud edges. *Journal of Geophysical Research: Atmospheres*, **115**.

Jones, C., C. Bretherton, and D. Leon, 2011: Coupled vs. Decoupled boundary layers in vocals-rex. *Atmospheric Chemistry and Physics*, **11,** 7143-7153.

Kahn, R. A., B. J. Gaitley, J. V. Martonchik, D. J. Diner, K. A. Crean, and B. Holben, 2005: Multiangle imaging spectroradiometer (misr) global aerosol optical depth validation based on 2 years of coincident aerosol robotic network (aeronet) observations. *Journal of Geophysical Research: Atmospheres*, **110**.

Kaimal, J. C., J. C. Wyngaard, D. A. Haugen, O. R. Coté, Y. Izumi, S. J. Caughey, and C. J. Readings, 1976: Turbulence structure in the convective boundary layer. *Journal of the Atmospheric Sciences*, **33,** 2152-2169.

Kaufman, Y. J., D. Tanré, and O. Boucher, 2002: A satellite view of aerosols in the climate system. *Nature*, **419,** 215.

Khvorostyanov, V. I., and J. A. Curry, 2006: Aerosol size spectra and ccn activity spectra: Reconciling the lognormal, algebraic, and power laws. *Journal of Geophysical Research: Atmospheres (1984–2012)*, **111**.

Klein, S. A., D. L. Hartmann, and J. R. Norris, 1995: On the relationships among low-cloud structure, sea surface temperature, and atmospheric circulation in the summertime northeast pacific. *Journal of climate*, **8,** 1140-1155.

Kogan, Z. N., D. B. Mechem, and Y. L. Kogan, 2005: Assessment of variability in continental low stratiform clouds based on observations of radar reflectivity. *Journal of Geophysical Research: Atmospheres*, **110**.

Kollias, P., B. A. Albrecht, R. Lhermitte, and A. Savtchenko, 2001: Radar observations of updrafts, downdrafts, and turbulence in fair-weather cumuli. *Journal of the Atmospheric Sciences*, **58,** 1750-1766.

Lenschow, D. H., and P. L. Stephens, 1980: The role of thermals in the convective boundary layer. *Boundary-Layer Meteorol*, **19,** 509-532.

Lewis, E., and J. Teixeira, 2015: Dispelling clouds of uncertainty. *Eos, Transactions American Geophysical Union (Online)*, **96**.

Li, M., J. Liu, Z. Wang, H. Wang, Z. Zhang, L. Zhang, and Q. Yang, 2013a: Assessment of sea surface wind from nwp reanalyses and satellites in the southern ocean. *Journal of Atmospheric and Oceanic Technology*, **30,** 1842-1853.

Li, Z.-L., and Coauthors, 2013b: Satellite-derived land surface temperature: Current status and perspectives. *Remote Sensing of Environment*, **131,** 14-37.

Lilly, D. K., 1968: Models of cloud‐topped mixed layers under a strong inversion. *Quarterly Journal of the Royal Meteorological Society*, **94,** 292-309.

Liu, J., and Z. Li, 2014: Estimation of cloud condensation nuclei concentration from aerosol optical quantities: Influential factors and uncertainties. *Atmospheric Chemistry and Physics*, **14,** 471-483.

Liu, S., and X.-Z. Liang, 2010: Observed diurnal cycle climatology of planetary boundary layer height. *Journal of Climate*, **23,** 5790-5809.

Luo, Z. J., J. Jeyaratnam, S. Iwasaki, H. Takahashi, and R. Anderson, 2014: Convective vertical velocity and cloud internal vertical structure: An a‐train perspective. *Geophysical Research Letters*, **41,** 723-729.

Lynn, B. H., D. Rind, and R. Avissar, 1995: The importance of mesoscale circulations generated by subgrid-scale landscape heterogeneities in general circulation models. *Journal of Climate*, **8,** 191-205.

Manton, M. J., 1977: On the structure of convection. *Boundary-Layer Meteorol*, **12,** 491-503.

Martin, G., D. Johnson, D. Rogers, P. Jonas, P. Minnis, and D. Hegg, 1995: Observations of the interaction between cumulus clouds and warm stratocumulus clouds in the marine boundary layer during astex. *Journal of the atmospheric sciences*, **52,** 2902-2922.

Meskhidze, N., A. Nenes, W. C. Conant, and J. H. Seinfeld, 2005: Evaluation of a new cloud droplet activation parameterization with in situ data from crystal‐face and cstripe. *Journal of Geophysical Research: Atmospheres*, **110**.

Miller, M. A., and B. A. Albrecht, 1995: Surface-based observations of mesoscale cumulus–stratocumulus interaction during astex. *Journal of the atmospheric sciences*, **52,** 2809-2826.

Minnis, P., P. W. Heck, D. F. Young, C. Fairall, and J. Snider, 1992: Stratocumulus cloud properties derived from simultaneous satellite and island-based instrumentation during fire. *J Appl Meteorol*, **31,** 317-339.

Minnis, P., D. P. Garber, D. F. Young, R. F. Arduini, and Y. Takano, 1998: Parameterizations of reflectance and effective emittance for satellite remote sensing of cloud properties. *Journal of the atmospheric sciences*, **55,** 3313-3339.

Minnis, P., and Coauthors, 1995: Cloud optical property retrieval (subsystem 4.3). *Clouds and the Earth's Radiant Energy System (CERES) algorithm theoretical basis document*, **3,** 135-176.

Mishchenko, M. I., and Coauthors, 2003: Aerosol retrievals from avhrr radiances: Effects of particle nonsphericity and absorption and an updated long-term global climatology of aerosol properties. *Journal of Quantitative Spectroscopy and Radiative Transfer*, **79,** 953-972.

Moeng, C., and Coauthors, 1996: Simulation of a stratocumulus-topped planetary boundary layer: Intercomparison among different numerical codes. *B Am Meteorol Soc*, **77,** 261-278.

Neggers, R., B. Stevens, and J. D. Neelin, 2006: A simple equilibrium model for shallow-cumulus-topped mixed layers. *Theoretical and Computational Fluid Dynamics*, **20,** 305-322.

Paluch, I. R., and D. G. Baumgardner, 1989: Entrainment and fine-scale mixing in a continental convective cloud. *Journal of the atmospheric sciences*, **46,** 261-278.

Peng, Y., U. Lohmann, and R. Leaitch, 2005: Importance of vertical velocity variations in the cloud droplet nucleation process of marine stratus clouds. *Journal of Geophysical Research: Atmospheres*, **110**.

Petters, M., and S. Kreidenweis, 2007: A single parameter representation of hygroscopic growth and cloud condensation nucleus activity. *Atmospheric Chemistry and Physics*, **7,** 1961-1971.

Pinsky, M., A. Khain, I. Mazin, and A. Korolev, 2012: Analytical estimation of droplet concentration at cloud base. *Journal of Geophysical Research: Atmospheres (1984–2012)*, **117**.

Quaas, J., and O. Boucher, 2005: Constraining the first aerosol indirect radiative forcing in the lmdz gcm using polder and modis satellite data. *Geophysical research letters*, **32**.

Remer, L. A., and Coauthors, 2008: Global aerosol climatology from the modis satellite sensors. *Journal of Geophysical Research: Atmospheres*, **113**.

Rosenfeld, D., H. Wang, and P. J. Rasch, 2012a: The roles of cloud drop effective radius and lwp in determining rain properties in marine stratocumulus. *Geophysical Research Letters*, **39**.

Rosenfeld, D., B. Fischman, Y. Zheng, T. Goren, and D. Giguzin, 2014a: Combined satellite and radar retrievals of drop concentration and ccn at convective cloud base. *Geophysical Research Letters*, **41,** 3259-3265.

Rosenfeld, D., E. Williams, M. Andreae, E. Freud, U. Pöschl, and N. Rennó, 2012b: The scientific basis for a satellite mission to retrieve ccn concentrations and their impacts on convective clouds. *Atmospheric Measurement Techniques*, **5,** 2039.

Rosenfeld, D., G. Liu, X. Yu, Y. Zhu, J. Dai, X. Xu, and Z. Yue, 2014b: High-resolution (375 m) cloud microstructure as seen from the npp/viirs satellite imager. *Atmospheric Chemistry and Physics*, **14,** 2479-2496.

Rosenfeld, D., and Coauthors, 2014c: Global observations of aerosol‐cloud‐precipitation‐climate interactions. *Reviews of Geophysics*, **52,** 750-808.

Rosenfeld, D., and Coauthors, 2016: Satellite retrieval of cloud condensation nuclei concentrations by using clouds as ccn chambers. *Proceedings of the National Academy of Sciences***,** 201514044.

Schmidt, H., and U. Schumann, 1989: Coherent structure of the convective boundary layer derived from large-eddy simulations. *J Fluid Mech*, **200,** 511-562.

Schubert, W. H., J. S. Wakefield, E. J. Steiner, and S. K. Cox, 1979: Marine stratocumulus convection. Part i: Governing equations and horizontally homogeneous solutions. *Journal of the Atmospheric Sciences*, **36,** 1286-1307.

Schumann, U., 1988: Minimum friction velocity and heat transfer in the rough surface layer of a convective boundary layer. *Boundary-Layer Meteorol*, **44,** 311-326.

Seinfeld, J. H., and Coauthors, 2016: Improving our fundamental understanding of the role of aerosol− cloud interactions in the climate system. *Proceedings of the National Academy of Sciences*, **113,** 5781-5790.

Slingo, A., 1990: Sensitivity of the earth's radiation budget to changes in low clouds. *Nature*, **343,** 49-51.

Solomon, S., 2007: *Climate change 2007-the physical science basis: Working group i contribution to the fourth assessment report of the ipcc.* Vol. 4, Cambridge University Press.

Stephens, G., 1978: Radiation profiles in extended water clouds. I: Theory. *Journal of the Atmospheric Sciences*, **35,** 2111-2122.

Stephens, G. L., and T. J. Greenwald, 1991: The earth's radiation budget and its relation to atmospheric hydrology: 2. Observations of cloud effects. *Journal of Geophysical Research: Atmospheres*, **96,** 15325-15340.

Stevens, B., W. R. Cotton, G. Feingold, and C.-H. Moeng, 1998: Large-eddy simulations of strongly precipitating, shallow, stratocumulus-topped boundary layers. *Journal of the atmospheric sciences*, **55,** 3616-3638.

Stevens, B., and Coauthors, 2005: Evaluation of large-eddy simulations via observations of nocturnal marine stratocumulus. *Monthly weather review*, **133,** 1443-1462.

Stier, P., 2016: Limitations of passive remote sensing to constrain global cloud condensation nuclei. *Atmos. Chem. Phys*, **16,** 6595-6607.

Stocker, T., 2014: *Climate change 2013: The physical science basis: Working group i contribution to the fifth assessment report of the intergovernmental panel on climate change.* Cambridge University Press.

Stull, R. B., 1985: A fair-weather cumulus cloud classification scheme for mixed-layer studies. *Journal of Climate and Applied Meteorology*, **24,** 49-56.

Stull, R. B., 1994: A convective transport theory for surface fluxes. *Journal of the Atmospheric Sciences*, **51,** 3-22.

Stull, R. B., 2012: *An introduction to boundary layer meteorology.* Vol. 13, Springer Science & Business Media.

Tao, W. K., J. P. Chen, Z. Li, C. Wang, and C. Zhang, 2012: Impact of aerosols on convective clouds and precipitation. *Reviews of Geophysics*, **50**.

Taylor, G. J. B. G. K., 1960: *Scientific papers.* [s.n.], 6 pp.

Torres, O., P. Bhartia, J. Herman, Z. Ahmad, and J. Gleason, 1998: Derivation of aerosol properties from satellite measurements of backscattered ultraviolet radiation: Theoretical basis. *Journal of Geophysical Research: Atmospheres*, **103,** 17099-17110.

Tucker, S. C., and Coauthors, 2009: Doppler lidar estimation of mixing height using turbulence, shear, and aerosol profiles. *Journal of Atmospheric & Oceanic Technology*, **26**.

Twomey, S., 1959: The nuclei of natural cloud formation part ii: The supersaturation in natural clouds and the variation of cloud droplet concentration. *Pure and Applied Geophysics*, **43,** 243-249.

Várnai, T., and A. Marshak, 2015: Effect of cloud fraction on near-cloud aerosol behavior in the modis atmospheric correction ocean color product. *Remote Sensing*, **7,** 5283-5299.

Warren, G., J. Hahn, J. London, M. Chervin, and L. Jenne, 1986: Global distribution of total cloud cover and cloud type amounts over land.

Warren, S. G., C. J. Hahn, J. London, R. M. Chervin, and R. L. Jenne, 1988: Global distribution of total cloud cover and cloud type amounts over the ocean.

Williams, E., and S. Stanfill, 2002: The physical origin of the land–ocean contrast in lightning activity. *Comptes Rendus Physique*, **3,** 1277-1292.

Wood, R., 2012: Stratocumulus clouds. *Monthly Weather Review*, **140,** 2373-2423.

Wood, R., and J. P. Taylor, 2001: Liquid water path variability in unbroken marine stratocumulus cloud. *Quarterly Journal of the Royal Meteorological Society*, **127,** 2635-2662.

Wood, R., and C. S. Bretherton, 2004: Boundary layer depth, entrainment, and decoupling in the cloud-capped subtropical and tropical marine boundary layer. *Journal of climate*, **17,** 3576-3588.

——, 2006: On the relationship between stratiform low cloud cover and lower-tropospheric stability. *Journal of climate*, **19,** 6425-6432.

Wood, R., and Coauthors, 2015: Clouds, aerosols, and precipitation in the marine boundary layer: An arm mobile facility deployment. *B Am Meteorol Soc*, **96,** 419-440.

Young, G. S., 1988: Turbulence structure of the convective boundary layer. Part ii. Phonenix 78 aircraft observations of thermals and their environment. *Journal of the atmospheric sciences*, **45,** 727-735.

Zhao, T., W. Guo, and C. Fu, 2008: Calibrating and evaluating reanalysis surface temperature error by topographic correction. *Journal of Climate*, **21,** 1440-1446.

Zheng, Y., and D. Rosenfeld, 2015: Linear relation between convective cloud base height and updrafts and application to satellite retrievals. *Geophysical Research Letters*, **42,** 6485-6491.

Zheng, Y., D. Rosenfeld, and Z. Li, 2015: Satellite inference of thermals and cloud-base updraft speeds based on retrieved surface and cloud-base temperatures. *Journal of the Atmospheric Sciences*, **72,** 2411-2428.

——, 2016: Quantifying cloud base updraft speeds of marine stratocumulus from cloud top radiative cooling. *Geophysical Research Letters*, **43**.

——, 2017: New insights to the mechanism of surface coupling of elevated marine stratocumulus clouds. *submitted to Proceedings of the National Academy of Sciences*.

Zhou, X., P. Kollias, and E. R. Lewis, 2015: Clouds, precipitation, and marine boundary layer structure during the magic field campaign. *Journal of Climate*, **28,** 2420-2442.

Zhu, Y., D. Rosenfeld, X. Yu, G. Liu, J. Dai, and X. Xu, 2014: Satellite retrieval of convective cloud base temperature based on the npp/viirs imager. *Geophysical Research Letters*, **41,** 1308-1313.